technische universität
dortmund

Fakultät Physik – Experimentelle Physik V

Physik E5

The talkative AGN next door

Broad-band spectral variability
of the TeV blazar Markarian 501

Dissertation

zur Erlangung des akademischen Grades eines
Doktors der Naturwissenschaften
(Dr. rer. nat.)

vorgelegt von

Dipl.-Phys. Marlene Doert

Februar 2013

Contents

Chapter 1

Introduction

Astroparticle physics is a comparably young field of research, which unites scientists from the domain of particle physics and from the area of astronomy and astrophysics. Just after the celebration of its 100^{th} anniversary in the year 2012, astroparticle physics continues to be an active and fast-growing field, which promises not only to provide deeper insights into the most powerful environments within our Universe, but also to deliver results at the interface of searches for new physics in various different fields. Ultimately, this synergy will help us to understand the evolution, constitution and the future of our Universe.

Within astroparticle physics, the field of gamma-ray astronomy can be seen as the natural extension of “conventional” astronomy, which mankind has pursued probably ever since by exploring the night sky with the naked eye or, later on, through the help of telescopes. In the last century, the accessible part of the electromagnetic spectrum has been expanded beyond visible light by the use of radio telescopes and satellite experiments. Gamma-ray astronomy now allows to probe the very end of the electromagnetic spectrum and can thus give insights into the most energetic phenomena in the Universe. After the technique passed its *proof of principle* only a few decades ago, the exploration of the gamma-ray sky is now entering a *Golden Age*, as experiments are at hand which are sensitive enough to allow for deep studies of cosmological objects, such as the black holes sitting at the center of *active galaxies*.

The work performed in the scope of this thesis has been dedicated to a better understanding of the phenomenon of *active galactic nuclei* (AGN). These objects stand out by producing a powerful and highly variable output over the entire electromagnetic spectrum, while being one of the most favored candidates for the sources of the highest energetic cosmic radiation in charged particles. A better understanding of these objects will pave the way for detailed studies of the evolution of the cosmos and the discovery of new fundamental physics phenomena.

The subject of AGN has been approached via the example of the TeV blazar Markarian 501, which presents itself as the ideal candidate for deep studies of the intrinsic mechanisms at work, by its vicinity and high variability.

The work which is presented in this thesis is anchored in the field of gamma-ray astronomy, as it has been performed within the collaboration of the MAGIC experiment. Still, besides the cooperation with groups exploring the other bands of the electromagnetic spectrum in a *multi-wavelength* study, the connection to another area of astroparticle physics research, namely the field of neutrino astronomy, has been pursued in the context of the *multi-messenger* approach.

The thesis is organized as follows:

Chapter 2 gives a brief overview of the field of astroparticle physics. The different messenger particles are introduced, the relevant basic mechanisms by which they are accelerated, produced, deflected or attenuated are outlined and the different types of sources which are currently being studied are briefly discussed.

A preface to the principles of air showers and Cherenkov gamma-ray astronomy is given in **Chapter 3**, followed by an introduction of the MAGIC experiment. The experimental setup of the two-telescope system as well as the basic analysis procedure are illustrated here.

In **Chapter 4**, the theme of *inverse problems* is outlined, followed by an introduction into the method of *regularized unfolding*. After a brief presentation of the novel unfolding program TRUEE, the incorporation of the program into the standard MAGIC analysis chain is discussed, which has been a major project in the course of this thesis. Subsequently, the first application of the new unfolding chain on MAGIC telescope data is presented.

Being one of the major candidates discussed in the preceding chapters, **Chapter 5** introduces the source class of AGN and blazars in particular, summarizing their observational properties throughout the electromagnetic spectrum. The current state of research and the open questions are outlined. The object Markarian 501, which is subject to two studies which have been performed in the course of this thesis, following quite different approaches, is introduced here.

Chapter 6 presents a multi-instrument campaign on Markarian 501, which has been another major project in the scope of this thesis. At first, the results of an analysis of the corresponding MAGIC data are shown. Subsequently, the multi-instrument data set is discussed, including detailed studies of variability and inter-band correlations, spectral variability and the evolution of the broad-band spectral energy distribution during flaring episodes. The results are discussed in the light of leptonic emission models, based on previous works on this data set, and in the context of similar results seen in other source classes.

Chapter 7 approaches Markarian 501, and the blazar class in general, from a contrary point of view, assuming hadronic interactions and the consequential production of neutrinos. An estimation for a possible neutrino signal from such processes is pursued, while only simple bolometric considerations are used. The results, which are obtained on the basis of the data set presented in the preceding chapter, are discussed in the context of state-of-the-art neutrino astronomy.

After detailed discussions of results and conclusions are given at the end of the respective chapters, **Chapter 8** concludes the thesis and provides a brief outlook to possible future activities based on the presented work.

Chapter 2

Astroparticle Physics Briefly

The first step into the field of astroparticle physics was taken by V. Hess in 1912, when he discovered that ionizing radiation, which he called *Höhenstrahlung*, is reaching us from space [Hes12]. Further findings which were linked to measurements of astroparticles, like the discovery of the muon, the pion and the positron, have had great influence on the development of particle physics. Nowadays, astroparticle physics has emerged to be a vivid, still young, field of research. It has grown to be an advantageous combination of astrophysics and particle physics, from which both "parent" fields substantially profit.

The possible channels to study astrophysical sources have been expanded by very high energy photons, neutrinos and potentially charged particles such as the highest energy protons. These new messengers give access to the most powerful phenomena in our Universe, and will contribute to understanding extreme events such as supernova explosions and gamma-ray bursts, but also the fascinating phenomenon of black holes, their influence on the formation of galaxies and ultimately the formation of the Universe that we know today.

On the other hand, cosmic accelerators can be exploited to study particle physics at energy scales beyond anything possible to establish in man-made machines. Once the sources of the highest energy cosmic rays are found and a reasonable understanding is acquired, they could be promising cosmic laboratories which offer accelerated particles at outstandingly high energies and even "for free", while of course posing the challenge of an uncontrollable and probably unpredictable particle beam.

For a detailed introduction into the field of astroparticle physics, see for example [FR12] and [BG06], which served as the basic references for the following sections.

2.1 The Messengers

The messenger particles which are addressed in the context of astroparticle physics, namely the charged cosmic rays, highest energy photons and neutrinos, have very different characteristics, which give them distinct advantages (and disadvantages) for studying different aspects of the highest energy phenomena. In the following, a short overview of the particles and their major properties is given.

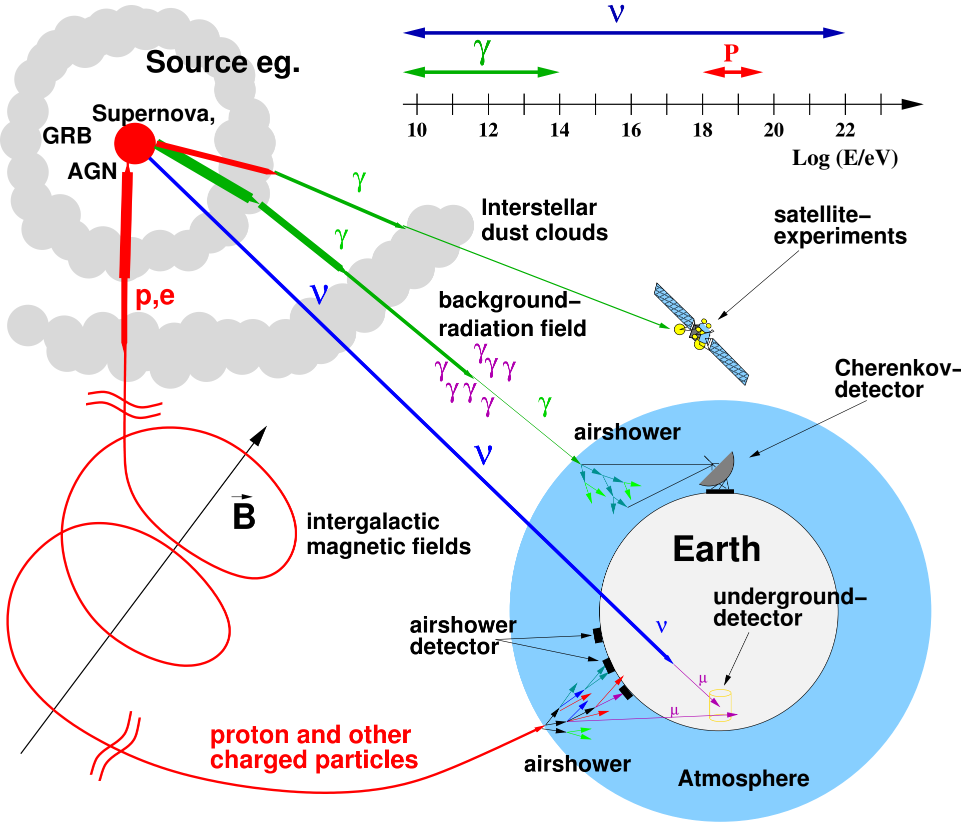

Figure 2.1: Schematic overview of multi-messenger astrophysics: emission in charged particles (p, e), high energy photons (γ) and neutrinos (ν) is emitted from a particle accelerating source (for a discussion of the sources see section 2.3). The particles propagate through space where they are perturbed by magnetic fields (p, e), clouds and background radiation (p, e and γ) or not at all (ν), until they are detected in one of the various experiments in the Earth's orbit, on the surface or underground. The typical energies of the particles are also indicated. Figure: [Dre10] after [Wag04].

2.1.1 Charged cosmic rays

After an incoming flux of charged particles has been found by V. Hess in 1912, the term *cosmic rays* (CR) was coined by R. A. Millikan in 1925 [MC28]. To distinguish these particles from the very high energy photons, which also contribute to the cosmic radiation (see Sec. 2.1.2), they are nowadays also referred to more precisely as *charged cosmic rays*. The population of particles which enter the atmosphere are made up by 98% of light atomic nuclei (at energies $> 1\,\text{GeV}$). At these energies, charged leptons contribute only by $\approx 2\%$, cf. [BG06].
The spectral distribution of cosmic ray particles spans up to 13 orders of magnitude in energy. Its shape is essentially a power-law, with two spectral breaks at 10^{15}-10^{16} eV (the so-called *knee*) and at 10^{18}-10^{19} eV (the *ankle*). The corresponding spectral indices are -2.7

before the knee, a steepening to -3.0 above, and a flattening after the ankle, cf. [BG06]. At energies above $4 \cdot 10^{19}$ eV, the particles have enough energy to interact with ambient photons of the *cosmic microwave background* (CMB), see [PW65]. This phenomenon is known as the *Greisen-Zatsepin-Kuzmin* (GZK) cutoff, which was predicted in 1966 [Gre66,ZK66]. Recent measurements confirm a suppression of the flux at these energies [A+08a]. For more details see also [FR12].

Being electrically charged, CR particles interact with interstellar and intergalactic magnetic fields. Due to multiple deflections in these fields, the particle flux is isotropized and generally no information can be gained about the origin of the particles.

The breaks in the spectrum might be hints to possible limitations of different accelerating mechanisms or populations of sources. Particles which contribute to the flux at the highest energies are likely to stem from outside the Milky Way, as the galactic magnetic fields cannot confine particles with gyroradii corresponding to such energies [Lin63]. The question of the sources of CRs in this energy range is one of the crucial puzzles in the field today. Several source classes (and single sources) beyond our galaxy have been suggested as good candidates for this emission, see e.g. [BS12, TH11, DR10].

Due to the same effect, particles at the highest energies (the so-called *sub-GZK* particles), are crucial to be studied, as they are less deflected during propagation through space and should point back to their sources. The low particle flux, which governs this energy range, requires elaborate detection techniques in order to acquire the necessary amount of events, such as the Auger experiment, which combines particle detectors and fluorescence telescopes to a 3000 km^2 sized hybrid experiment [A+08a].

2.1.2 Cosmic gamma-rays

Another part of the cosmic radiation is formed by photons which populate the high energy end of the electromagnetic spectrum, the gamma-rays ($E \gtrsim 1\,\mathrm{MeV}$). Due to their electromagnetic neutrality, gamma-rays are not deflected by magnetic fields during their propagation. Therefore, they can be used to perform source studies, which has led to the new field of *gamma-ray astronomy*. However, at the highest energies these photons undergo attenuation by interactions with low energy photons, which fill up the Universe. This background field, which is formed by the accumulation of star light and radiation from dust, is commonly referred to as the *Extragalactic Background Light* (EBL). Models are at hand which describe the distribution of low energy photons and the resulting attenuation factors as a function of energy and source distance, see e.g. [SDJS92,KD10,FRV08]. As the EBL has a direct relation to the evolution of the Universe itself, gamma-ray spectra of cosmological sources are used to study the composition and evolution with time and distance of the EBL.

The detection of gamma-ray photons is hindered by the fact that, unlike photons in the optical or the radio regime, they are absorbed by the atmosphere. Satellite missions such as the *Energetic Gamma Ray Experiment Telescope* (EGRET) [K+89] and now the *Fermi Gamma-ray Space Telescope* (*Fermi*-GST) [A+09c] are used to probe the flux in gamma-rays from outside the Earth's atmosphere. Due to the limits in detector size, however, combined with steeply decreasing statistics towards higher energies, only the range up to $\approx 300\,\mathrm{GeV}$ can be accessed with these instruments. In the regime of very high energies ($E \gtrsim 50\,\mathrm{GeV}$), the *imaging atmospheric Cherenkov technique* offers to use the atmosphere as a detection volume, by observing so-called *extensive air-showers* which are initiated by the gamma-ray photons. Chapter 3 will give more insight into ground-based gamma-ray astronomy and introduce one of the state-of-the-art experiments in the field, the MAGIC telescopes [A+12a].

2.1.3 Neutrinos

The third species of cosmic messenger particles are neutrinos - neutral, very light leptons. Due to the fact that they interact only via the weak force, neutrinos are able to travel over large distances without being deflected or attenuated. And while photons (and hadrons) might be trapped in central regions of stars or within the sites of particle acceleration and production, neutrinos can easily escape. These characteristics make them ideal messengers in order to probe the center of objects in far distances which are opaque to other kinds of emission.

Neutrinos are produced in hadronic interactions, e.g. in the fusion of atomic nucleii at the center of the sun or as a decay product of particles created in interactions of relativistic hadrons with photon fields or among themselves.

During their propagation in space, neutrinos undergo oscillations between the different flavor states (ν_e, ν_μ, ν_τ). This effect was found as the solution to the *solar neutrino problem*, which was phrased after a too small flux in ν_e was measured from the sun [BD66, GP69]. The confirmation of these oscillations can be seen as the first correction to the *standard model of particle physics* (SM), as oscillations require neutrinos to have a finite mass, which is not foreseen in the SM.

After studies of astrophysical neutrinos in absorption experiments (e.g. Homestake [C+98] and GALLEX [Vig98]) and scattering experiments (such as (Super-)Kamiokande [F+98b]), which utilized detection volumes such as water tanks for their measurement, experiments of a new type have been set up in order to detect cosmic neutrinos at the highest energies. The steeply decreasing event numbers at very high energies and the small cross-section of the interactions themselves required much larger detector volumes and led to the exploitation of natural water or ice environments, such as a lake (BAIKAL [B+97a]), the sea (e.g. ANTARES [A+11d]) and the antarctic ice (first AMANDA [A+00], currently IceCube [A+06a]). The biggest challenge for these experiments is the suppression of a vast background of neutrinos which are induced in interactions of charged CRs in the atmosphere. So far no detection of cosmic *very high energy* (VHE) neutrinos could be claimed.

2.2 The Processes

In the following, the processes of particle acceleration and interaction which are relevant for this work are outlined briefly. For a very recent overview and detailed explanations on the processes introduced below, see for example [FR12] and [BHK12], but also [RL08].

2.2.1 Particle acceleration - Fermi I and II

E. Fermi was the first to postulate the idea that CRs might be produced by collisions of particles with magnetized interstellar clouds [Fer54]. This *stochastic acceleration* involves terms with $\mathcal{O}(\Delta v^2)$, where Δv is the differential of the involved velocities, and is therefore also known as *second-order Fermi acceleration*.

Later on, this principle was applied to shock environments, see [Kry77, ALS77, Bel78a, Bel78b, BO78], which yields a process that is linear in the velocity differential ($\mathcal{O}(\Delta v)$), and is thus much more efficient. This *diffusive shock acceleration* is therefore also referred to as *first-order Fermi acceleration*. Like the stochastic acceleration, this process leads to power-law distributions of the resulting particle spectra. In the non-relativistic case, the spectral index only depends on the shock compression, e.g. the ratio between the plasma velocities upstream and downstream of the shock. In the case that the shock moves at relativistic speed, see e.g. [K$^+$00a], it depends on the upstream flow speed, orientation of the magnetic field with respect to the shock and the characteristics of the involved scattering processes. Typically, indices around -2 are realized. Fermi acceleration at relativistic shocks is thought to take place within relativistic jets in astronomical objects. For a descriptive discussion of the processes see e.g. [FR12] and [BHK12].

2.2.2 Synchrotron radiation

Charged particles which are moving within a magnetic field generally follow a spiral path. This means that they are constantly deflected or accelerated. In the relativistic case, they will emit synchrotron radiation, which can be understood as the relativistic generalization of cyclotron radiation. This highly polarized radiation can span over a broad spectrum, while the spectral index of the photon distribution is closely related to the distribution of the emitting particles. Discussing the energy distribution of the accelerated particles $n(\gamma)$, energies are described in terms of the particle Lorentz factor γ, corresponding to

$$\gamma = \frac{1}{\sqrt{1-\beta^2}}, \text{ with } \beta = \frac{v}{c}. \tag{2.1}$$

For a particle distribution

$$n(\gamma) = n_0 \gamma^{-p}, \tag{2.2}$$

which is characterized by a spectral index p (while n_0 represents a normalization factor), this results in a synchrotron spectrum which, over a wide range in ν, follows

$$j(\nu) \propto \nu^{-\alpha_{\mathrm{sy}}}, \text{ with } \alpha_{\mathrm{sy}} = \frac{p-1}{2}, \tag{2.3}$$

combined with a low and a high energy cutoff, cf. [BHK12]. Here, ν denotes the photon frequency, $j(\nu)$ is the spectral distribution of the photons and α_{sy} defines the synchrotron spectral index. Naturally, the spectra become more complicated for more detailed particle spectra.

Due to this so-called *synchrotron cooling*, the radiating particle loses energy, while the *particle energy-loss rate* strongly depends on the mass (m) of the particle:

$$\frac{d\gamma}{dt}_{\mathrm{sy}} \propto -m^{-3}, \tag{2.4}$$

see [BHK12] for a more detailed expression. This makes electrons radiate much more efficiently than heavier particles, but it also implies that they cool fast and acceleration to the highest energies is problematic. Protons or heavier nuclei radiate less efficiently, but can be accelerated to very high energies more easily.

A part of the produced synchrotron photons may be absorbed again during interactions with the relativistic electrons, which leads to an effect known as *synchrotron self-absorption*. The corresponding absorption probability is dependent on the magnetic field and the photon frequency itself. Consequentially, the regions of such synchrotron radiation may be opaque (with an optical depth $\tau \geq 1$) below a critical frequency ν_{SSA}. For detailed calculations and illustrations of the resulting spectrum see e.g. [BHK12].

2.2.3 (Inverse) Compton scattering

Electrons (and positrons) can undergo Compton scattering processes with photons, which are in the general case described by the *Klein-Nishina cross-section*, see e.g. [JR76, Hei54]. For small photon energies, the process can be approximated by the constant *Thomson cross-section*, which describes an elastic scattering in the rest frame of the electron.
Such scattering interactions are thought to occur in astrophysical regions of particle acceleration, which are typically filled with relativistic electrons and dense photon fields. In the following, photon energies are denoted in units of the electron rest mass:

$$\epsilon \equiv \frac{h\nu}{m_e c^2}, \tag{2.5}$$

while the electron energy is denoted in terms of its Lorentz factor γ.
In the so-called *Thomson regime* (at low photon energies), the photon's energy after scattering is given, in the rest frame of such an emission region, by

$$\epsilon_{\mathrm{scat}} \approx \gamma^2 \epsilon, \tag{2.6}$$

while ϵ describes the energy of the photon before scattering, cf. [BHK12]. The photon receives a boost in energy from the electron. As the direction of energy transfer is contrary to the commonly known Compton scattering, this process is also referred to as *inverse Compton scattering*.
In the *Klein-Nishina limit*, where $\epsilon\gamma \gtrsim 1$, the cross-section for the process is strongly suppressed. This makes the upscattering of high energy photons much less efficient.
It can be shown that the (inverse) Compton spectrum is characterized by the same spectral index $\alpha_{\mathrm{C}} = \alpha_{\mathrm{sy}}$, which was obtained for the synchrotron spectrum, if a power-law distribution of electrons and a monoenergetic photon field are assumed [BHK12]. See this reference also for detailed calculations of the cross sections, including also its angular dependence.

2.2.4 $\gamma\gamma$-absorption

Photons of different energies ϵ_1 and ϵ_2 can interact with each other and produce an electron-positron pair. This is true for high energy gamma-ray photons among themselves and with low energy photons, as long as the relevant energy threshold

$$\epsilon_1 \geq \frac{2}{\epsilon_2(1-\mu)} \tag{2.7}$$

is surpassed. Here, $\mu = \cos(\Theta)$ describes the collision angle, cf. [BHK12]. These processes are important for interactions of high energy gamma-ray photons with photon fields of lower energy, such as e.g. radiation from the surrounding accretion disk in the vicinity of a plasma jet, which will be discussed in chapter 5.

Besides interactions within the sources of the emission themselves, very high energy gamma-rays can interact with photons of the EBL. The corresponding optical depth $\tau_{\gamma\gamma}$ increases with gamma-ray photon energy and with the distance of the source.

2.2.5 Photo-hadronic interactions

Hadronic particles are thought to be present, for example, in plasma jets (see section 5.1) and can be accelerated to relativistic energies. In these environments, they can interact with present photon fields via a number of different processes.

Protons and heavier nuclei can interact with the ambient photon field to create electron/positron pairs via *Bethe-Heitler Pair production* [BH34]. However, it is found that photo-hadronic processes are more dominant in the scenarios discussed in the course of this thesis (e.g. relativistic plasma jets). For a thorough treatment on these interactions see e.g. [BHK12].

In so-called *photomeson production* processes, the interaction of protons or nuclei with the photon field can create mesons, predominantly pions, following four different channels: the excitation and subsequent decay of resonances, the direct pion production without involved resonances, diffractive scattering and multi-pion production, cf. [BHK12]. In the $\Delta-$*approximation*, only the largest resonance $\Delta(1232)$ is considered for the production of mesons, which leads to branching ratios of the neutral pion π_0 to the charge pion π^+ of 2:1. As mentioned above, this process leads predominantly to the production of pions, while the decay into other mesons (mainly K and η) contribute by less than 20%, cf. [BHK12]. A neutral pion decays further into two (very high energy) photons, while a charged pion decays into a muon and a neutrino and further into an electron/positron and two more neutrinos. In chapter 7, these interactions will be treated in more detail in the light of the mentioned approximations.

2.2.6 Electromagnetic cascades

In opaque regions, photons are likely to interact with the present photon field via various processes, producing electrons/positrons, which themselves result again in the production of photons and so on. In these so called *cascades*, the photon energy is gradually reprocessed towards lower energies. As several different processes are involved and interlinked, these cascades cannot be described in a trivial way. Connected to the size of the emission region, the processes can be differentiated into “saturated cascades”, where more photon interactions take place than photons escape the region, and “non-saturated” cascades, where the typical escape time is lower. While the former type generally leads to power-law distributions with spectral indices $\alpha_\gamma \to 2$, the cascades of the latter type tend to terminate after a few cycles, cf. [BHK12].

2.3 The Sources

In the following, some of the most interesting sources for the production of high energy radiation - gamma-rays and neutrinos, but possibly also charged CR - will be introduced briefly.

2.3.1 Supernova remnants

Within our galaxy, *super nova remnants* (SNR) make up one of the most interesting source classes for the detection of astroparticles. The most prominent representative is the Crab Nebula, which is the remnant of a super nova that has been observed by Chinese astronomers in 1054. After the core of a massive star collapses because of a depletion in the fusion material, its outer material is ejected into the interstellar medium, producing shocks and excellent sites for particle acceleration. While the core might form a neutron star (possibly a pulsar) or a black hole, the remaining outer shells of the former star are referred to as a SNR. In the case of a rotating neutron star at the center of the object, the remnant is called a *pulsar wind nebula* (PWN). Typically, SNR exhibit very hard spectra in gamma-rays, which are cutoff only at energies of about 20 TeV. This indicates that the accelerated particles, which are responsible for the emission of gamma-rays, must feature energies up to 10^{14} or even 10^{15} eV, cf. [FR12]. SNRs are thought to make a substantial contribution to the observed flux of charged CRs below and possibly also above the knee, see also [Dru12].

2.3.2 Binary systems

Another promising class of sources are binary systems, which contain a compact remainder of a former massive star (either a black hole or a neutron star). These systems are characterized by accretion of matter onto the compact object, which might exhibit outflows of relativistic particles in the form of plasma jets, cf. [FR12] and also chapter 5. Such systems are referred to as *micro quasars*.

2.3.3 Galactic center

A region which is densely populated, and probably hosts many different classes of promising candidates for high energy emission, is the Galactic center. However, given the large density of emitters, the detection and investigation of single sources is challenging. Within the most prominent feature in this region, Saggitarius (Sgr) A, possibly a super-massive black hole has been identified (Sgr A*), which is also an emitter of VHE gamma-rays [KT12, A^+04], cf. [FR12].
As a center of mass accumulation, the Galactic center is also a good candidate for searches for *dark matter* (DM) annihilation or decay signatures. Gamma-rays could be produced as a product of these processes. However, the hard spectrum seen from this region suggests the dominant emission to come from PWN rather than dark matter annihilation/decay, cf. [FR12].

2.3.4 Active galaxies

Beyond our galaxy, radio galaxies, quasars and a large number of different source classes, which are seen in radio, optical, X-ray and higher frequencies, have been summarized as *Active Galactic Nuclei* (AGN). These objects, which host a super-massive black hole that is fed by surrounding material, are thought to (partly) exhibit highly relativistic particle outflows, which are the sources of VHE gamma-rays and possibly also of the highest energy CRs. The source class of AGN and the subclass of *blazars* will be introduced in more detail in chapter 5.

2.3.5 Gamma-ray bursts

Spontaneous, very rapid outbursts in gamma-rays have been detected, which subside again after few seconds, but leave a so-called *afterglow* in optical, radio and X-ray frequencies, which can be visible over weeks. These transient objects have been named *gamma-ray bursts* (GRB) and are thought to be caused by core-collapse supernovae and/or colliding neutron stars, cf. [BG06]. GRBs constitute one of the most promising source classes for the emission of the highest energy CRs.

2.3.6 Starburst galaxies

Starburst galaxies are a subclass of galaxies, which show no core activity like AGN, but still exhibit TeV gamma-ray emission (for an overview and a recent discussion see e.g. [Ohm12, LT12]). The large abundance of supernova events leads to strong stellar winds within these galaxies, which are thought to be sites for particle acceleration, cf. [FR12].

2.3.7 Candidates for CR emission - the Hillas plot

While supernovae are discussed as the best candidates for the production of charged cosmic rays at intermediate to high energies, the sources for the highest energy CRs are still looked for. In 1984, M. Hillas discussed the properties which give a source class the capability to accelerate particles up to such high energies. The potential of a source depends on the size of the emitting region and the strength of the prevailing magnetic fields (B), in combination with the charge (Ze) and energy (E) of the particles themselves. In the scope of gradual acceleration models, the size of the accelerating region L has to be much larger than the particle's Larmor radius

$$r_L \propto \frac{E}{ZB}, \tag{2.8}$$

in order to keep particles in the process. Taking into account scattering processes and the relativistic velocity of the scattering centers β, the following condition has to be fulfilled:

$$BL > \frac{2E}{Z\beta}, \tag{2.9}$$

where B is given in μG, L in pc and E is quoted in 10^{15} eV, cf. [Hil84]. In the so-called *Hillas plot* (see Figure 2.2), possible candidates for the acceleration of protons and heavier

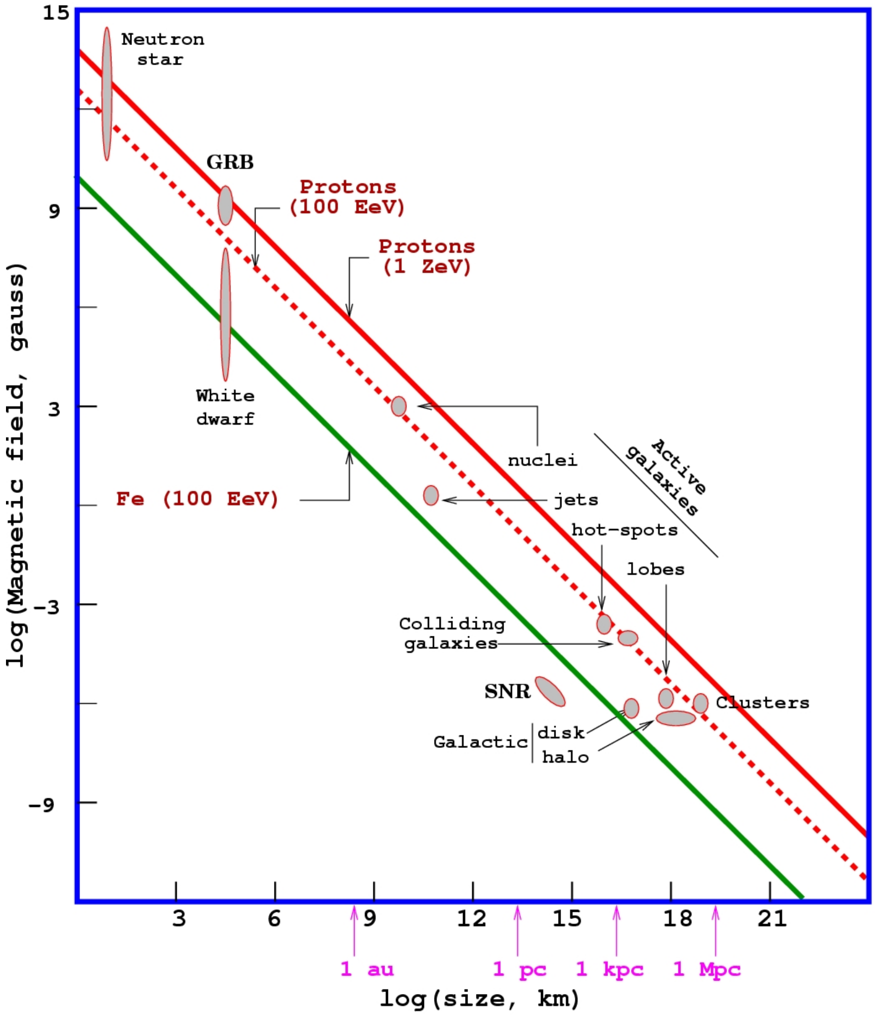

Figure 2.2: The Hillas plot: overview of candidate sources (or regions within sources) for the emission of the highest energy CR, based on their size and the prevailing magnetic field. Objects below the respective diagonal lines cannot accelerate particles to the given energies. While particular regions in AGN could be responsible for the emission of protons up to ≈ 100 EeV, GRB or neutron stars might be the sources of ultra high energy CRs at around 1 ZeV. For more details, see text. Figure: [Str09], adapted from [Hil84].

nuclei of different energies can be identified.
Currently, AGN jets (or so-called *hot spots* therein) are still favored, before GRBs, as emitters of the highest energy cosmic rays, see e.g. [B^{+}09a, Der11]. In chapter 5, these interesting and promising objects will be introduced and discussed in more detail.

Chapter 3

Gamma-ray Astronomy with the MAGIC Telescopes

The gamma-ray spectrum which reaches Earth from a - meanwhile large - number of sources is being explored from MeV energies up to several tens of TeV. However, above $\approx 100\,\mathrm{GeV}$, the steep spectrum does not allow to acquire sufficient statistics with space-bound experiments, which are limited in the size of the detection area. Still, gamma events are absorbed in the Earth's atmosphere and do not reach the surface. While this does not permit to measure gamma-ray photons directly with ground-based detectors, this fact is being exploited by the imaging air Cherenkov technique. The observation of so-called *air showers*, which are induced by gamma-ray events, still allows to observe such events with ground-based telescopes and at the same time offers a huge increase in events statistics, as the whole atmosphere is turned into a detection volume. In this chapter, this observation technique will be briefly discussed. Subsequently, the MAGIC telescopes will be introduced, which are a state-of-the-art ground-based gamma-ray imaging facility, and the basic principles of an analysis of MAGIC data will be outlined.

3.1 The Imaging Air Cherenkov Technique

When highly energetic particles (gamma-rays as well as charged CRs) enter the atmosphere, they interact with the atmospheric particles and induce a cascade of secondaries. This cascade increases rapidly, as long as the remaining energy per shower particle is high enough to undergo further interaction. This "cloud" of highly energetic particles is referred to as an *extensive air shower*. The size and elongation of such a shower is dependent on the energy of the primary particle. Gamma induced showers typically show a slim, spindle-shaped structure, while showers which are induced by hadronic particles feature a broader transversal spread and a more heterogeneous composition, as the contained hadronic secondary particles can cause electromagnetic sub-showers at different positions, further away from the shower axis. Typical hadronic and photon-induced cascades, which have been simulated with the Monte Carlo program CORSIKA (see subsection 3.3.2), are shown in Figure 3.1. Compared to gamma-ray showers, hadronic events of this kind are much more abundant (by at least a factor 10^3) and pose a strong background to gamma-ray measurements.

As the particles which form such an air shower are highly energetic and move with a velocity that is larger than the speed of light in the surrounding air, they emit *Cherenkov*

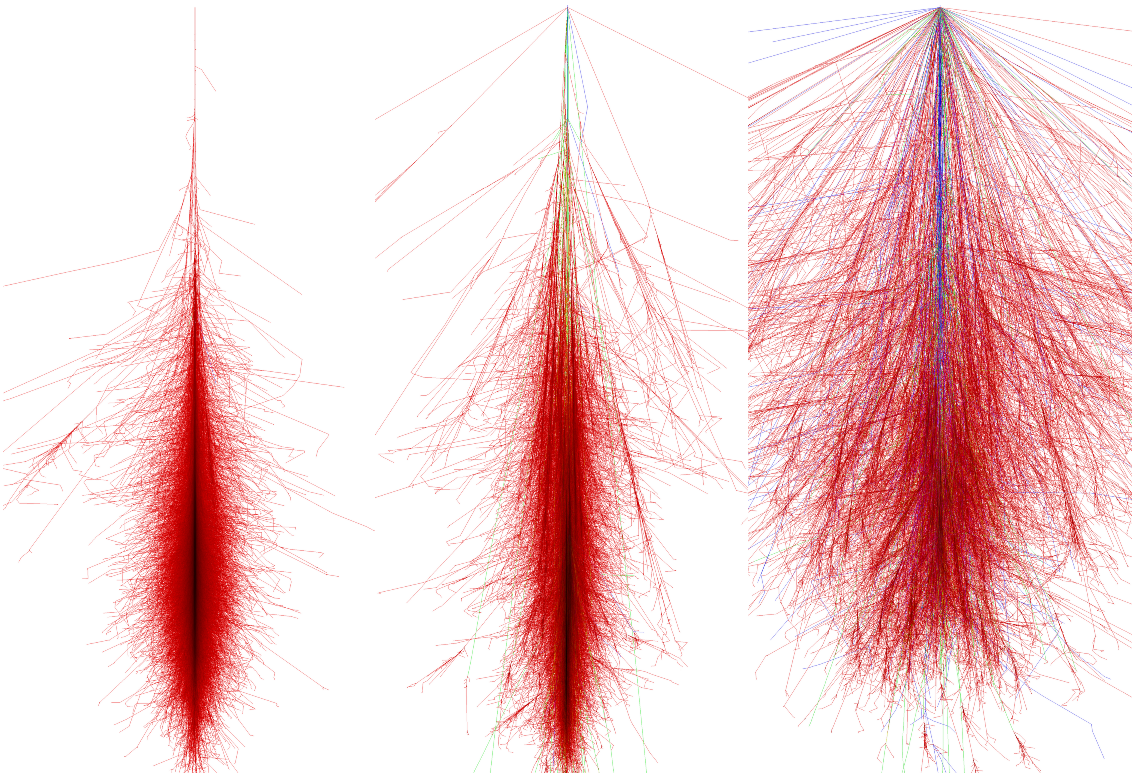

Figure 3.1: Monte Carlo simulated air showers: Shown are cascades induced by a gamma particle (left), a proton (middle) and an iron nucleus (right). All particles have been simulated with an energy of 1 TeV, entering the atmosphere perpendicular to the Earth's surface (zenith angle = 0°) and undergo their first interaction at a height of 30 km. Figure: [Sch13].

radiation. This effect creates a cone of blue to ultra-violet light, which is emitted by the shower in forward direction and can be detected by ground-based telescopes. For a more detailed introduction into the physics of air showers see e.g. [Wee03], but also [FR12] or [BG06].

After the first detectors which recorded the light emitted by gamma-ray induced air showers were built as early as 1953 [GJ53], the idea of an imaging technique was introduced in 1977 [WT77], cf. [FR12]. With the Whipple telescope, the first detection of gamma-rays from a cosmic source has been achieved in 1989 [Wo89], which made the Crab Nebula (a SNR) the first source in the VHE gamma-ray sky. After Whipple and the first stereoscopic *imaging air Cherenkov telescope* (IACT) array HEGRA (abbrev. for *High-Energy-Gamma-Ray Astronomy*), currently several Cherenkov telescope systems are in operation, namely the *Very Energetic Radiation Imaging Telescope Array System* (VERITAS, in Arizona, US) [H^+06], the *High Energy Stereoscopic System* (H.E.S.S., in Namibia) [H^+03] and the *Major Atmospheric Gamma-ray Imaging Cherenkov telescopes* (MAGIC telescopes, on La Palma de Canarias, Spain) [A^+12a].

While the next generation of ground-based gamma-ray astronomy instruments is already being planned, namely the *Cherenkov Telescope Array* (CTA) project, which will comprise of the order of 100 Cherenkov telescopes of different sizes [A+11c], the work which is subject to this thesis has been mainly based on measurements obtained with the MAGIC telescope(s).

3.2 The MAGIC Telescopes

Figure 3.2: Photograph of the MAGIC telescopes on the Roque de los Muchachos in La Palma de Canarias [Wag09].

The MAGIC telescopes are a stereoscopic system of two Cherenkov telescopes, which are situated on the Roque de los Muchachos (28.8° N, 17.8° W, 2,225 m above sea level) in the Canary Island of La Palma, Spain. The telescope has started scientific operation as a stand-alone telescope in 2004 [A+08c] and was upgraded to a two-telescope stereo-system in 2009 [A+12a].

3.2.1 Design/Construction

The telescopes are characterized by large mirror dishes of 17 m diameter, which are built from aluminum mirrors (while partly also glass mirrors were used for the second telescope dish) and feature a parabolic shape. The single mirrors can be aligned with an active mirror control system. The large mirror dishes increase the amount of light that can be collected with the telescopes, and thus allow also for faint air showers, induced by low energy gamma events, to be recorded. This way, a lower energy threshold of ≈ 50 GeV (in stereo operation) is achieved [A+12a].

In order to have a fast-moving telescope, despite its extraordinary size, the telescope frames have been built from ultra-light carbon-fiber tubes. This allows for fast repositioning of

the telescope, requiring only 20 seconds for a 180° turn in azimuth [B+09b].
The initial camera of the first telescope (hereafter M1) has been build in a hexagonal shape, of two different types of *photo multiplier tubes* (PMTs): 397 PMTs with a diameter of 0.1° have been placed in the inner part of the camera, surrounded by 180 outer pixels of a diameter of 0.2°. The second telescope (hereafter M2) is equipped with a round, homogeneous camera, built from 1039 pixels of 0.1° diameter [BT+09]. Both cameras have a diameter of 3.5°. For calibration purposes, each camera has a so-called *calibration box*, which supplies short calibration pulses during dedicated *calibration runs* and in between the data taking runs, to allow for a calibration of the individual pixels later on, see [S+02].
In 2012, when the MAGIC system was again upgraded in order to become more homogeneous, a new M1 camera was installed, which has essentially the same features as the M2 camera.
After conversion of the PMT signals from electric to optical, using vertical *cavity laser diodes* (VCSELS), and transmission through optical fibers, they are split and fed into the trigger and the read-out system in the *counting house*.
Different read-out systems were in use for M1. The system which was last used in mono mode and for the first years of the stereo operations was built from *flash analog to digital converters* (FADCs) [G+08]. For M2, a system of *domino ring sampler 2* (DRS2) chips was first used. Both systems operated at a sampling rate of 2GSample/s. In the course of the upgrade of the system in 2012, both telescopes are now equipped with DRS4 based read-out systems.
The trigger criterion for an event to be recorded consists of several steps. Each pixel is regulated by a discriminator threshold (the so-called level-zero trigger). The subsequent level-one-trigger requires an X next-neighbor (XNN) criterion to be fulfilled, which means that an event only passes the trigger if a compact group of X pixels passes the discriminator. For mono observations, usually a 4NN configuration has been applied, while for stereo observations, 3NN topologies in the single telescopes proved to deliver the best performance. In stereo observation mode, an additional stereo trigger "distills" those events, which have been seen in both telescopes [P+08]. For a detailed description of the MAGIC stereo system see [A+12a].

3.2.2 Operation

During the observation, background events stemming from hadronic showers, the light of the night sky or from diffusive electrons and gamma-ray particles contaminate the collected data sample. Although elaborate techniques are used to remove such events, still some background remains in the measurement. To get a good estimate of the contribution of this background, off-measurements are required. A practical way to obtain such background measurements is the so-called Wobble observation mode [Fo94], which permits to observe the signal region and a background region at the same time. This is achieved by pointing the telescopes not directly to the source, but to a position in a distance of 0.4 degrees next to the source. This way, an *on-source region* and one or several *off (source) regions* can be defined in the camera. Alternatively, separate on-source and off-source measurements are performed and combined later in the course of the analysis.

3.3 MAGIC Analysis

3.3.1 Analysis goals

The analysis of MAGIC data is generally performed using the standard analysis package *MARS* [M+10b].

Besides the mere detection of a gamma-ray signal from a source, the MAGIC analysis allows also to obtain the distribution of the gamma-ray flux vs. energy, the *energy spectrum*, the evolution of flux with time, which is referred to as the *light curve*, and the arrival directions of gamma-ray events in two coordinates, the so-called *skymap*. While deriving energy spectra is one of the key problems which are addressed in this thesis, and the analysis presented in chapter 6 makes use of both, energy spectra and light curves, no skymaps have been generated in the course of this thesis and will thus not be considered in the following.

3.3.2 Monte Carlo simulations

Owing to the indirect measurement technique, simulations of air shower events and the response of the telescope system are required in order to reconstruct the intrinsic properties of the recorded shower events, such as the type of the incident particle or its energy. These events are simulated following the *Monte Carlo* (MC) method and are, in the case of MAGIC, generated in three steps: The simulation of the first interaction of the incident particle, the resulting particle cascade and the corresponding Cherenkov light emission are simulated with the air shower simulation program *CORSIKA* [HKC+98]. Subsequently, the program *reflector* performs the absorption of Cherenkov photons in the atmosphere on their way to the telescope level, the reflection on the telescopes' mirror surfaces and determines which of the photons reach the camera plane. Details can be found in [Mor02]. Finally, the *camera* program simulates the response of the PMTs and the electronic system, including the characteristics of the read-out and the trigger. For details see [Bla01].

Following the energy spectral shape which is generally expected from the observed sources, the underlying spectrum of the incident particles is generated as a power-law distribution, while the range and the spectral index can be adjusted. Beside the general tuning of the telescope parameters for the MC, in order to resemble the features of the system as closely as possible, several parameters have to be adjusted based on the observational circumstances under which the corresponding data have been taken. Generally, simulations are generated for several combinations of these parameters, from which the best matching ones are subsequently chosen for a particular analysis. Alternatively, dedicated simulations can be generated, which are specifically "tailored" to the data set at hand, see [DH12, Doe09]. Among the crucial parameters is the range of the covered *zenith angles*, which is defined as the angle between the telescope's pointing position and the zenith position in the sky. Closely connected to this observation angle is the *maximum impact parameter*, which defines the furthest distance from the telescope (system) up to which showers are produced. The *impact parameter* itself is measured as the distance between the shower axis and the telescopes, projected to the ground. Another important parameter which has to be chosen carefully based on the data sample is the *point spread function* (PSF) of the optical system. According to the image defects introduced by the mirrors, this effect is also simulated in the Monte Carlo. The PSF is defined as a Gaussian spread in the $x - y$ plane of the camera.

3.3.3 Data quality selection

Prior to the actual data analysis, the data sample has to be selected according to several quality criteria, to ensure that technical defects as well as bad weather conditions do not corrupt a reliable analysis result. The general criteria for this quality selection comprise a tolerably stable trigger rate and a not too high *direct current* (DC) of the signal. The latter would indicate too much light from the night sky, which enters the measurement as noise. Regarding the weather condition, the *cloudiness* is constantly measured by a *pyrometer* and should not exceed a given limit. Furthermore, the *starguider* evaluates the night sky and monitors the *number of identified stars*. A too low number is also a good indication for poor view and thus bad data quality. For an exemplary choice of values for the parameters see subsection 6.2.1.

3.3.4 Calibration

Based on the *calibration runs*, which are taken before each data run and interlaced during the normal data-taking procedure, conversion factors (from signal amplitude to number of photo electrons (phe)) are determined for each pixel. PMTs for which the signal amplitude or the arrival time has been reconstructed wrongly are interpolated, cf. [A$^+$08c]. This step is performed with the program *callisto* or, since the upgrade of the telescope system in 2012, with *sorcerer*. This is performed for both, real data and MC.

3.3.5 Image cleaning and characterization

Subsequent to the calibration, a cleaning procedure is applied, which allows to remove all pixels from the camera image, that do not belong to the image of the shower. To achieve this, two cleaning levels are defined: The higher threshold (typically 6-10 phe) specifies so-called *core pixels*. A lower threshold is applied (in general about 3-5 phe), which leaves pixels with a content above this level in the image, if they are adjacent to a core pixel.

After this procedure, only the image of the shower remains, which is typically of an elliptical shape (but can look more complicated for hadronic showers and showers of higher energy in general). Subsequently, these shower images are characterized by a number of parameters, so-called *image parameters* [Hil85]. Among these are the parameters *width* and *length*, which describe the semiaxes of an ellipse given by the *root mean square* (RMS) of the 2-dimensional light distribution (see left panel of Figure 3.3). In this context, the parameter α describes the angle between the major axis of the ellipse and the connecting line between the center of gravity of the ellipse and the defined source position in the camera (see also Figure 3.3). Further parameters describe other properties of the image, e.g. the light content of the shower (*size*), the concentration of the light distribution (*conc*) and the *number of islands*, which is defined as the number of discontiguous light patches. These two tasks are performed using the program *star*, which is also applied to simulated and real data.

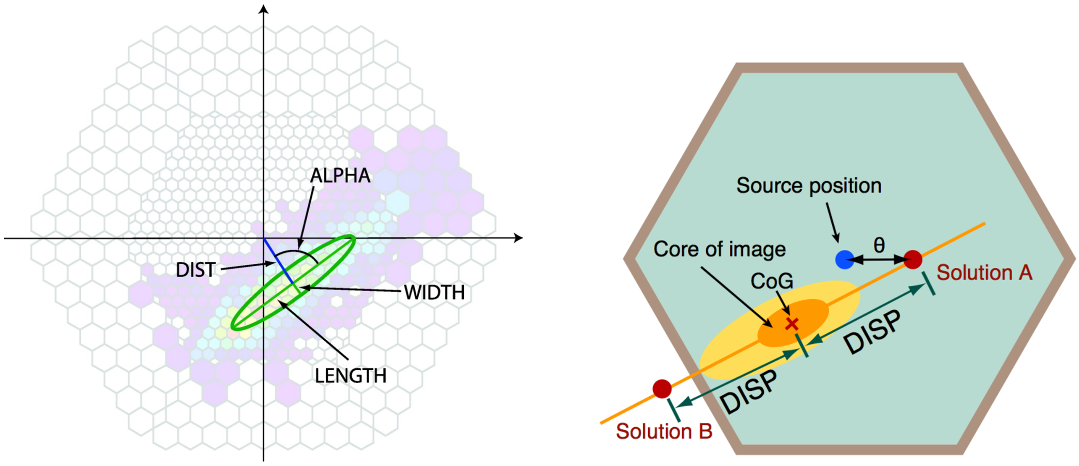

Figure 3.3: Schematic views of the definition of image parameters in the camera plane. Left panel: Basic image parameters proposed by M. Hillas [Hil85]. Figure from [A+08c]. Right panel: Reconstruction of the source position using the *Disp* method [L+01, DS+05]. Figure from [Maz07].

3.3.6 Stereo parameters

In the case of stereo observations, the program *superstar* merges the data from the two telescope pipelines and allows to determine the *impact parameter* (see subsection 3.3.2) and the *maximum height of the shower* for each event. These parameters are obtained based on the stereoscopic information and can improve the energy estimation and the suppression of the background [Feg97], see also [A+12a].

3.3.7 Background suppression and energy estimation

The sought-for gamma-ray events are dominated by a huge background of hadronically-induced shower events by about three to four orders of magnitude. However, as outlined before, development and shape of the showers are different for hadronic and pure electromagnetic showers. In the process of *gamma-hadron* (γ/h) *separation*, the data sample is filtered in order to remove a large fraction of these hadronic background events. To do this, the statistical learning method *Random Forest* (RF) [Bre01] is trained on Monte Carlo generated gamma events and off-measurements which are likely to include only a very small fraction of gamma-ray induced events. This is done within the program *osteria* (mono) or *coach* (stereo). Based on the RF, a new parameter, the *hadronness*, is created, which describes the probability for an event to be of hadronic origin. Applying the trained RFs, the program *melibea* subsequently assigns a *hadronness* value to each event, which can be used later on to remove probable hadron events from the sample by the application of a cut in this parameter. Additional constraints on other parameters, e.g. discarding images with small *size*, can help to remove events which have a low probability to be correctly classified as gamma or hadron.
While some of the image parameters are well correlated with the true energy of an event, e.g. the *size*, a new parameter, the *estimated energy*, is built as a combination of some

of the available parameters in order to achieve the best possible correlation with the true energy. This new parameter is generally also obtained via RF training on MC (gamma) events and applied to the data during the execution of *melibea*. It is used as a basis for several subsequent applications, like the reconstruction of the energy spectrum.

3.3.8 Source detection

To derive a signal, events expected to originate from the signal region need to be identified and separated from the remaining background. In the mono analysis, the parameter α offers very good separation power, as gamma-ray events which stem from the source are expected to be pointing towards the source position in the camera. Randomly distributed background events, however, are supposed to produce a flat distribution in α.
Based on this principle, the on- and off-source samples can be determined. In the case of Wobble observations, the parameter α is determined at least twice for each event: Once as α_{on} with respect to the source position in the camera, and once as α_{off}, with respect to the anti-source position, which defines the background region (see Figure 3.4). In the case of more than one background region, several α_{off} can be defined. An (energy dependent) cut in each α, which conserves only events with small α values, produces the on and off event samples.
In the case of on-source observations, α is determined with respect to the camera center. In this case, off events have to be obtained from a separate data sample.

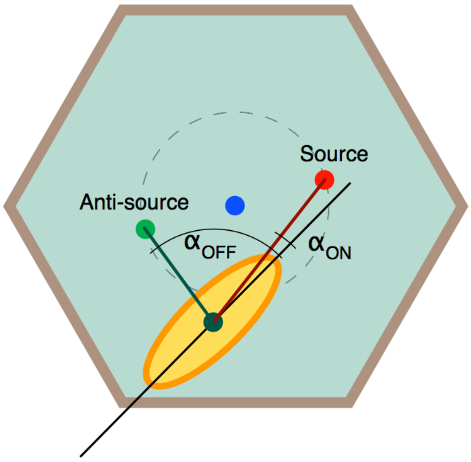

Figure 3.4: Illustration of the definition of α in the case of Wobble mode observations. Events below a certain value in α_{on}, which is defined with respect to the source position in the camera, constitute the on-source sample, while events with small values in α_{off}, which is defined with respect to the anti-source, belong to the off sample. Figure: [Maz07].

In the mono data analysis, another approach can be followed, alternatively to the α-analysis. Using the *Disp* method [L$^+$01, DS$^+$05], an estimated source position can be derived. A new parameter θ^2 is introduced, where θ describes the distance in the tele-

scope camera between the expected source position and the reconstructed source position for each event (see right panel in Figure 3.3). This way, signal and background regions can be defined via cuts in θ^2.
In the case of a stereo analysis, an improved version of the *Disp*-θ^2 method is applied: Based on the stereo image, the crossing point of the two shower axes and the two points which were estimated as the source position using *Disp* for each telescope are combined to a weighted average, which defines the final reconstructed source position (see Figure 3.5). This is again used for the calculation of θ.

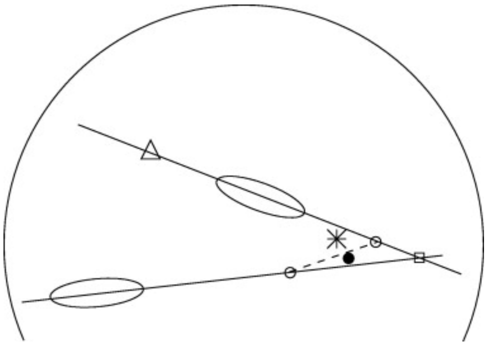

Figure 3.5: Schematic view of the improved *Disp* method for stereo observations: The open square defines the crossing point of the two shower axes, the open circles describe the (*Disp*) reconstructed source positions for the individual telescopes. The filled circle represents the weighted average of these three points, while the star denotes the true source position. The open triangle indicates the second solution for the single *Disp* reconstruction for one of the telescopes. Figure: [A$^+$12a].

With the events from the source direction in the on sample and a good estimation of the background contribution from the events in the off region, the actual signal can be derived as the number of excess events N_{exc}:

$$N_{\text{exc}} = N_{\text{on}} - N_{\text{off}}. \tag{3.1}$$

The significance of this result can be obtained according to the formula by Li and Ma [LM83], and is quoted in terms of standard deviations σ. Throughout the community, a source is agreed on to be detected when the canonical limit of $5\,\sigma$ is reached.

As outlined above, a source detection is possible based on the data distribution in α or θ^2. Furthermore, this defines the on-source sample and the respective excess for further applications. The calculation of α or θ^2 is performed within the MARS software package by *odie* (detection), *fluxlc* (light curve and preliminary spectrum) and *made-up* (preparation for spectral reconstruction with *TRUEE*, see chapter 4).

3.3.9 Reconstruction of the light curve

Based on *melibea* files, where each event features all image parameters plus an *estimated energy* and a *hadronness*, the program *fluxlc* allows to calculate the excess events, following one of the approaches described above. The necessary cuts in α/θ^2 and the *hadronness* can be set by hand or be automatically optimized by the program, in a way that user-defined *efficiency* values are met. Here, *efficiency* means the fraction of true gamma events which survive the cut, which is obviously evaluated based on MC events. A high efficiency is desirable in order to obtain good statistics in the final sample, but generally a trade-off between *efficiency* and *accuracy* has to be found, while the latter is a measure for the purity of the final sample with respect to contamination by hadrons.

Based on the MC event sample, *fluxlc* also determines the so-called *collection area* (or effective area) A_{eff} of the measurement, which represents the acceptance of the measurement process (given by the area within which events are collected, folded with the cut efficiency of the analysis) as a function of energy (and the incident angular distribution). Subsequently, the *integral flux* within a chosen energy range can be given as

$$F(E_{\mathrm{min}} < E < E_{\mathrm{max}}) = \frac{N_{\mathrm{exc}}}{A_{\mathrm{eff}} \cdot T_{\mathrm{eff}}}, \tag{3.2}$$

where T_{eff} is the effective on-source time of the considered time span. A *light curve* is defined as the evolution of the integral flux of the source versus time.

3.3.10 Reconstruction of the energy spectrum

Following the standard unfolding procedure offered by the MARS package, the first step towards the reconstruction of the spectrum can also be performed with *fluxlc*. In the same way as for the determination of the light curve, the program can set cuts in *hadronness* and α or θ^2 in order to obtain a sample of (mostly) γ events which are likely to stem from the source. For a preliminary spectrum, the differential flux, which is given as

$$\frac{dF(E)}{dE} = \frac{1}{A_{\mathrm{eff}} T_{\mathrm{eff}}} \cdot \frac{dN}{dE}, \tag{3.3}$$

is presented in a histogram with respect to the *estimated energy*. With the *migration matrix*, which gives the correlation between the *estimated energy* and the true energy as derived from the MC by *fluxlc*, this “preliminary spectrum” is converted into the actual spectrum, using the unfolding tool *combunfold*.

An alternative method has been implemented in the course of this thesis, making use of the novel unfolding program TRUEE for the first time in gamma-ray astronomy [M$^+$13]. The two spectral reconstruction procedures are presented in detail in chapter 4.

Chapter 4

TRUEE - Unfolding gamma-ray energy spectra

4.1 Unfolding - Definition and Motivation

In the course of the analysis and interpretation of data, accomplishing the leap from a set of observable quantities to the actually sought quantity is one of the most challenging tasks. In Cherenkov astronomy, one of the quantities which are looked for is the energy distribution of the gamma particles emitted by the investigated source. What can be collected by the instruments are images of the Cherenkov light distribution of the induced air showers. Image parameters like the light content or the shape of the image constitute the set of observables which yield information about the intrinsic properties of the recorded event. The correlation between the intrinsic event properties and the induced response in the instrument can be gained from MC simulations, which describe the air shower development and the detection process of the telescope. However, the true energy of each gamma-ray event cannot be determined unambiguously. Every detection process suffers from a finite resolution in the collected parameters. Due to this fact, a clear conversion from the observables back to the energy is not possible. As an example, events of a certain energy can be registered in different bins of an observable distribution. Likewise, one bin of the distribution of an observable can be filled with events of different energies. Thus, the so-called migration of events between bins has to be regarded. Additionally, the detection process is characterized by a limited acceptance. The events which are seen and detected by an instrument only account for a fraction of the particles which actually enter the atmosphere. Hence, the relation between generated and seen events also has to be derived from MC simulations and incorporated in the reconstruction of the true distribution of the gamma particle energy.

The whole process of obtaining the true distribution in a sought quantity on the basis of measured distributions in observable parameters is called *deconvolution* or *unfolding*. It includes the transformation from the space of observables to the space of sought quantities (possibly more than just one), the consideration of migration effects stemming from finite resolution and the limited acceptance of the detection process.

This problem could also be paraphrased as “finding the cause of a known effect”. This more descriptive term points to the fact that problems of this kind are summarized as the class of so-called *inverse problems*, or more maliciously *ill-posed problems*.

This chapter is structured as follows: in section 4.2, a brief introduction to inverse problems is given, followed by the presentation of methods for the solution of these kinds of problems in section 4.3. The explanations given there mainly follow [BL98] and [Blo84]. section 4.4 introduces the novel unfolding program TRUEE and outlines its functionalities, requirements and advantages. In the subsequent sections 4.5 and section 4.6, the incorporation of TRUEE into the standard analysis chain of the MAGIC experiment and its first application on MAGIC data are presented, which make up one of the key projects of this doctoral thesis. The results presented in sections 4.4, 4.5 and 4.6 have been published in [M$^+$13] in collaboration with N. Milke and the other co-authors. The description given here mainly follows the paper, but has been reworked and expanded.

4.2 Inverse problems

Problems of the above mentioned kind appear not only in astroparticle physics, but in many different fields and applications. One quite famous example is the reconstruction of images taken by the Hubble Space Telescope right after its launch. Due to a deficient mirror, the early Hubble images were distorted, but could still be used after they had been corrected by applying deconvolution algorithms. Further examples can be found in the optimization of dynamical processes in engineering and economics. What all of these different problems have in common is the indirectness of the measurement and the task to find the parameter distribution of interest by analyzing the distribution of secondary parameters which is accessible to the measurement.

Mathematically, the problem is described by a Fredholm integral equation of the first kind [Fre03]:

$$g(y) = \int A(y, x) f(x) dx + b(y). \tag{4.1}$$

Here $g(y)$ represents the distribution in the observable parameter y, which can in general be more-dimensional; $f(x)$ describes the sought distribution in the parameter of interest x; $A(y, x)$ is called *response function* and contains all properties of the detector and the measurement process as a whole and $b(y)$ represents a possible background which is present in the measurement process.

As already mentioned, the response function contains not only the correlation between the observable(s) and the sought quantity. Generally, it also describes the change in acceptance of the detector throughout the whole parameter space and the smearing between the bins of the different parameters, which is caused by the limited resolution of the detector, cf. [BL98, Blo84].

4.3 Unfolding and Regularization

In the following section, the individual steps of the unfolding procedure in general will be outlined.

4.3.1 Discretization

To get a handle on solving Equation 4.1, discretization of the problem is the first step, which permits to tackle the equation numerically. Moreover, this approach is very plausible, as the measurement itself is usually performed in a finite way with bin sizes at least as big as the resolution of the detector. Thus, all parts of the equation are discretized with respect to the measured parameter y, the sought parameter x and in case of $A(y, x)$ with respect to both of these. For distributions depending only on y, this is straight forward:

$$g(y) \longrightarrow \vec{g}: \qquad g_i = \int\limits_{y_{i-1}}^{y_i} g(y)dy, \tag{4.2}$$

$$b(y) \longrightarrow \vec{b}: \qquad b_i = \int\limits_{y_{i-1}}^{y_i} b(y)dy. \tag{4.3}$$

The distribution of $f(x)$ is not known, but needs to be determined throughout the procedure. Therefore a parametrization is required which allows to form any possible function by varying the coefficients. A convenient way to do this is to define $f(x)$ as a linear combination of a set of base functions $p_j(x)$:

$$f(x) = \sum_{j=1}^{m} a_j p_j(x), \tag{4.4}$$

with the respective coefficients a_j.
With this parametrization for $f(x)$, the core of Equation 4.1 becomes

$$\int\limits_a^b A(y,x)f(x)dx = \sum_{j=1}^{m} a_j \left[\int\limits_a^b A(y,x)p_j(x)dx \right] \tag{4.5}$$

$$= \sum_{j=1}^{m} a_j A_j(y), \tag{4.6}$$

$$\text{with} \quad A_j(y) = \int\limits_a^b A(y,x)p_j(x)dx. \tag{4.7}$$

With the discretization of the observable distributions of measurement and background (Equation 4.2 and Equation 4.3) and the discretization of the response function with respect to the observables

$$A_{i,j} = \int_{y_{i-1}}^{y_i} A_j(y)dy, \tag{4.8}$$

the integral equation becomes a matrix equation:

$$\vec{g} = A \cdot \vec{a} + \vec{b}, \tag{4.9}$$

with the vectors in observable space $\vec{g}$ and $\vec{b}$, the so-called *response matrix* A and the vector $\vec{a}$ which consists of the coefficients which define the solution $f(x)$ on the basis of the base functions p_j. The uncertainty of the measurement is given by the covariance matrix V_y. For uncorrelated measurements of events, this matrix contains only diagonal entries which represent the given measurement uncertainty. The covariance matrix of the sought quantity V_x needs to be found together with its distribution. Due to the migration of events, it is in general not diagonal, cf. [BL98, Blo84].

4.3.2 Determining the response matrix

A problem which is particularly present in astroparticle physics is the fact that the determination of the response matrix A is not straight-forward. Here, the detector response cannot be probed by test measurements of events with known energy and direction, which is the case in other disciplines. Thus, the development of the air shower itself and the detector response are generally derived from MC simulations. The response matrix is built from the simulated events according to their distribution in the sought quantity and the detector observables. After normalization, the response matrix contains the probabilities for an event in bin i of a measured quantity to populate bin j in the sought quantity.

4.3.3 Matrix inversion versus unfolding fit

Knowing the response matrix, the distribution in the sought variable $f(x)$ has to be found from the data. After discretization, this distribution is described by the vector of coefficients $\vec{a}$ from Equation 4.9.

Matrix inversion

Several approaches have been developed for the determination of $\vec{a}$. The most intuitive one is the inversion of the matrix A:

$$\vec{g} = A \cdot \vec{a} + \vec{b} \tag{4.10}$$

$$\Rightarrow \vec{a} = A^{-1} \cdot \left(\vec{g} - \vec{b}\right) \tag{4.11}$$

However, this is only feasible if A is a quadratic, non-singular matrix. In general, further methods have to be applied in order to find the solution for $f(x)$ with a given matrix A.

Least Squares Fit

In methods which avoid the actual inversion of the response matrix, the best agreement between the measured data $\vec{g}$ and the assumption of the true distribution $\vec{a}$, folded with the detector response A, is generally achieved through minimization. For example, a least squares expression can be defined and minimized:

$$\chi_0^2 = (\vec{g} - A \cdot \vec{a})^T \cdot V_y \cdot (\vec{g} - A \cdot \vec{a}) \overset{!}{=} \min. \tag{4.12}$$

Finding one $\vec{a}$, for which the expression reaches its minimum, delivers the solution $f(x)$ which shows the best agreement with the data. Strictly spoken however, using this χ^2 expression is only valid if the measured data points follow a Gaussian distribution, which is not the case for a low number of events. In that case, Poissonian statistics have to be taken into account.

Likelihood Fits

The likelihood function permits to account for measurements following any distribution, e.g. the Poisson probability density distribution, which is important in astroparticle physics measurements. For n measurements y_i of a random variable y which follow the probability density $f(y|a)$, where a is an unknown parameter on which the probability density depends, the likelihood function is defined as

$$L(a) = f(y_1|a) \cdot f(y_2|a) \ldots f(y_n|a) = \prod_{i=1}^{n} f(y_i|a). \tag{4.13}$$

The value $\hat{a}$ which maximizes $L(a)$ is the best estimate of a. What proved to be more practical is to minimize the negative log-likelihood function:

$$F(a) = -\ln L(a) = -\sum_{i=1}^{n} \ln f(y_i|a) \overset{!}{=} \min. \tag{4.14}$$

For the case of a Poissonian distribution $f(g_{i,m}; g_i)$, the corresponding log-likelihood function to be minimized is given by

$$F(a) = \sum_i (g_i(a) - g_{i,m} \ln g_i(a)) \overset{!}{=} \min, \tag{4.15}$$

where g_i is the mean value for a given solution a and $g_{i,m}$ is the number of measured events (including a possible background contribution) in an interval i. A minimization of the equation leads to the best estimate for a which considers the Poissonian distribution of the measurements, cf. [BL98, Blo84].

4.3.4 Regularization

Independently from the choice of the method, solving an *inverse problem* will often lead to a solution for $\vec{a}$ (and thus for $f(x)$) which is characterized by strong fluctuations. These fluctuations are not of a physical origin and do not stem from the measurement itself. In fact, they are inherent to the class of *inverse problems*. Generally it can be said that the fluctuations are caused by small, insignificant contributions within the response matrix, which are amplified during the process of unfolding. Thus, the solution is dominated by noise, which does not yield any information about the measured distribution. For a detailed discussion of the origin of the fluctuating results, see e.g. [Blo96].

Several methods have been developed, which allow for some kind of cleaning of the unfolding result from the above mentioned insignificant contributions. In many regularization methods, a so-called regularization term $\mathrm{Reg}(x)$ is added to the minimization term (e.g. the least squares χ_0^2), multiplied by a regularization weight τ:

$$\chi^2 = \chi_0^2 + \tau \cdot \mathrm{Reg}(x). \tag{4.16}$$

The regularization term incorporates a requirement to the smoothness of the function $f(x)$, which avoids strong fluctuations. This requirement can be realized in different ways, see e.g. [Tik63, Sch94]. The strength of the influence of the regularization can be adjusted by varying the regularization weight τ. In the above used notation, small values of τ correspond to a weak regularization, large values imply a strong influence through regularizing.

Besides the methods which follow the scheme described in Equation 4.16, other approaches are existent, which tackle the problem in a different way, but also lead to a smoother result, see e.g. [Mar82, Ber89]. In these methods, the strength of the regularization is implicitly contained in the number of steps performed to find the solution or in the use of suppression factors.

The method from Tikhonov [Tik63] shall be outlined in a bit more detail here, as it is the method of choice for the unfolding program TRUEE, which will be presented in section 4.4. Following Tikhonov, the regularization term can be chosen as the square of an operator which is applied to the solution $f(x)$. One possibility to keep the fluctuations of the solution low is to use its second derivative, which, in the discrete case, results in the so-called curvature matrix C:

$$Reg(x) = \int \left(\frac{d^2 f(x)}{dx^2} \right)^2 dx = \vec{a}^T C \vec{a}. \tag{4.17}$$

The minimization of this expression within the unfolding fit will lead to a suppression of oscillations in the resulting $f(x)$.

Although the application of regularization methods is essential in order to get a meaningful unfolding result, regularizing always implies that a part of the information gained in the measurement process is discarded. Thus, whenever regularization is applied, the main challenge is to find a good agreement between the attenuation of unphysical fluctuations and a too strong smoothing of the result, whereby unexpected features of the measured distribution can be lost, cf. [BL98, Blo84].

4.3.5 Alternative method: Forward Folding

For completeness, the method of *forward folding* shall be mentioned here, as it oftentimes enters the discussion as a valid alternative method to other unfolding algorithms. In forward folding approaches, the solution $f(x)$ is also parametrized and the best match between the observational data and an ansatz for $f(x)$ folded with the response is looked for. However, in the case of forward folding, the parametrization of the solution is built on the basis of a model with only few free parameters. This means that, within this analysis, no features of the data beyond the used model can be found, which poses a substantial drawback of the method. As an example, the forward folding for data which are expected to follow a power-law shaped distribution would start from an expression like

$$f(x, q_1, q_2) = q_1 \cdot x^{q_2}, \tag{4.18}$$

with q_1 and q_2 as free parameters, and would therefore not be sensitive for distinct features like superimposed lines or unexpected cut-offs. An unfolding method like the one presented earlier is independent from certain models and can be used to find any features present in the data within the limitations of the resolution of the measurement.

4.4 TRUEE

After this general introduction into the class of inverse problems and the outline of some methods which were developed to lift the ill-posedness of these problems, a particular unfolding program will be introduced in the following. The program is called TRUEE (Time-dependent Regularized Unfolding for Economics and Engineering problems) and has been developed by N. Milke, see also [M+13]. It is based on the unfolding algorithm which has first been implemented in the FORTRAN 77 program $\mathcal{RUN}$ (Regularized UNfolding) by V. Blobel [Blo84, BL98]. The program has been converted to a C++ version based on the ROOT framework and has been extended by several new functions. The core of the algorithm is composed by a minimum log-likelihood fit which is used to determine the unfolding result. For the suppression of unphysical fluctuations, Tikhonov's regularization method is applied (see subsection 4.3.4). The program can read the input data on event basis, either from ROOT n-tupel files or equivalent ASCII files. This way, the program holds all information in order to optimize the configuration of the response matrix to each specific case. Furthermore, possible weight distributions can be introduced prior to the unfolding, without modifying the input sample itself. Up to three observable parameters can be accounted for in the unfolding fit, which allows to combine parameters which yield complementary information.

A *test mode* and a *verification* of the unfolding result by comparing a posteriori distributions of data and MC permit to assess the quality of the unfolding result. Furthermore, the program is capable of performing an acceptance correction and accounts for possible background measurements. The different functionalities of TRUEE will be explicated in the following.

4.4.1 Parametrization using splines

As outlined in subsection 4.3.1, the sought distribution $f(x)$ can be parametrized with a set of base functions $p_j(x)$ according to Equation 4.4, to discretize the problem. A set of base functions which has proven to be advantageous for these kinds of applications are Basis-spline (B-spline) functions [Boo01]. They consist of several polynomial functions of a low degree. Cubic B-splines, which are built from four polynomials of third degree each, are used for the application presented in the following. B-splines of third order are continuously differentiable up to the second derivative, also on the points where adjacent functions overlap, the so-called knots. The differentiability is especially important for the Tikhonov regularization method as it is applied in TRUEE, as the second derivative of the parametrized solution is used here. The other great advantage in using splines is the fact that they do not show a tendency to oscillate due to the low degree of the polynomials, cf. [M+13].

4.4.2 The response matrix

In order to determine the response matrix, a set of Monte Carlo generated events, which follow some known distribution in the sought variable and which are then processed by the whole simulation of the shower development and the measurement properties of the detector, is required. These simulations need to describe the properties of the measurement process as accurately as possible, as the unfolding is based on the assumption that the relation between observables and the true variable which is derived from the Monte Carlo simulations also applies for the measurement.

The matrix A is determined based on the events contained in this Monte Carlo sample. For one sought variable and n observables which are used during the unfolding, the dimension of the matrix is $n+1$. The binning for each observable and the sought quantity are fixed at this point. Subsequently for each event, the corresponding matrix element is raised by the weight of the event. If no weights are applied, it is raised by 1. After all events are filled into the matrix, the matrix is normalized. At this point it contains all information about the migration of events between the observable histograms and the sought variable histogram as well as resolution effects. As the set of Monte Carlo events which is used here only contains events which survived the simulated trigger and the applied analysis cuts, the acceptance of the detector is not considered within the response matrix. However, TRUEE is capable of applying an acceptance correction to the unfolded event distribution, which will be explained in subsection 4.4.6, cf. [M+13].

4.4.3 Choice of observables

In most measurement processes, a large set of observable parameters is obtained. TRUEE offers the possibility to handle three of those observables at once during the unfolding itself, while most algorithms can account for only one. Naturally, parameters which correlate well with the sought parameter should be chosen for these observables. In order to investigate the correlation of the parameters and to pick the best ones, TRUEE provides correlation and profile histograms for up to 30 observables, based on the MC sample. An example for these histograms and a good selection is shown in subsection 4.6.3.

4.4.4 Parameter selection

For the unfolding itself, the definition of a number of parameters is required, while a sensible combination of these parameters is crucial to obtain a result which includes as much information from the measurement as possible while avoiding strong fluctuations stemming from the ill-posedness of the problem. The list of parameters comprises the

- number of knots,
- number of bins,
- number of degrees of freedom.

The number of knots defines the number of B-splines which are used for the parametrization (see Equation 4.4). This can be interpreted as an internal binning of $f(x)$, which is used during the unfolding fit. After the estimation of $f(x)$, the obtained distribution is converted to the final result histogram, which holds the unfolded distribution. The number of bins of this histogram has to be defined. It should be consistent with the resolution of the experiment. The third parameter, defining the number of degrees of freedom, influences the regularization strength. The relation to the regularization weight τ which has been introduced in Equation 4.16 is

$$ndf = \sum_{j=1}^{m} \frac{1}{1 + \tau S_{jj}}, \tag{4.19}$$

where S_{jj} are the eigenvalues of the curvature matrix $\mathbf{C}$ in increasing order. Each summand represents a filter factor for the coefficient with index j, which in turn describes the transformed measurement. Filter factors < 1 damp the influence of the corresponding coefficient. This is needed to suppress insignificant coefficients, which would otherwise distort the solution. As the regularization weight τ increases, the damping effect becomes stronger, while the number of degrees of freedom decreases. This way, τ can be determined indirectly in TRUEE by defining the number of degrees of freedom.

The crucial task is to find a good combination of the parameters which ensures a reasonable strength of regularizing. If the number of degrees of freedom is chosen too high compared to the number of bins, large fluctuations might distort the solution. On the other hand, if the number is chosen too low, significant information might be suppressed. In general, the number of degrees of freedom should be similar to the number of bins, while the number of knots can be larger.

TRUEE offers several histograms which facilitate this choice. One of these displays a quality value κ, which is related to the strength of correlation between the unfolded data points, for each combination of number of knots and number of degrees of freedom. This histogram is created for each number of bins of the result histogram. An example is shown in Figure 4.1. The best combinations are those which show the lowest possible value of κ. For more detail on the parameter κ and the choice of the unfolding parameters, the reader may be referred to [M+13].

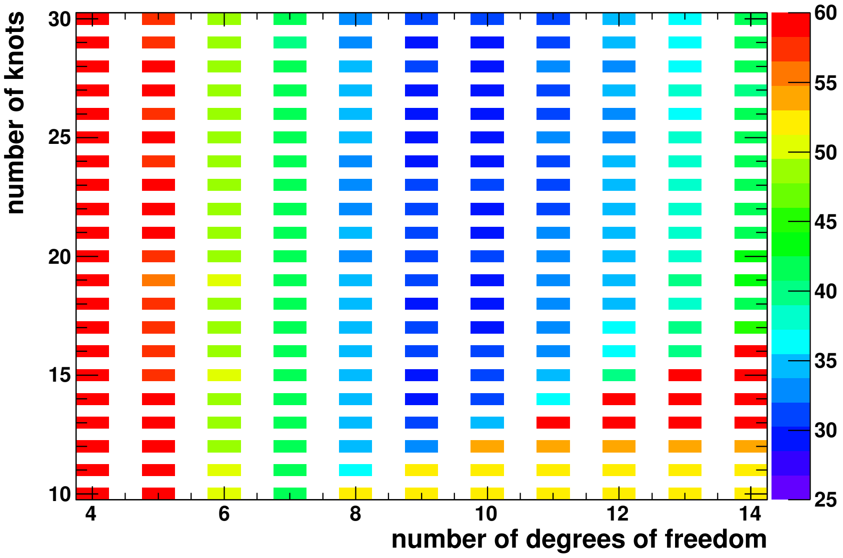

Figure 4.1: Two-dimensional histogram of the correlation-related value κ versus number of knots and number of degrees of freedom. The value of κ is given by the color scale and indicates the quality of the unfolding result. In the example given in this figure, the dependency of κ on the regularization strength (here the number of degrees of freedom) is evident. The best results with the lowest inter-bin correlation are found in the range between 9 to 11 degrees of freedom. Figure: [M$^+$13].

4.4.5 Treatment of background

Most experiments suffer from background which influences the measurement and has to be skillfully removed or corrected for. Unfolding offers the possibility for a correction of a possible background, if its distribution is either measured or well simulated. Based on a background event sample supplied by the user, TRUEE takes its contribution to the measured distribution into account during the unfolding fit (see Equation 4.11).

4.4.6 Acceptance correction

In the case of a measurement process which is characterized by a limited acceptance, the initial distribution $f(x)$ which is looked for needs to be reconstructed based on the data sample obtained during the measurement. If the acceptance losses are included in the MC simulation and the distribution function of the initially generated sample as well as the resulting event sample are known, TRUEE can perform such a correction for acceptance during the unfolding.

4.4.7 Verification with a posteriori observable distributions

A robust check for the quality of the performed unfolding and the applied simulation sample is given in the form of verification histograms. During the unfolding fit, the MC sample is folded with the migration matrix and re-weighted such that it matches the data in terms of the distributions in the observables which are used in the unfolding (up to three). For verification, the observable distributions of data and re-weighted MC are compared. In the initial samples, these do not necessarily match. After the unfolding fit, however, the MC have to reproduce the data in all observables, not only in the ones which were used during the fit. TRUEE provides such verification plots for each observable which has been introduced to the program as a part of the input sample. An example is given in the scope of the application in MAGIC, in Figure 4.7. For more details, see [M$^+$13].

4.4.8 Test mode

An additional test for the sanity of the combination of parameters can be performed in the so-called *test mode* of the program. In this mode, only the MC sample is considered. A fraction of the simulated events makes up the sample which is to be unfolded, which will in the following be referred to as *pseudo-data.* The remaining events are used as the usual MC sample. As the true quantity is known for the simulation, the true distribution can be compared to the one obtained in the unfolding. TRUEE provides histograms presenting these two distributions as well as the deviation of the two in each bin. The resulting and the true distribution are compared in a Kolmogorov-Smirnov test [CLR67] and a χ^2 test. Together with the inter-bin correlation value κ, this provides another option for choosing the best parameter combination: In Figure 4.2, κ and the obtained χ^2 value are shown for each combination of parameters. The best combination can be found where both the correlation and the deviation of the fit are low, cf. [M$^+$13].

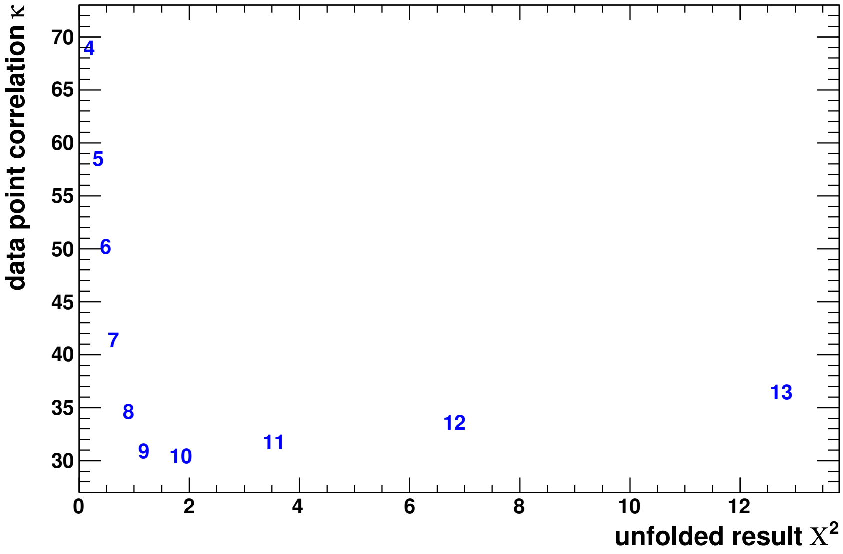

Figure 4.2: The L-curve plot: κ as a measure for the inter-bin correlation versus the χ^2 value obtained from the comparison of the true distribution to the unfolding result. The labels which indicate the bin contents are formed by the respective number of degrees of freedom. The best results are located at the kink of the curve, where both κ and χ^2 are comparably small. Figure: [M$^+$13].

4.5 TRUEE Unfolding in MAGIC

In the following section, the first application of the unfolding program TRUEE in the analysis of experimental data taken with the MAGIC telescopes will be presented. It is also the first application in the field of Cherenkov Astronomy in general and has been one of the major subjects of this thesis.

To begin with, the implementation of the unfolding in the analysis software prior to this work will be outlined and a motivation for the application of TRUEE as the new unfolding tool will be given. Subsequently, the implementation of TRUEE into the MAGIC analysis chain MARS will be presented. This includes the construction and implementation of the program *made-up*, which substitutes, for the case of an unfolding with TRUEE, the present program *fluxlc* as the spectral reconstruction tool. It is adjusted to deliver data in a form which meets the requirements of TRUEE. The implementation of TRUEE itself into the chain will be outlined and a new finishing tool, named *cure*, will be briefly described. *cure* is built to extract the desired TRUEE result and to refurbish it by generating spectral plots and by applying fits to the resulting spectrum. Finally, the application of this new unfolding chain first on Monte Carlo simulations and secondly on data of the Crab Nebula will be shown, as this source serves as the *standard candle* in gamma-ray astronomy.

4.5.1 Present MAGIC unfolding

The standard MAGIC data analysis procedure has been outlined in section 3.3 (further details can be found in [M^{+}10b]). In the following, the analysis steps of spectral reconstruction and unfolding will be discussed in more detail. These steps are executed after the calibration of the raw data, the cleaning of shower images and determination of image parameters as well as the assignment of a *hadronness* and an *estimated energy* to each event, which are obtained with the Random Forest method [Bre01], after training on MC simulations.

At present, the standard MAGIC analysis software offers to perform the reconstruction and unfolding procedure with a pipeline composed of the tools *fluxlc* and *combunfold*. The program *fluxlc* reads *melibea* files and creates a preliminary spectrum in form of a histogram of differential flux versus the estimated energy. The program applies cuts on the hadronness parameter, to obtain a reasonably pure gamma sample, on the sky coordinates of the recorded events and on θ^2 or α, to separate events from the on and the off measurement. *fluxlc* also calculates the acceptance of the detector, the effective area, using MC simulated events. Based on the estimated energy of the events, it calculates the amount of excess events and weights the resulting signal with the effective area of the detector. The products are a preliminary energy spectrum with respect to the estimated energy and the migration matrix for the chosen binning.

As the *estimated energy* is built from observable quantities, it is itself also (only) an observable. The spectrum with respect to this parameter is not yet unfolded from observational properties, as it does not account for threshold effects, possible discrepancies in the energy estimation or the limited resolution of events. Thus, this spectrum has to be unfolded in order to obtain results which are really independent from the measurement process. The macro *combunfold* offers to apply different unfolding algorithms with different regularization methods in order to produce a spectrum with respect to the true energy [A^{+}07b].

This is done via "reshuffling" of events between the bins according to the migration matrix. Additional to the unfolding, the macro permits to apply fits of several functions to the obtained spectrum, which take into account the covariance matrix and thus also the correlation of the solution, cf. [M+13].

4.5.2 Motivation for unfolding with TRUEE

The current MAGIC spectral reconstruction and unfolding, which has been outlined above, involves some limitations: The major one is given by the already fixed histogram representation of the data prior to the unfolding. This way, the binning in neither the observables nor the sought quantity can be optimized during the unfolding itself. Furthermore, all except one observable, namely the estimated energy, are discarded and cannot be used for the unfolding, although they might contain complementary information. In TRUEE, up to three observables can be taken into account during the unfolding itself and the binning in each observable as well as the result histogram can be changed and optimized during the process, as TRUEE reads event-based input files instead of histograms. Another advantage of TRUEE is its capability to include a possible background contribution within the unfolding and to perform a correction for the acceptance of the measurement process, which would otherwise have to be done outside (before or after) the unfolding procedure, cf. [M+13].

4.5.3 Incorporation of TRUEE in the MAGIC analysis chain

As TRUEE requires the information of individual events and the generation of histograms is done inside the program, it has to enter the analysis process at an earlier step than the present MAGIC unfolding program. Also, the consideration of the measurement's background and the acceptance correction do not need to be and rather should not be carried out beforehand. Thus, the output of the spectral reconstruction program *fluxlc* is not usable for a TRUEE-based spectrum reconstruction. However, some tasks which are usually performed by *fluxlc*, such as setting the analysis cuts and the separation of on region and off region events, need to be carried out prior to the unfolding. For this reason, the program *made-up* has been implemented, which serves as a preparation tool for an unfolding with TRUEE.

made-up

The program *made-up* (mc and data extraction - unfolding preparation) is designed to prepare the data in a convenient way for a subsequent unfolding with TRUEE. This includes the generation of n-tupel files, the construction of a function describing the distribution of the originally generated Monte Carlo events and the preparation of a matched template steering file for TRUEE. The structure of the program is based on the MARS program *odie*. In detail, *made-up* fulfills the following tasks:
Events are read from data and MC files, which have been processed with the MARS analysis chain up to the program *melibea*. At this point, each event is characterized by all the image parameters, an *estimated energy* and a *hadronness*.
made-up additionally calculates the θ^2 parameter for each event and checks if the data suffers from mispointing. Furthermore, the effective observation time is calculated for the

whole data sample. These routines are inherited from *odie*.
made-up applies several cuts to the events, in both the data and the MC sample:

- A cut in the *hadronness* parameter is performed in order to remove events which are very likely to stem from hadronically induced air showers.
- A cut in the θ^2 parameter defines the sample of events in the on and the off region in the telescope camera. These samples serve as the on-source measurement and a measurement of the background, respectively.
- A *zenith angle* range can be defined, in case only a sub-sample of events recorded at low or high zenith angles shall be analyzed.
- Additional cuts can be defined by the user.

For the cuts in *hadronness* and θ^2, a default is set, which is shaped according to the current standard for spectrum cuts in the MAGIC analysis. These cuts have been optimized in order to achieve a high gamma efficiency of more than 90%. In the standard chain, these cuts are applied in *fluxlc* and defined in bins of the estimated energy. As *made-up* reads analytical expressions as cuts, a fit to the given bin values has been performed, as can be seen in Figure 4.3. The analytical expression which has been derived from this fit and which is the default setting in the *made-up* steering file, is included in Appendix A.
made-up creates three ROOT trees and three corresponding output files, which are later on filled with

- on events,
- off events and
- MC on events,

respectively. As the MC sample contains only simulated gammas which are designed to stem from the source, the MC on sample is identical to a clean signal sample. So, no MC off sample is needed. All events which fulfill the cut conditions are stored in the respective output tree, either data on or off or MC on. Each of these trees contains all parameters which are relevant for the unfolding, disengaged from the MARS data tree structure, as even-level branches.
Apart from the features of the actual data events and MC events which survive the analysis up to the spectrum reconstruction, some auxiliary information is written to the output files. *made-up* reads the properties of the originally produced MC sample(s), such as the number of originally generated events N_{gen}, the maximum impact parameter r, a range for the simulated energies E_{min} and E_{max} and the slope of the generated energy spectrum γ, and stores them into an additional tree in the MC output file. If different MC samples are applied for the analysis, e.g. samples with a different zenith angle range and a therefore different maximum impact parameter, this is recognized by the program and several trees, one for each MC sample, are created.
From the data sample, the calculated effective observation time is extracted and added to the on data output file in an additional tree. These auxiliary information are needed for the acceptance correction within TRUEE.

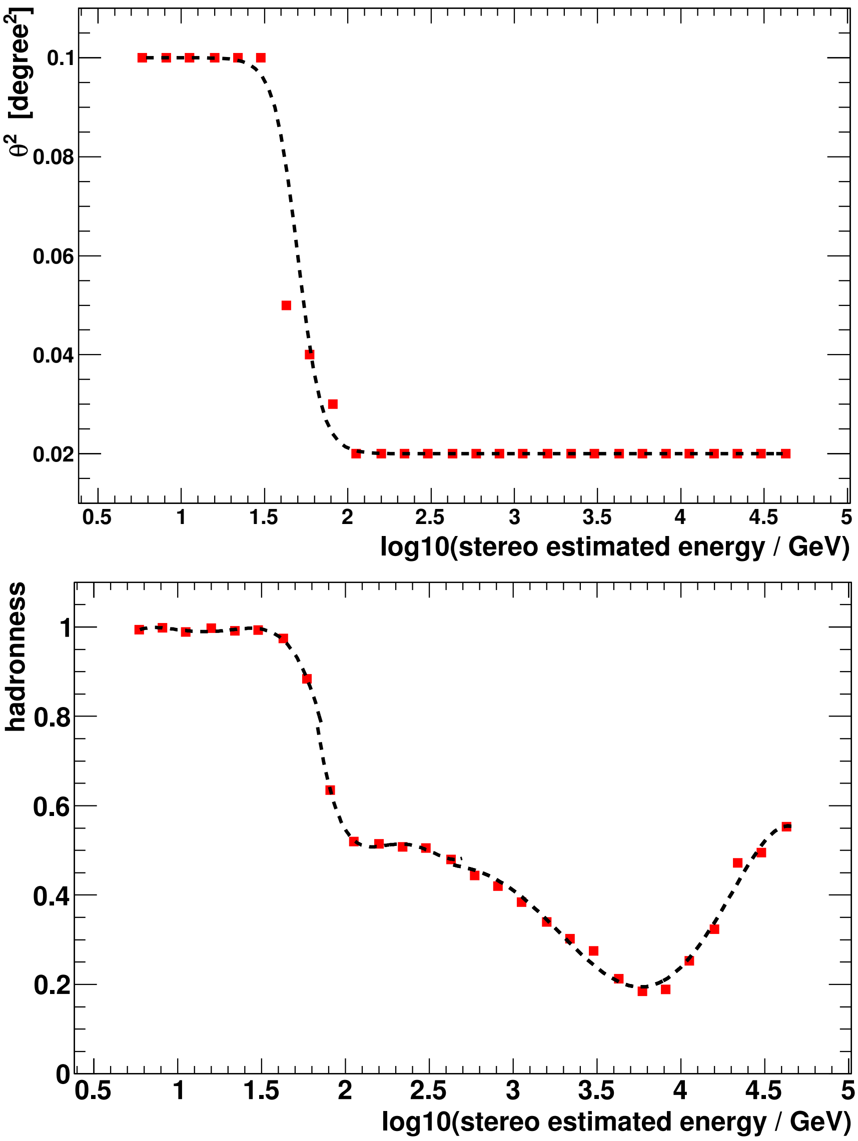

Figure 4.3: Default configuration for analysis cuts in θ^2 and *hadronness* for *made-up*. Shown are the standard cut values used in the current MAGIC spectral analysis for each bin in *estimated energy* (red squares) and the derived analytical function used in the spectral analysis with TRUEE (dashed line).

Besides the ROOT output files, a steering file for TRUEE, *truee.rc*, is created by *made-up*, in which all known paths and variables are already set. From the parameters of the originally generated MC sample(s), a function describing the distribution of these events with energy

$$\frac{dN}{dEdAdt} = K \cdot \left(\frac{E}{1\,GeV}\right)^{-\gamma}, \tag{4.20}$$

is constructed and written to the steering file. If this function is passed on to TRUEE within its steering file, the program performs an acceptance correction for the unfolded spectrum. The scaling factor K of the MC function is determined from the known parameters as follows:

$$N_{gen} = \int\limits_{E_{min}}^{E_{max}} \int\limits_{A} \int\limits_{T_{obs}} \frac{dN}{dEdAdt} dEdAdt \tag{4.21}$$

$$\Rightarrow K = \frac{N_{gen}}{r^2 \cdot \pi \cdot T_{obs}} \cdot \frac{(-\gamma+1)}{\left(\frac{E_{max}}{1\,GeV}\right)^{-\gamma+1} - \left(\frac{E_{min}}{1\,GeV}\right)^{-\gamma+1}}. \tag{4.22}$$

As the MC sample contains only a number of events, but no time span which would correspond to an observation time, the number of events are scaled to the observation time determined from the data sample. This way, the normalization of the generated Monte Carlo flux to the actual data is achieved.
If several MC samples are applied, a function is generated for each sample and the sum of the distributions is written to the file. If, instead of real data, another (independent) Monte Carlo sample shall be unfolded, some modifications have to be considered with respect to this procedure:

- No observation time can be calculated for a sample of Monte Carlo events. Thus, this parameter is set to zero in the corresponding data output tree.
- As there is no observation time for MC events, the function of the originally generated MC sample needs to be modified as well. Instead of a flux spectrum like the one given in Equation 4.20, the number of particles per energy and area are used:

$$\frac{dN}{dEdA} = \frac{N_{gen}}{r^2 \cdot \pi} \cdot (-\gamma+1) \cdot \frac{\frac{E}{1\,GeV}^{-\gamma}}{\left(\frac{E_{max}}{1\,GeV}\right)^{-\gamma+1} - \left(\frac{E_{min}}{1\,GeV}\right)^{-\gamma+1}}. \tag{4.23}$$

The usage of the program is analog to other MARS programs: Most parameters are passed to the program within a steering file (*made-up.rc*). The following cuts and file paths can be defined here:

- `Madeup.minZenith, Madeup.maxZenith`

  This allows for cuts in the zenith angle range.
- `Madeup.signalCut`

  The cut on the θ^2 parameter can be defined here. A cut depending on energy can be introduced as a function $f_{\theta^2-cut}(x)$, where x represents the estimated energy.

- `Madeup.cuts`

  All other cuts can be defined here, i.e. the cut in the hadronness parameter and additional cuts which are chosen by the analyzer. Like the signal cut, these can be dependent on the energy.

- `Madeup.dataName`

  The path in which the data melibea files are stored is given here.

- `Madeup.mcdataName`

  Here, the path to the MC files, which are used to determine the response matrix and the acceptance of the detector, is specified.

- `Madeup.outpath`

  This defines the path in which the files generated by *made-up* are stored.

When the program is launched, some additional options can be chosen:

```
./made-up [options],
```

where the options are:

- `-h`

  This help prints out a short manual, where all options are explained.

- `--config=$PATH/made-up.rc`

  With this command, the location of the steering file, which shall be used during the run of the program, is specified. The default path is `$MARSSYS/mrcfiles/made-up.rc` .

- `--ind=$DATAPATH/20*root, --inmc=$MCPATH/GA*root, --outpath=$PATH`

  The paths to data files, MC files and the output path can be given here instead of the steering file.

- `--mcunfold`

  If for testing purposes MC simulated data shall be unfolded as a kind of pseudo-data, this command has to be passed to the program. In this case, no observation time is calculated and the corresponding MC function is generated according to Equation 4.23.

- `--onlydata`

  `--onlymc`

  These commands can be used - only for test purposes - if either the MC data or the real data shall be skipped during the reading of the events. During the preparation of data for an actual unfolding, both data and MC have to be processed within one run. This ensures that both sets undergo the same cuts and that the MC function is calculated correctly.

After a successful run of *made-up*, the outpath directory should yield four new files, e.g.

- paramforunfold_data.root
- paramforunfold_bg.root
- paramforunfold_mc.root
- sugg_truee.rc,

or files named according to the user's choice. These files are processed further by TRUEE, whereat all paths and the MC properties are already included in sugg_truee.rc.

TRUEE

The incorporation of TRUEE itself in the MARS analysis package is straight-forward. After retrieving the TRUEE package, the program's source code has been added to the MARS repository in a dedicated folder *mtruee*. The main code and an example steering file are added to the MARS folder as well. For the integration and all following analyses presented in this work, the TRUEE release version 2.4 has been used.

cure

After the unfolding process, a macro can be used to extract the solution with the best combination of parameters from the result file and to apply spectral fits to the solution, which account for the correlation among the data points of the final distribution, using several selectable functions. The tool has been built based on the fitting part of the present MAGIC unfolding macro *combunfold*.

The TRUEE software itself and the preparation program *made-up* have been integrated into the MARS analysis package and are officially available in the standard release since version Mars 2-6-0. The post-processing tool *cure* is available as a macro.

4.6 First application of TRUEE in a MAGIC analysis

In the following section, the first application of the spectral analysis pipeline, which has been set up as outlined above in the course of this work, on data taken by the MAGIC experiment will be presented. By comparing the resulting energy spectrum to the spectrum derived in the course of a standard MARS analysis of the same data sample, it serves as a *proof of principle* analysis. The Crab Nebula, because of its steady emission in the VHE range also referred to as the *standard candle of gamma-ray astronomy*, is the natural source of choice for this first TRUEE application. The procedure which is reported on here is not optimized to deliver insights into the physics of the source or the performance of the telescope system. Studies of the performance of the MAGIC stereo system have been published in [A^+12a]. The analyses presented here have been performed using MARS version 2-4-13, with the additional programs introduced above.
The adjustment of the tools is carried out based on MC simulations. The used MC and data sample as well as the individual steps of optimization and verification of the unfolding procedure are discussed below.

4.6.1 Utilized data and Monte Carlo samples

Data sample

The analysis is performed on a data sample which has been collected during 7.3 hours of observations of the Crab Nebula. The observations took place with the MAGIC stereoscopic system and were carried out in wobble observation mode (see section 3.3). The data have been processed with the standard MAGIC analysis chain up to the *melibea* level, at which state the events feature all image parameters plus an assigned *hadronness* and an *estimated energy*, obtained by the application of a Random Forest trained on a MC sample. The features of the measured data sample, namely the covered zenith angle range and the number of events (before and after analysis cuts) are summarized in Table 4.1.

Table 4.1: Data sample obtained during 7.3 hours of MAGIC observations of the Crab Nebula. Given are the range in zenith angles covered during the observation and selected after analysis cuts and the number of shower events in the sample before and after analysis cuts.

Data Sample	generated	residual (after cuts)
Zenith angle range	6 - 41 °	6 - 35 °
No. events	3 457 509	18 234 (on) 12 278 (off)

MC samples

Three samples of MC events have been used during this unfolding analysis. They have been prepared by the same procedure as the data sample, while all three MC samples used here are independent from the training sample of the applied Random Forests. Table 4.2 summarizes the most relevant features of the simulated samples: The spectral index of the power-law distribution according to which they have been generated, the zenith angle range within which the events were generated and the maximum distance of the shower (at its first interaction in the upper atmosphere) from the center of the telescope system, which is known as the *maximum impact parameter*. Additionally, the sizes of the samples are given as the initial size (generated) and the remaining number of events after analysis cuts (residual). While sample A belongs to the standard sample of MAGIC MC simulations, sample B and C have been produced especially for this study, as they feature a different spectral index γ. All samples have been produced over an energy range from 10 GeV to 30 TeV.

4.6.2 Preparation with made-up: Cuts

During the preparation of both the pseudo-test unfolding and the real data unfolding, cuts have been applied to the files while processing with *made-up*. Default values have been chosen for the θ^2-Cut and the cut in *hadronness*, according to the current standard in MAGIC analysis. As the test analysis presented here is performed in the low zenith angle range, an additional cut in the *zenith angle* discards all events which have been recorded

Table 4.2: Monte Carlo simulated event samples which were used in the course of this TRUEE application. Shown are characteristics of the different samples such as the spectral index of the power-law distribution in energy, the range of zenith angles covered by the simulations and the maximum distance of the shower to the telescopes up to which showers have been generated (see text for more details). Furthermore, the total number of events before and after analysis cuts are given for each sample.

MC Sample	A	B	C
Spectral index γ	1.6	2.6	2.6
Zenith angle range	5°- 35°	5°- 35°	5°- 35°
Max. impact parameter	350 m	350 m	350 m
No. generated	7 893 000	10 000 000	40 000 000
No. residual	272 283	24 444	100 224

at an angle greater than 35 degrees. The following constraints have been applied to the data as pre-cuts:

- Size in M1 and M2 > 50
- Number of Islands in M1 and M2 < 2
- Leakage2 in M1 and M2 < 0.2.

This pre-selection is also part of the default settings in a standard MAGIC analysis.

4.6.3 Choice of observables

In principle, all observable parameters, i.e. all image parameters and event properties, can serve as input information for the unfolding. However, only three parameters can actually enter the procedure at the same time. Therefore, a selection of up to three observables had to be made, which yield the best results after unfolding. A corresponding pre-selection for MAGIC has been discussed in [Ein10].

Utilizing the check plots offered by TRUEE, the correlation of each observable with the sought variable, as drawn from the Monte Carlo, has been examined. The correlation of the parameters which have been chosen for this work are presented in Figure 4.4. It is evident that the *estimated energy*, a trained combination of observables that should by design show a very good correlation with the true energy, does exactly that. Thus, the estimated energy was chosen as the first parameter which goes into the unfolding procedure. The remaining observables show less correlation with the sought variable, some are not correlated at all. The *zenith angle* does not show a strong correlation, but it is closely connected to the acceptance of the detector and has proven to be of importance during the unfolding already in prior works, e.g. [Cur08]. Therefore, it serves as a second observable which should go into the unfolding. In order to determine the best choice of the third parameter, several trial unfoldings have been carried out, where the different image parameters nominated in [Ein10] are applied as the third observable parameter. The most

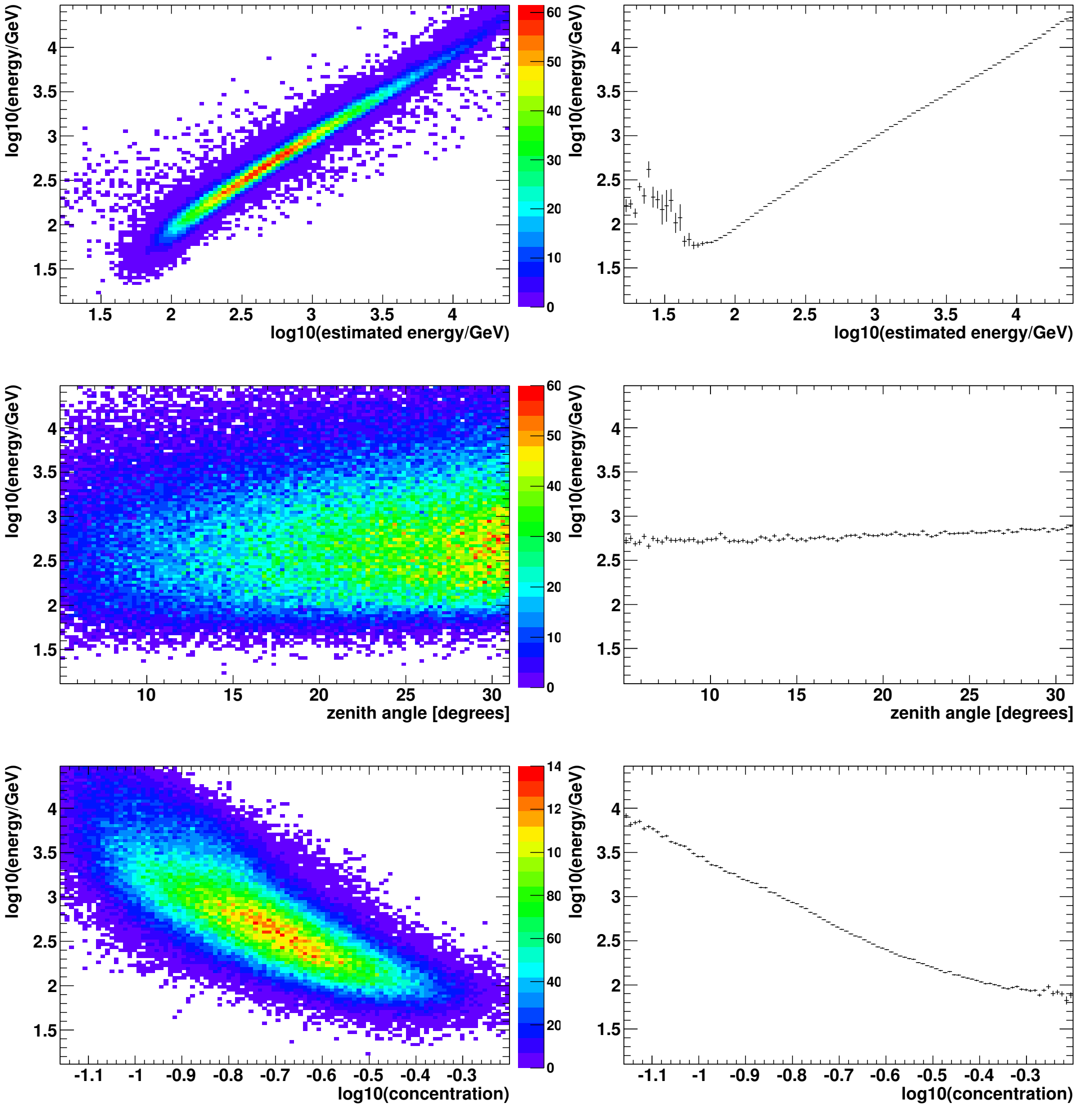

Figure 4.4: TRUEE histograms showing the correlation between several observable parameters and the (true) energy. Besides the two dimensional histograms, in which the event density is illustrated in color code (left hand side), profile histograms (right hand side) allow to locate a good correlation by a monotonically changing profile. Figures: [M+13]

stable results have been achieved when applying the parameter *concentration*, which is specified as the light content ratio of the brightest pixel versus the surrounding ones. As Figure 4.4 shows, this parameter is well correlated with the true energy, cf. [M+13].

Binnings

The bin ranges of the observables have been chosen based on the bin contents which can be seen in Figure 4.4. The range has been chosen as wide as possible, but so that a sufficient amount of events remains in each element of the migration matrix for the chosen binning. The numbers of observable bins have been varied during the test unfoldings, avoiding too low statistics in the single elements of the migration matrix. Generally, the finest binning is chosen for the parameter with the strongest correlation. The final choice of ranges and binnings is the following:

- *stereo estimated energy:* 32 bins from $\log 10(E_{est}/GeV) = 1.2$ to 4.4
- *concentration:* 15 bins from $\log 10(conc1) =$ -1.16 to -0.2
- *zenith angle:* 3 bins from $zenith\ angle = 5\,°$ to $31\,°$.

The binning of the resulting histograms has been chosen as equidistant bins in $\log 10(E)$ over the range from $\log 10(E) = 1.42$ to 4.3. With the energy resolution of the MAGIC stereo system of 17%, as stated in [A+12a], the number of bins has been conservatively set to 16.

4.6.4 Application on Monte Carlo simulated data

Before any unfolding of data is carried out, a test unfolding on Monte Carlo data should always be performed. This ensures that the used combination of unfolding parameters delivers trustable results. In the following, a standard test unfolding will be presented, where one sample of MC generated events is split in two parts: one is used as a pseudo-data sample and the other one as the regular MC sample. The best combination of parameters found in this procedure can subsequently be applied to the unfolding of real data, which is presented in subsection 4.6.5.

The test unfolding is performed based on MC sample A (see Table 4.2), while 90% of the events are used for the determination of the response matrix and 10% serve as the sample which is unfolded. This is a desirable data to MC ratio, in order to ensure that the statistical errors introduced by the MC do not exceed the ones induced by the data. The 10% which are unfolded will in the following be addressed as *pseudo-data*. As only gamma events are contained in this sample which by design originate from the position the telescope is pointing at, no consideration of background is necessary here. Thus, no background sample is passed on to TRUEE for this test unfolding. A large range of the parameters *number of knots* and *number of degrees of freedom* has been probed and the parameters have been optimized towards little correlation between the unfolded data points. For the test unfolding presented here, the following combination of unfolding parameters has been chosen:

- number of bins: 16
- number of knots: 21
- number of degrees of freedom: 13.

The resulting event distribution is presented in the upper left panel of Figure 4.5, together with the true distribution known from the Monte Carlo and the relative deviation. The distributions are in good agreement.

The result of an unfolding procedure should be largely independent of the used MC sample. To address a possible dependency of the unfolding result on the MC input spectrum, a second test unfolding is presented here: instead of using MC and pseudo-data stemming from one MC sample, which therefore share all properties such as the generated spectral slope, MC sample B has been applied as pseudo-data, which differs in the spectral index by exactly 1.0 compared to sample A. By event numbers, sample A is about 10 times the size of sample B, which is a very comfortable data to MC ratio, as mentioned above.
This study allows to investigate the influence of the deviation of spectral slopes in the applied MC sample and the sample (either MC or data) which is to be unfolded. The same combination of unfolding parameters has been used and the corresponding result event spectrum is shown in the upper right panel of Figure 4.5. Also here, a good agreement can be noted. At the highest energies, the error bars are larger than in the test unfolding presented above. This effect is due to a substantial decrease of events towards higher energies, as the spectral distribution of the pseudo-data is steeper in this case.

Beyond the unfolding of event distributions, i.e. event numbers which are distributed in bins as shown above, TRUEE is also capable of correcting for the limited acceptance of the detector, as outlined in subsection 4.4.6. To do that, the function according to which the used Monte Carlo events have been produced has to be given.
In the following, the acceptance corrected unfolding of MC sample B (pseudo-data) is presented, using sample A as MC. The applied MC function has been defined according to Equation 4.23, with the parameter values for MC sample A given in Table 4.2 and with $E_{min} = 10\,\mathrm{GeV}$ and $E_{max} = 30\,\mathrm{TeV}$. The unfolding itself is performed with the same binnings of the observables and with the same range of unfolding parameters. The lower left panel of Figure 4.5 shows the unfolded distribution together with the initial MC function and the relative deviation. The agreement is very good at intermediate energies. At the high energy end, the effect of decreased statistics appears again, which was already seen in the event spectrum and is therefore expected. However, the distribution appears to be underestimated by the unfolding result at low energies, while the corresponding event spectrum does not show such a deviation. This effect is caused by a difference in the centers of gravity of the MC sample (A) and the pseudo-data sample (B) within each bin, which is most prominent at low energies (below 400 GeV), where the event distribution of sample A steeply increases while sample B already shows a turnover (see the left and right hand side in the upper panel of Figure 4.5). This difference in the spectral index causes a shift of the center of gravity within each bin. While this does not affect the unfolding procedure itself, the acceptance correction refers to the center of gravity in each bin and is thus distorted by this shift. In order to confirm that the deviation actually stems from this effect, a third MC sample has been introduced (sample C, see Table 4.2). This set of MC simulated events has the same features as sample B, but is about 4 times larger in number. This is commonly quoted as the minimum overabundance of MC compared to data necessary to keep the statistical errors stemming from the MC low.

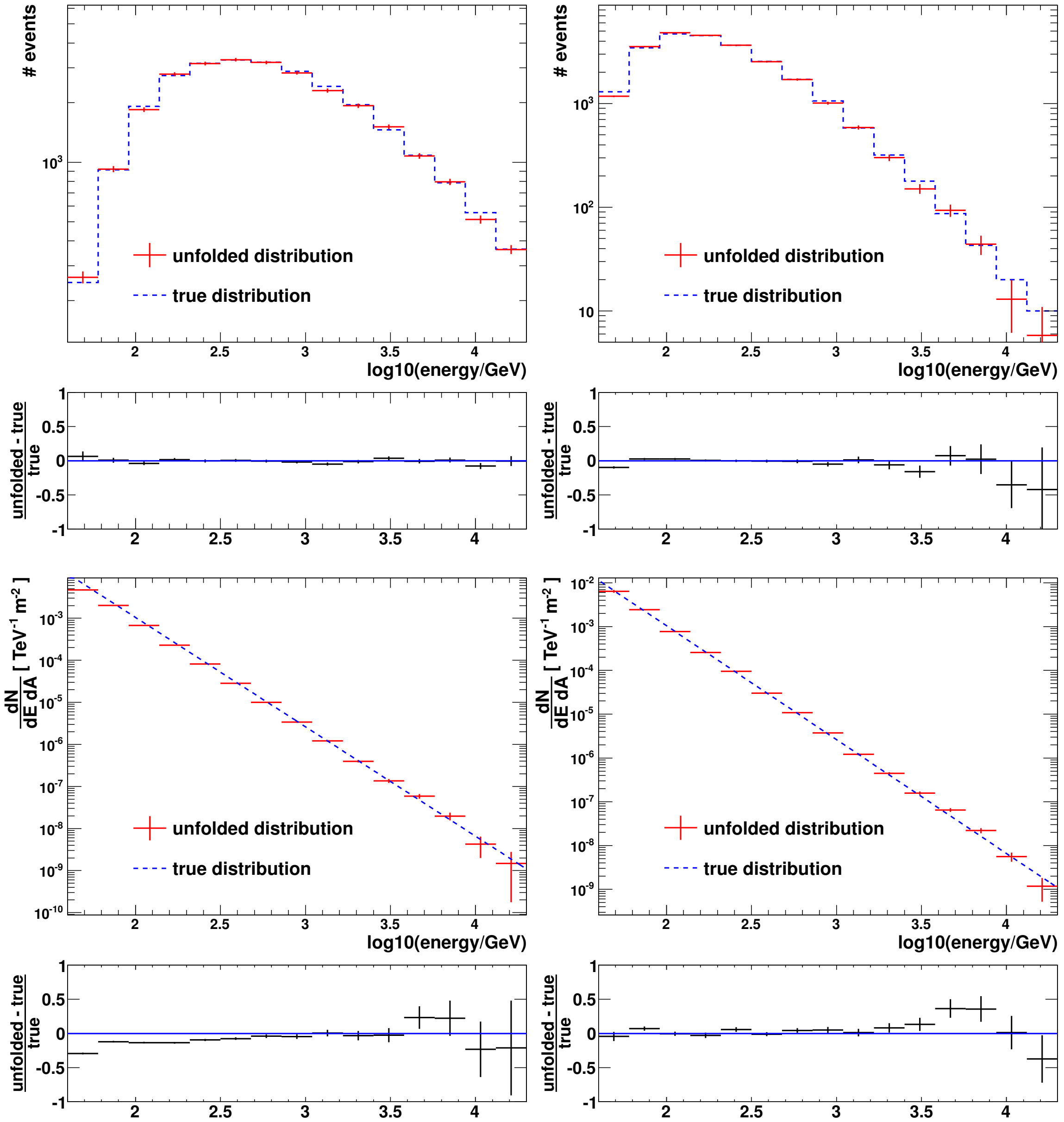

Figure 4.5: Upper panels: TRUEE-unfolded event distributions of simulated events (red points with error bars) and the true distributions (blue dashed line). Left hand side: Event distribution of MC sample A, unfolded in test mode. Right hand side: unfolded event distribution of MC sample B, while sample A is used to determine the migration matrix. Lower panels: Unfolding of MC distributions with TRUEE and built-in acceptance correction. Left hand side: unfolded distribution of MC sample B (still using sample A for the migration matrix). Right hand side: unfolding of MC sample C. For each unfolding, the relative deviation between the unfolded result and the true distribution is shown in the panels right below each figure) For details see text. Figures: [M+13].

A pseudo-test unfolding is carried out with sample C in the role of simulated data and sample B again in the role of pseudo-data. Again the same unfolding parameters used before have been applied. The resulting distribution, the true distribution and the relative deviation are shown in the lower right panel of Figure 4.5. While the deviations at high energies due to low statistics are largely unaffected by the change in the MC sample, a considerable improvement could be gained at low to intermediate energies.

It has to be emphasized that this effect is only relevant in the case of an applied acceptance correction together with a considerable difference between the distributions in data and MC. The unfolding itself performs well under these circumstances and has generally proven to do so if the deviation in spectrum does not exceed 1.0 [M+13]. It is planned to introduce a two-step procedure within TRUEE, during which an automatic re-weighting of the used MC sample is performed according to the tentative distribution present in the data. This way, the residual dependence on the MC input spectrum in the case of acceptance correction will be eliminated, cf. [M+13].

4.6.5 Application on Crab Nebula data

After the unfolding procedure has been verified by using Monte Carlo simulations as pseudo-data, the energy spectrum of the Crab Nebula is derived on the basis of the real data sample. As a cross-check, a second analysis with the standard MARS spectral reconstruction tools has been carried out. For both analyses, MC sample A has been used to derive the response of the detection process. Finally, the resulting energy spectra are compared.

In the course of the analysis with standard MARS, the prepared data sample which has been described in section 4.6.1 has been processed with the program *fluxlc*. Analysis cuts for the separation of gammas and hadrons and for the definition of the on and off data sample have been derived according to [A+12a] and applied to both, data and MC sample. The migration matrix is determined and the effective area is derived from the simulations. Subsequently, the tool *combunfold* has been used to unfold the produced histogram of differential flux versus the estimated energy, applying the derived migration matrix. All unfolding algorithms offered by *combunfold* have been tried and showed compatible results. Within *combunfold*, a power-law function has been fitted to the spectrum obtained with the regularization method of Bertero [Ber89], while taking into account the covariance matrix of the solution.

For a spectral reconstruction with the analysis chain which is subject to this work, the data are prepared with *made-up*: a cut in *hadronness* is applied and the data are split with a θ^2 cut according to the on and off region in the camera. The used cut values correspond to the one used in the standard analysis, as illustrated in Figure 4.3. Furthermore, the function describing the initial distribution of the MC sample is determined. For the unfolding, the resulting on-source event sample is passed to TRUEE as the measured data sample, while the off-source sample serves as background. As, in the case of Wobble observations with one off-region, the on and off data are recorded simultaneously and within the same time span, no additional weights have to be applied to the background sample. The MC function as identified by *made-up* is utilized by TRUEE to perform the acceptance correction. The parameters which have been found in the course of the test analysis have been applied during the unfolding with TRUEE. The resulting spectrum has been fitted (taking into account the covariance matrix), while being processed with the extraction tool *cure*.

In Figure 4.6, the resulting spectral distributions obtained with the two analyses are shown, as well as a comparison of the fit functions which have been found for the two results. Because the binning has been determined in different ways for the two analyses, no bin-by-bin comparison is possible here.

The results are in good agreement, with deviations below 11 %, cf. [M+13].

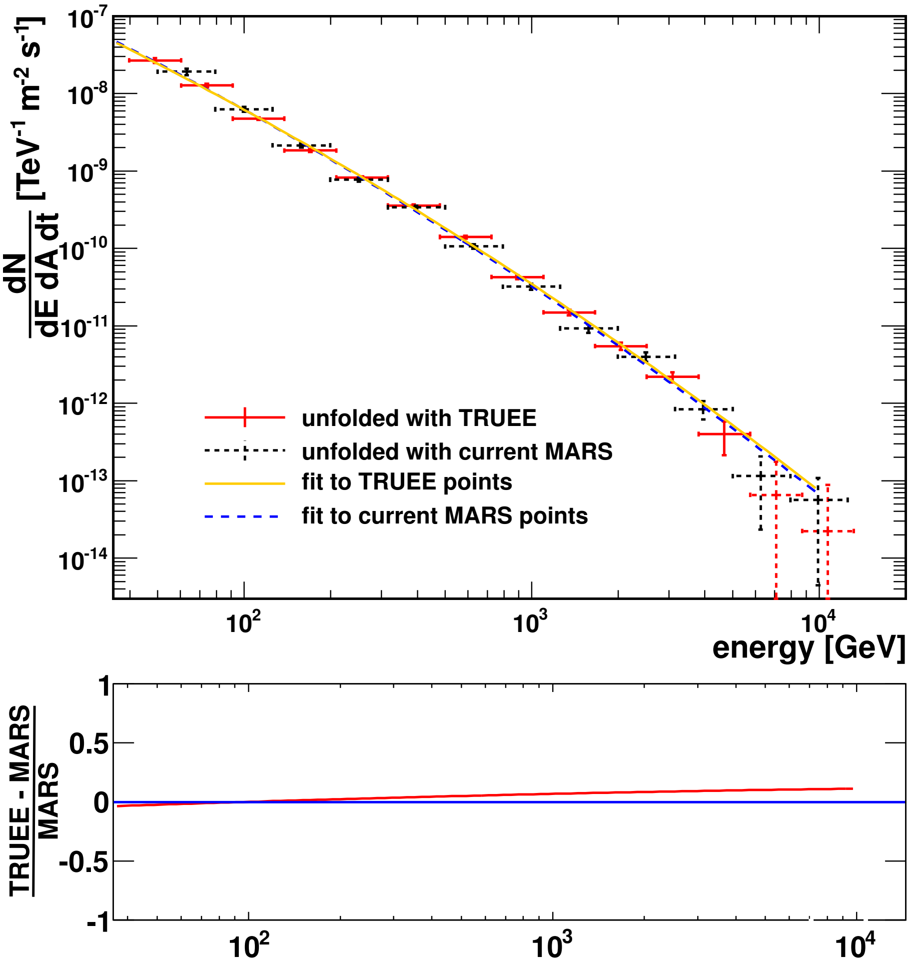

Figure 4.6: Unfolded VHE gamma-ray energy spectrum of the Crab Nebula obtained with the current MARS unfolding tool *combunfold* (black dashed points/error bars) and TRUEE (red solid points/error bars). The respective fit functions (blue dashed for *combunfold* and orange solid for TRUEE) are also shown. While the unfolding result is presented in the upper panel, the relative deviation of the two fit functions versus the energy is shown in the lower panel. Figures: [M+13].

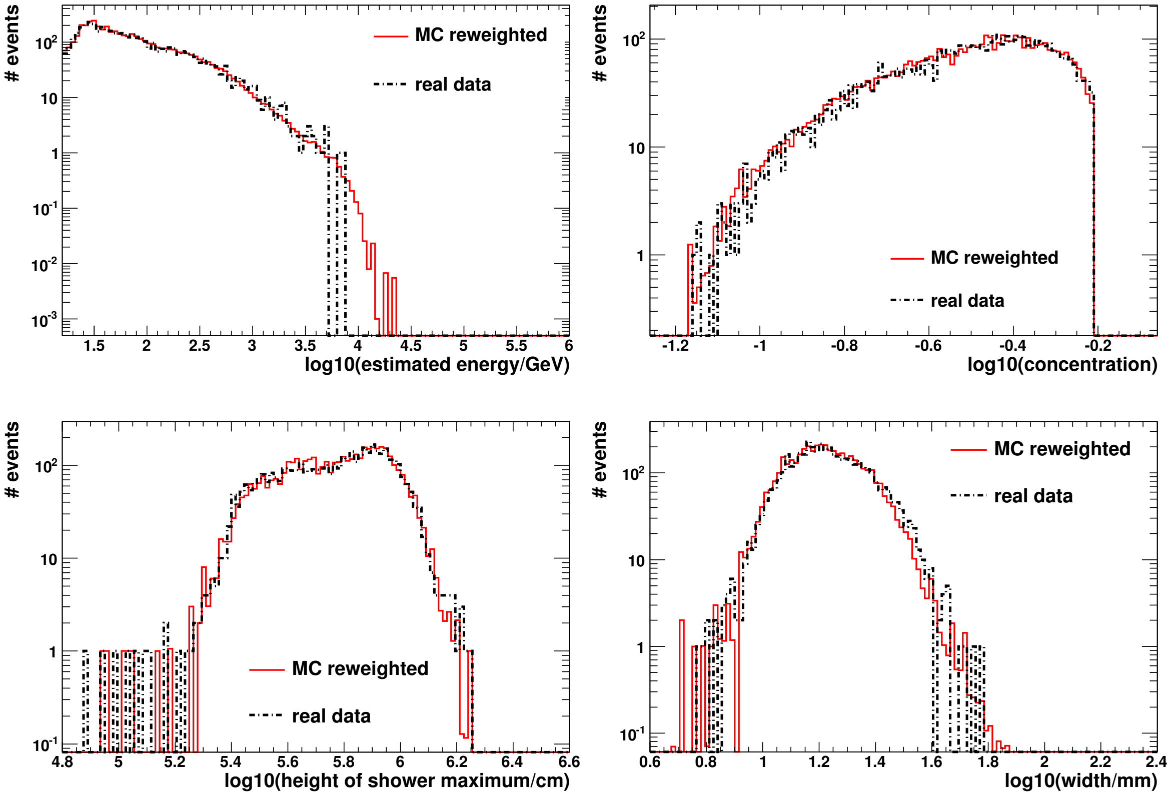

Figure 4.7: A posteriori comparison of the distributions in observable parameters of real data (black dot-dashed lines) and the (in the course of the unfolding) reweighted MC (red solid lines). In the upper panel, the distributions for two observables which have been used during the unfolding are presented, while distributions of observable parameters which have not been taken into account in the unfolding process are shown in the lower panel. Figures: [M^+13].

4.6.6 Verification using observable distributions

Independently from the various checks performed based on the MC test samples, the unfolding result obtained with TRUEE has undergone an additional verification on the basis of the distributions of observables in data and simulations, as described in subsection 4.4.7. The distributions for data and reweighted MC in two observables which have been used during the unfolding are presented in the upper panel of Figure 4.7, while the lower panel shows two parameters which have not been used. While the distributions for the former ones have to agree well by design of the method, the good agreement of the distributions in the not used observables is a strong confirmation for the compatibility of data and MC and for the quality unfolding result, cf. [M^+13].

4.7 Conclusion

Within this chapter, the class of *inverse problems* has been introduced and set in the context of today's measurement and analysis problems, underlining its importance in a wide range of fields. The common strategy for solving these kinds of problems, unfolding with regularization, has been outlined in general and the novel unfolding software package TRUEE has been presented with its functionalities and requirements. One of the key projects of this doctoral thesis has been the integration of TRUEE into the standard analysis chain of the MAGIC experiment, which has been successfully accomplished and led to a new chain of tools for the spectral analysis of very high energy gamma-ray data. The details of the implementation have been explicated in this chapter. Furthermore, the verification of the method on Monte Carlo simulations and its first application to MAGIC data have been presented. The latter one has been performed in the form of an analysis of gamma-ray data from the *standard candle* Crab Nebula, resulting in an energy spectrum of the source within this range. Beside being the first application of TRUEE in MAGIC, this has also been the very first use of the program in Cherenkov astronomy in general. The deconvolution with TRUEE has delivered good results, which have proven the method to be reliable and compatible with results obtained by methods of the current standard.

Based on the successful implementation of TRUEE into the standard MAGIC analysis, the new spectral reconstruction pipeline is now open to be used by all analyzers and presents an established and reliable alternative method to the prior standard. As TRUEE is an independent software package which will be maintained and developed further at Technische Universität Dortmund, all analyzers will profit from future improvements and expansions of the program.

By now, also other experiments in the field have expressed their interest to utilize the program in their analysis for the reconstruction of gamma-ray energy distributions.

Chapter 5

The Active Galaxy Markarian 501 - a talkative blazar in our neighborhood

5.1 Active Galactic Nuclei

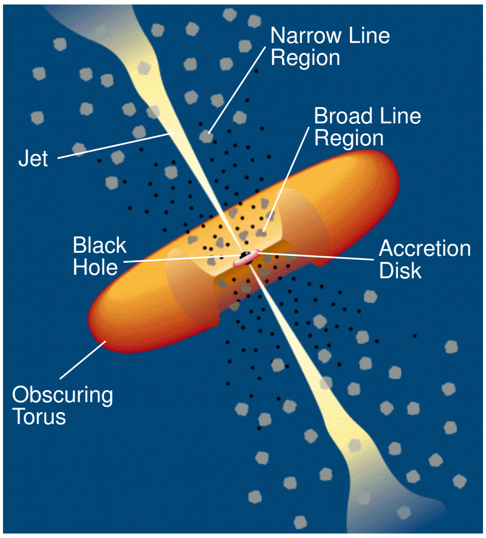

Figure 5.1: Schematic view of an active galactic nucleus as suggested by Urry and Padovani. The central engine, which is constituted by a *supermassive black hole* (SMBH) surrounded by an accretion disk, is obscured to the side by a torus of dust particles. Perpendicular to the plane of disk and torus, relativistic plasma jets can emerge, which are sources of powerful, non-thermal radiation. Figure adapted from [UP95].

Active Galaxies are defined as extragalactic objects which exhibit a strikingly high luminosity at the galactic center. The emission coming from their central region, confined to radii smaller than 1 parsec (pc), generally outshines the emission of the entire remaining galaxy, while the so-called *nucleus* can be as bright as up to 10^4 times the luminosity of the galaxy, cf. [Kro99]. This makes the centers of such galaxies, commonly referred to as *Active Galactic Nuclei* (hereafter AGN), the most luminous non-transient objects in the sky. Their overall luminosity is outvalued only by short-lived astrophysical phenomena like supernova explosions or gamma-ray bursts.

AGN are characterized by strong emission, which covers the entire electromagnetic spectrum, being most prominent at radio and optical wavelengths. They exhibit a spectrum which is essentially of a power-law shape. Except for the contribution of the host galaxy, which is known as the “blue bump” as it covers mainly the optical frequencies, most of this emission appears to be of non-thermal origin. The spectrum can exhibit distinct emission lines of varying width and strength, superimposed to the continuum emission.

The first AGN was detected in 1963 [Sch63] and was described as a star-like object, albeit being at large distance, as its spectrum showed more similarities to stellar emission than to the spectrum of a normal galaxy. More findings of objects which showed the exceptional core brightness and outstandingly strong radio emission, but were quite distinct in terms of e.g. the shape of the host galaxy, the morphology of the radio emission or the presence or absence of emission lines, resulted in a zoo of source types. Later on, the different empirically defined types of objects have been summarized in a classification scheme for AGN, suggested by Urry and Padovani [UP95].

Figure 5.1 presents a schematic view of the proposed AGN structure. The energy which is deposited in the sources’ powerful output is most likely gained from the accretion of matter onto a super massive black hole (SMBH, with $m_{\mathrm{BH}} \approx 10^6$ to 10^9 solar masses), which is located at the center of these objects, see e.g. [Ree84]. The accreting matter forms a disk which surrounds and feeds the SMBH. On larger scales, the central region is enclosed by a torus of dust particles, which obscures the central region when viewed from within or close to the plane defined by the accretion disk. Perpendicular to this plane, relativistic outflows can emerge from the central region in form of collimated plasma jets, often submerging into large cloud-like regions which exhibit strong emission in radio and are referred to as *radio lobes*. Within the jets, charged particles are assumed to travel through strong and collimated magnetic fields at relativistic velocities, which sometimes appear to be superluminal (i.e. at velocities $> c$), see e.g. [MRB83]. Strong non-thermal emission in the radio and X-ray band is seen from these jets, which is often highly polarized and is attributed to synchrotron emission from the charged particles moving within the magnetic fields. The underlying substructure, which can be seen in high resolution radio images, suggests the existence of shocks which travel along the jet axis, see e.g. [J$^+$05].

Within the scheme by Urry and Padovani, AGN are subdivided in radio-loud and radio-quiet sources, while sources classified as radio-loud are believed to comprise those AGN which exhibit relativistic plasma jets. The remaining differences in appearance, which led to the compilation of distinct classes of radio-loud AGN, are ascribed to geometrical effects. While the structure of an AGN follows a cylindrical symmetry, its appearance to the observer depends strongly on the viewing angle between the object’s symmetrical axis (jet axis) and the line of sight.

5.2 Blazars

In the AGN classification scheme which was outlined above, radio-loud AGN, for which the jet axis points close to the line of sight to the observer, are referred to as *blazars*.
The spectra which are observed from blazars generally reach from radio frequencies to very high energy gamma-rays, spanning up to about 20 orders of magnitude in energy. The *spectral energy distribution* (SED) is usually given in the representation

$$E^2 \cdot \frac{dN}{dE} \text{ vs. } E \quad \text{or} \quad \nu \cdot F_\nu \text{ vs. } \nu, \tag{5.1}$$

with the energy E and the differential energy spectrum $\frac{dN}{dE}$, or the frequency ν and the flux density per frequency interval F_ν. The typical SED of a blazar is characterized as a two-bump structure, where the first bump generally ranges from radio to X-ray frequencies and the second bump is typically most prominent at gamma-ray energies (MeV to TeV), see e.g. [BR78, UP95, UMU97, F+98a].
Probably the most striking feature of blazars is their fast variability at the highest energies, which implies flux changes by factors of up to an order of magnitude over various time scales, ranging from years down to several minutes, see e.g. [UMU97, A+07c, A+12c].

The fast variability and large luminosity seen in these sources suggest that the radiation that is being emitted within the jet is relativistically beamed towards the observer [BR78]. This can also explain the apparent superluminal motion of features in the jet, which is sometimes seen perpendicular to the line of sight. The characteristic quantity for this effect is the Doppler factor, which is defined as

$$\delta = \frac{1}{\Gamma - \beta \cdot \cos(\theta)}, \tag{5.2}$$

where Γ is the bulk Lorentz factor of the jet, $\beta = \frac{v_j}{c}$ with the jet velocity v_j and the angle between the jet axis and the line of sight θ. Relativistic beaming makes the source appear brighter ($\propto \delta^3$) , shifts the emission towards higher energies ($\propto \delta$) and shortens the apparent time scales for variability ($\propto \delta^{-1}$), cf. [BHK12]. While relativistic jets should generally appear in pairs, emerging back to back from the central region, for blazars oftentimes only one jet is visible, while the second one is dimmed by beaming effects in the opposite direction.
For such objects, the jet is often seen to begin with a bright radio feature, reffered to as the *core*. According to the current understanding, this region either corresponds to the location where the jet becomes optically thin to synchrotron emission (opacity $\tau < 1$) or to a shocked region further down the jet [BHK12, M+08].
Considering the shortening of variability time scales, the seen rapid variability still indicates, within the context of causality arguments, that the emission during states of high activity is produced in regions much smaller than the extension of the overall jet (typically with radii in the order of 10^{15} to 10^{17} cm). Together with the substructure seen in radio images, this favors the scenario of confined emission regions (so-called plasmoids), which might be caused by (or correspond to) moving shocks within the jet.

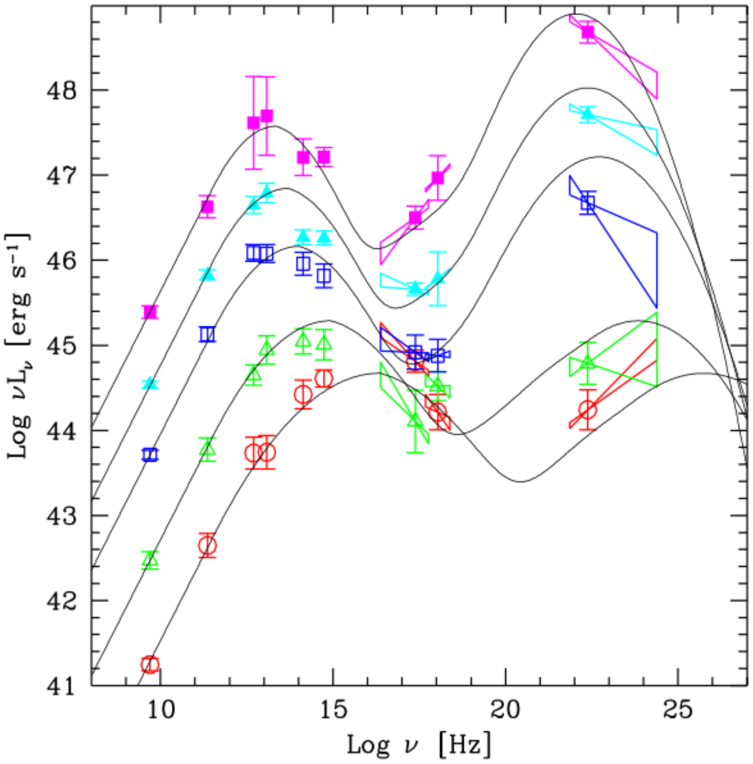

Figure 5.2: Average spectral energy distributions versus frequency of blazars which were studied by Fossati et al. in 1998. The solid lines depict spectral reconstructions which were obtained following a parametrization presented in [F^{+}98a]. With increasing overall luminosity and source power, a shift of the positions of the two peaks towards higher frequencies is apparent. Figure: [D^{+}01] after [F^{+}98a].

5.2.1 Blazar sequence

Historically, different classes of objects have been established, which are now summarized under the class of blazars. However, sources of distinct classes still show differences in several of their features, mainly their overall luminosity and the position of the bumps in the SED. Sources which have been classified as *flat spectrum radio quasars* (FSRQs) generally exhibit the peak position of the synchrotron bump at $\nu_{synchr} \approx 10^{13}$ to 10^{14} Hz, while the peak is found at higher frequencies ($\nu_{synchr} \approx 10^{16}$ to 10^{17} Hz) for sources classified as *BL Lacertae objects* (BL Lacs, named after the archetypical source BL Lacertae [N^{+}01, A^{+}07a]). Following this scheme, the class of BL Lacs has been subdivided further into *high-frequency peaked* and *low-frequency peaked BL Lac objects* (HBL and LBL, respectively [PG95]). Throughout the class of blazars, the peak position appears to be anticorrelated with the overall luminosity [F^{+}98a], see also Figure 5.2. FSRQs are generally found to exhibit much larger jet powers than LBLs and the even less powerful HBL sources. In connection to that, HBL often show slower jet velocities in comparison to more powerful sources, as seen from VLBA images, see e.g. [PPE10] and references

therein. At the same time, the presence of emission lines in the spectrum differs between these sources, ranging from strong lines seen in FSRQs to only dim or no lines in HBL objects.
The continuity in the mentioned parameters suggests a unified scheme for these different source populations, ascribing the diverse behavior only to differences in the luminosity or overall power of the sources, which appears to decline along the so-called *blazar sequence*.

5.2.2 Acceleration and emission models

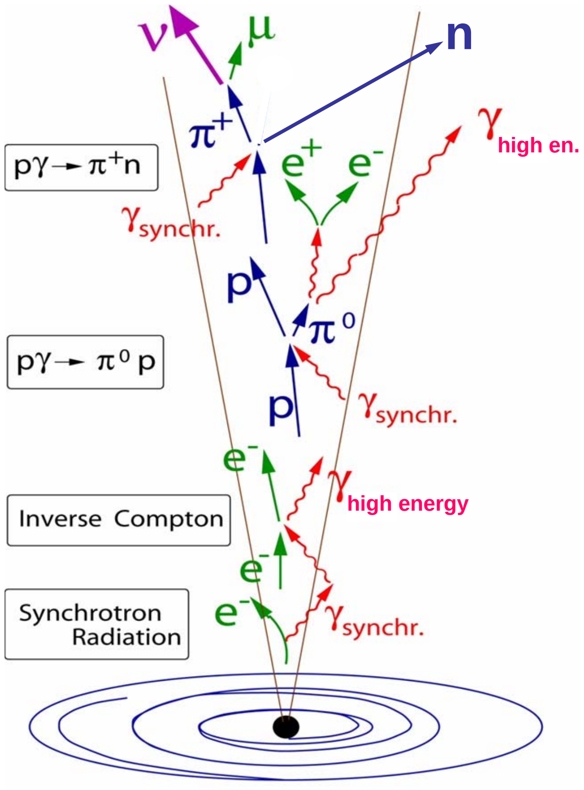

Figure 5.3: Schematic view of the processes which are thought to take place in relativistic blazar jets: electrons moving in the magnetic field emit synchrotron radiation and produce high energy photons by the inverse Compton effect, in the scope of SSC models. Following hadronic models, relativistic protons also interact with the present photon field and produce neutral and charged mesons, which decay into high energy photons and leptons, respectively, including high energy neutrinos. Possible external photon fields or proton synchrotron emission are not depicted here, although they might also play an important role in blazar jets. Figure: [KS12].

A large quantity of physical models has been developed in order to explain the processes which cause the existence of the observed SED from blazars. While most of the models agree that the first bump in the SED is caused by synchrotron emission from highly relativistic electrons which are present in the jet, see e.g. [G+98], the models differ in the

explanation of the second spectral bump. The prevailing models can be attributed to several groups:
The so-called *leptonic* models describe the high energy emission as photons which have been pushed to higher energies by interaction with the relativistic electrons via the *inverse Compton* effect. *Synchrotron self-Compton* (SSC) models suggest the interaction of electrons with their own synchrotron photon field, thus implying a strong correlation between changes in the synchrotron and the high energy emission, see e.g. [TMG98,MGC92,Böt02]. External Compton (EC) models involve the presence of external photon fields, such as radiation stemming from the accretion disk, see e.g. [DS93, SBR94].
Hadronic models assume the presence of highly relativistic hadronic particles in the jet, in addition to the present leptons, and ascribe the generation of the second SED bump to hadronic interactions. Among others, these can involve interactions of highly relativistic protons with the (electron induced) synchrotron field [MB92], with the magnetic field in the jet, producing synchrotron emission [Aha00,B⁺11] or with both [M⁺03,AD03,Man93]. Among the key parameters of these models are the characteristics of the underlying energy spectrum of the relativistic particles which cause the emission (namely the particle density, minimum and maximum energies as well as possible spectral breaks), the density of present photon fields (if not derived from the electron population within the SSC model) and general properties of the active region, such as the size of the region, the Doppler factor of the bulk motion and the surrounding magnetic field.

5.2.3 Blazars: the secrets they still keep

It can be claimed that blazars constitute the best candidates to study the source class of AGN: Based on their powerful emission which spans the entire electromagnetic spectrum up to VHE gamma-rays, they allow the observer to look down their relativistic jets, as they target the beamed emission from the most active regions directly at our instruments. Thus, blazars are the most promising objects to improve the insight into the mechanisms which govern the creation of the powerful jets and the way they are fuelled by the central engine of an AGN.
In fact, blazars make up $\approx 35\%$ of the known gamma-ray emitters at TeV energies (number obtained based on [WH13]). Still, these objects hold many open questions, such as the content and structure of the plasma jets, the cause of the strong and rapid variability and the relation between the variety of sources.

Many collected broad range blazar spectra can be well explained with SSC models (see e.g. [A⁺12b, G⁺12, Man11]). However, occasionally difficulties arise. One example is the SED of the FSRQ 3C 279, which can not be reconstructed by leptonic models, even when involving an external source of photons (EC models) [BRM09]. Another one is the occasional appearance of so-called *orphan flares*. This term describes a significant increase in the flux of the second spectral bump, while no similar event is seen in the synchrotron bump. Such events cannot be accommodated in simple (standard) SSC models. An example of such behavior has been observed for the HBL source PKS 1959-650 [K⁺04], while a similar event was also seen for Mrk 421 [B⁺05]. Recently, a claim for a similar event has been made for observations of Mrk 501 in 2009 [Pic11, NST12]. As the respective data are subject to the work presented here, this topic will be discussed in detail in chapter 6.

Hadronic models can account for suchlike missing correlations between the two bumps, but due to longer acceleration and cooling times of hadronic jet components, they tend to have problems in explaining the rapid variability seen from these sources. If strong evidence for a highly relativistic hadronic component in blazar jets is found, this would be a sensational result with a large impact on the field of astroparticle physics, as it would establish AGN as sources of the ultra high energy (UHE) cosmic rays. An alternative approach for the confirmation of hadronic interactions in blazar jets will be discussed in chapter 7.

Beside the composition of the jet plasma, also its structure is not yet fully understood. With the technique of high resolution radio interferometry it is now possible to study the jet with a resolution smaller than the size of the jet itself. Recent observations of the LBL source BL Lacertae and the FRI galaxy M 87 suggest that the highest activity takes place in the parts of the jet close to their central engine [M+08, A+09b]. Complementary polarization measurements of several FSRQs and LBLs suggest a connection of changes in the jet polarization and the occurrence of flares [A+10, M+08, M+10a]. However, a complete understanding which is independent from single objects or subclasses still needs to be found.

Another topic of current research is the relation between the different blazar subclasses, which is connected to the aforementioned blazar sequence. Although suggested already in 1998 [F+98a], the relation between the different appearances of blazars is not fully understood and is subject to debates, see e.g. [Fin13, M+12b]. Detailed investigation of the variability behavior in connection with the overall spectral output and the radio morphology of sources of the different classes are required to pin down the intrinsic mechanisms which might unify the observed properties.

Beyond the opportunity to gain a better understanding of the astrophysical phenomenon of AGN, the class of blazars also offers the ideal cosmic laboratory to study the physics of the highest energies. The highly energetic output in combination with their far distances offers to address more fundamental questions, such as the search for quantum gravity, Lorentz invariance violation or the existence of axions [A+08b, Ste04, H+12]. Prior to that however, the intrinsic properties of the sources need to be well understood.

5.3 Markarian 501

The AGN Markarian (Mrk) 501 is a prominent member of the class of blazars. It is located at RA=16h 45m 52.22s, Dec= 39° 45’ 36.6” with a measured redshift of z = 0.034, which corresponds to a distance of 1.4×10^8 pc or 4.7×10^8 light years. As the third object (and the second object beyond our galaxy) it has been detected in VHE gamma-rays in 1995 [Q+96, B+97b], after the detection of the Crab Nebula [Wo89] and the first VHE blazar Mrk 421 [P+92]. Based on its SED, Mrk 501 has been classified as an HBL according to the scheme proposed by Padovani and Giommi [PG95]. It is known as one of the most extreme blazar sources, showing very strong and fast variability (and thus appearing to be a very *talkative* object).

Soon after its detection, the blazar appeared to be in an exceptionally high state in the year 1997, when its emission above 350 GeV was at a level of 10 times the flux of the Crab Nebula [C+97]. This event was thoroughly studied in the VHE range, also looking into correlations with the X-ray band (see also [S+98a, A+99a, A+99b, DA+99]). During the large flare, the synchrotron bump has been found to peak at or above 100 keV, which indicates a shift of the peak by at least two orders of magnitude compared to its usual position [C+97, P+98, T+01]. Moreover, a significant correlation between flux variations in the gamma-ray and X-ray regime was found, which can be well reproduced by one zone SSC models. After a period of quiescent emission, the source was seen in a flaring state again in 2005, when an increase in flux by a factor of 2 on time scales down to two minutes was measured [A+07c]. Generally, throughout the prior observations, the source spectrum in the VHE range appeared to be harder when the source was bright, see e.g. [A+07c].
VLBA images of Mrk 501 revealed a comparably slow moving jet which is characterized by a *limb brightening* structure [PPE08, P+09].
Numerous MWL campaigns have been conducted on Mrk 501, see e.g. [P+98, K+00b], and the collected data could be well reproduced within the framework of SSC models [T+01]. However, the allowed range of the model parameters is still wide, as the collected data were too sparse (both in frequency coverage and time) to put strong constraints on the parameter ranges, see e.g. [M+12a]. The fast variability seen in 2005 is a strong argument in favor of a comparably small emission region (with $R \approx 10^{15}$ cm) [A+07c]. Still, the low state of the source can be accommodated for by assuming regions which are larger by one or two orders of magnitude in radius, see e.g. [A+11b]. This might also suggest that more than one region is involved in the emission and thus points to more complicated (two zone) models. The substantial shift in the synchrotron peak and the *harder when brighter* behavior suggest a change in the electron energy distribution as the cause for the seen flaring events [P+98], but also long-term changes in the size of the emission region or the Doppler factor are being discussed [M+12a].
The fast variability in gamma-rays, together with a comparably slow apparent motion of the jet in radio images, gave rise to the so-called *bulk Lorentz factor crisis* [HS06], which suggests separate regions to be responsible for the emission in radio and gamma-rays. This could for example be accounted for by a *spine-layer model* [GTC05], involving a structured jet with a fast moving central component and a slower sheath. While other explanations are being discussed, the limb brightening seen in VLBA images would favor this scenario.

All things considered, clear constraints on the properties of the active regions and the involved particle populations, and possible changes of these parameters with time, are still to be found. Beyond that, hadronic models are still not ruled out, although leptonic models seem to explain most seen phenomena.

In chapter 6, a multi-instrument analysis will be presented, which was conducted in order to shed light on the mechanisms behind the source's broad-band spectral variability. A view on Mrk 501 in the scope of hadronic emission models will be given in chapter 7, focussing on the possibility of using large-scale neutrino detectors to search for the debris of hadronic interactions in the blazar.

Chapter 6

MWL Campaign on Mrk 501 in 2009

6.1 Motivation and Introduction

The blazar Mrk 501 is an excellent candidate source to study the intrinsic behavior of AGN: with a redshift of $z = 0.034$, it is one of the closest extragalactic TeV gamma-ray sources we know. Therefore, the produced gamma-ray emission has undergone only weak attenuation by pair production with the Extragalactic Background Light (EBL, see subsection 2.1.2) at the time when it reaches the Earth, which adds only a small uncertainty to the measurement of the intrinsic source spectrum. Additional to its proximity, the source is bright and very variable. Thus, spectral changes within quiescent and flaring periods can be investigated.

In order to get the best possible view of the overall behavior of blazars, so-called *multi-wavelength* (MWL) or *multi-instrument campaigns* are organized. At best, these include instruments distributed over all wavelengths of the electromagnetic spectrum, which observe the source simultaneously or at least over the same time span. Although such campaigns have been organized for a long time already, see e.g. [C+97], the mechanisms by which the seen gamma-ray emission is produced and the variability of the overall spectral energy distribution of the source are not yet fully understood (see chapter 5). One reason for this is given by the fact that the previous generation of gamma-ray instruments was not sensitive enough. Recently however, the possibility to study the entire high energy peak of the SED has improved substantially. The *Fermi* satellite was launched in 2008 [A+09c] and its on-board gamma-ray detector *Large Area Telescope* (LAT), together with the state-of-the-art IACTs (MAGIC, H.E.S.S. and VERITAS), provides a complete sampling of the high energy SED bump. The low energy threshold of MAGIC even allows for a cross-calibration of the LAT and the IACT measurements at around 100 GeV. With this improved coverage, which affects especially the measurements of the high energy bump, new MWL campaigns are able to constrain models further.

In this chapter, a multi-instrument campaign on Mrk 501 is presented. The campaign was conducted in the year 2009 over a time span of 4.5 months (lasting from March 15^{th} to August 1^{st}) and comprised the participation of 30 different instruments, covering all wavebands from radio to VHE gamma-rays. MAGIC took part in this campaign as one of three VHE instruments. The presented MWL data set led to one previous publication, which was focused on the presentation of the data set itself and the spectral energy density (SED) combined from all instruments' measurements, averaged over the whole duration of the campaign [A+11b].

One of the key projects of this thesis has been the variability analysis of this MWL data set, with a particular focus on the changes in flux and the spectral shape with time in the course of the campaign.

The relevant MAGIC data have been among the last which were taken in the single telescope configuration, as shortly after (fall 2009), MAGIC began the operation as a stereoscopic system. The data have been re-analyzed in the course of this work and the results are presented in the following section. As the novel spectral analysis chain, which was presented in chapter 4, has been implemented for the analysis of MAGIC stereo data, only the standard MAGIC analysis tools have been used here. The data from the remaining instruments have been supplied by analyzers of the corresponding experimental groups as light curves (flux versus time) and energy spectra (flux versus energy), while spectra for shorter periods or single observations were only available for those instruments where the acquired event statistics were high enough. The results drawn from this data set are presented subsequently (section 6.5 and following). Finally, the results are discussed and put into context of the current state of knowledge of this source, the source type and possibly related source types.

The results which are shown in this chapter will be presented in a second multi-author publication, signed by all participating collaborations, which is led by the author of this thesis [A+13].

6.2 MAGIC data analysis

A first analysis of the MAGIC data taken on Mrk 501 during the reported MWL campaign has been carried out by D. Tescaro in his PhD thesis [Tes10]. It resulted in the broad-band energy spectrum presented in [A+11b], which averages over the whole data taking period. In the course of this work, the data have been re-analyzed, as deeper studies regarding the variability, both in flux and energy spectrum, were needed. In that process, a repeated quality selection of the data was desirable. The analysis configurations have been verified on a data sample from the Crab Nebula.

6.2.1 Data selection

The initial set of MAGIC data from Mrk 501, which is chosen for this analysis, contains all observations from the time window of the campaign which were performed in Wobble observation mode and at comparably small zenith angles (below 35 °). In that time span, only few higher zenith observations were carried out and only some observations were performed in *on source* observation mode (in the course of the commissioning of the second telescope). These data runs have been discarded in order to establish a homogeneous data sample. The initial data set has undergone quality selection cuts, as presented in Table 6.1 (see also subsection 3.3.3). The chosen dates of observation are listed in Table 6.2. The total observation time of this sample amounts to 16.8 hours.

Table 6.1: Properties of the collected MAGIC Mrk 501 data sample and quality selection cuts which have been applied to the sample, prior to the analysis. For details on the individual parameters see subsection 3.3.3.

Parameter	Cut value
Zenith range	$6^\circ < \mathrm{Zd} < 35^\circ$
Observation Mode	Wobble
Cloudiness	< 40
No. of identified stars	> 10
DC currents	$< 1500\,\mathrm{nA}$
Trigger rate	stable, above 190

Table 6.2: Nights of observations which are represented in the final data sample used for the presented analysis. Following a convention which is used throughout MAGIC, the date of the following day (sunrise) is given for each night. For the given nights, observations have been performed as part of the MWL campaign and delivered data which (partly) survived the quality cuts given in Table 6.1.

Month	Days
March	23., 31.
April	1., 2., 3., 4., 5., 17., 18., 19., 20., 23., 24., 25., 27.
May	22., 24., 27.
June	14., 29.
July	23., 26.

6.2.2 Off-data sample

The data set, which serves as the “hadron training sample” for the Random Forest trained for gamma-hadron (γ/h) separation (see subsection 3.3.7), is built from observations of weaker sources, which were also taken in Wobble observation mode, around the same period and in a similar zenith angle range as the Mrk 501 observations. The used sources and observation dates are summarized in Table 6.3. The data have undergone the same quality selection as the Mrk 501 sample.

6.2.3 Monte Carlo selection and RF training

For this analysis, the standard MAGIC Monte Carlo simulations have been used. According to the telescope configuration at the time of data taking, single telescope simulations with FADC read-out and Wobble observation mode have been chosen (see also subsection 3.2.1 and subsection 3.2.2). MC with several point spread functions were available, and 14.8 mm was chosen according to the monitored PSF of the telescope (see Figure 6.1). The set of MC files has been split into a train and a test sample. The train sample serves

Table 6.3: Set of observations which constitute the hadron training sample for the (γ/h) separation RF: Given are the observed (comparably weak) sources and the dates (nights) of observations which survived the quality cuts given in Table 6.1.

Source	Month	Days
1H1722+119	March	30., 31.
	April	5., 6.
2MASX0324+34	January	13., 15.
MS1050	March	19., 20., 23.
	April	1.
PKS-1222+21	April	20.
PKS1424+240	April	17., 19., 21.
	June	15., 22.

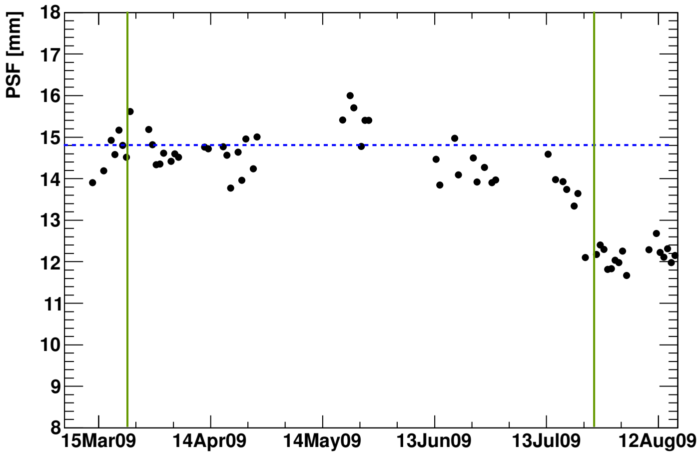

Figure 6.1: Measurements of the Point Spread Function (PSF) of the telescope around the time of the Mrk 501 observations (black dots). The vertical solid green lines define the time window in which the MAGIC observations have taken place. The blue dashed line indicates the PSF of the chosen Monte Carlo simulated events.

as the gamma sample for the γ/h separation training, while the test sample is used later for the spectral reconstruction.

Three RFs have been trained with the MARS program *osteria*. The standard configurations have been used. The RF to estimate the probably for an event to be of hadronic origin, the so-called *hadronness*, was trained on MC and off-data, building 100 trees. RFs which generate a *disp* and an *estimated energy* for each event, have been trained only on MC simulations, with 50 trees in both forests.

6.2.4 Flux variability analysis

Using the program *fluxlc*, light curves have been produced, presenting the evolution of the source's integral gamma-ray flux with time. The parameter α has been used to define the signal and background region in the camera (see subsection 3.3.8). After optimization on the Crab Nebula data, the following cuts have been applied during this procedure:

- $\alpha < 8$,
- size > 150 phe,
- hadronness cut efficiency 0.7,

while the actual cuts in hadronness have been determined by the program such that the quoted efficiency is reached. Three off regions in the camera have been used to determine the background of the measurement.

The light curve was produced within the energy range from 300 GeV to 50 TeV for reasons of comparison (see Figure 6.2), as in the course of the first analysis of this data, an overall light curve in the same range has been obtained and the light curve determined by VERITAS (see section 6.5) covers the same range. A comparison to the light curve obtained in [Tes10] and from an additional cross-check by N. Nowak is shown in Appendix B.

In the overall light curve, a significant increase in flux can be seen on the 22^{nd} of May, which slightly exceeds the flux level of the Crab Nebula, showing 1.1 Crab Units (C.U.), while the baseline flux is at the level of about 0.3 C.U.

To address the variability in different bands, light curves within different energy ranges (160 GeV to 500 GeV and 500 GeV to 10 TeV) have been investigated, while 160 GeV and 10 TeV correspond to the lower and upper threshold of the analysis, respectively. The *hardness ratio*, which is defined as the ratio of fluxes in two different bands, is presented in Figure 6.4, together with the two light curves. Due to the large uncertainties in the light curves, especially for short observations, also the hardness ratio shows comparably large error bars there. A fit of the hardness ratio distribution with a constant delivered a $\chi^2 = 12.51$ for 14 degrees of freedom, while the mean value is compatible with 1. The corresponding probability for the data points to be compatible with a constant flux is 57%. No significant change in the hardness over time can be stated.

To investigate possible intra-night variability on the day of the large flux increase, May 22, a light curve with a bin size of 5 minutes has been produced from the data of that night (see Figure 6.3). In this light curve, only marginal differences in the flux can be seen. A constant fit to the light curve yields a reduced χ^2 of 7.86/6 and thus a fit probability of 25%. Therefore no strong and rapid variability can be concluded.

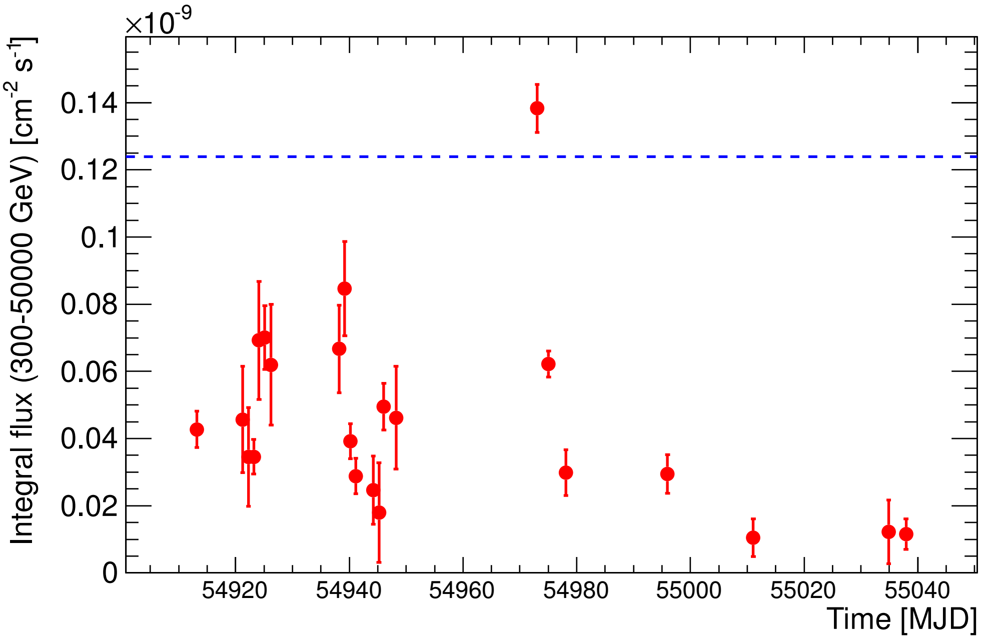

Figure 6.2: Light curve derived from the MAGIC Mrk 501 observations: The integral flux in the range 300 GeV to 50 TeV is shown. This light curve is also included in the MWL light curve collections in subsection 3.3.3. The blue dashed line indicates the flux of the Crab Nebula in the given energy range.

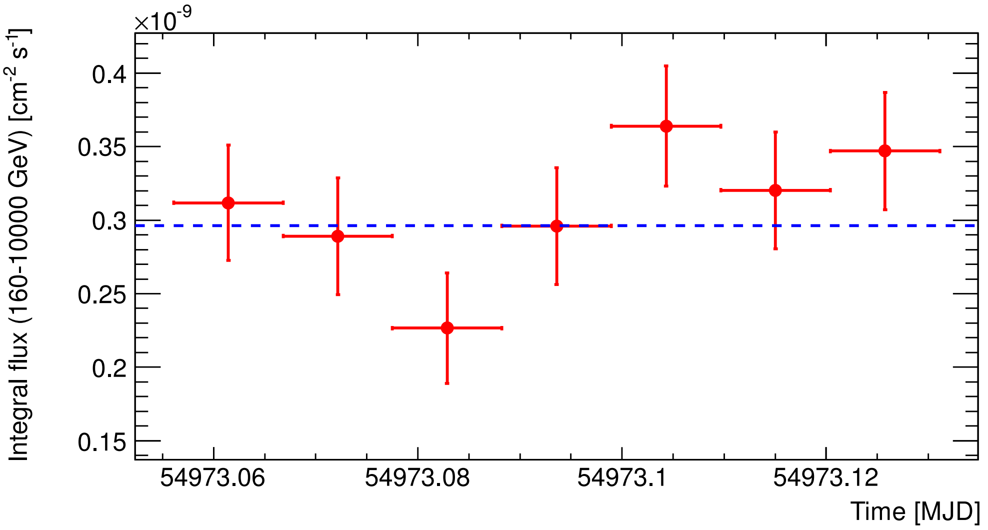

Figure 6.3: Intra-night light curve of the observations of Mrk 501 on May 22nd 2009 in the energy range 160 GeV to 10 TeV. The size of the individual time bins has been chosen as 5 minutes. The blue dashed line indicates the flux of the Crab Nebula.

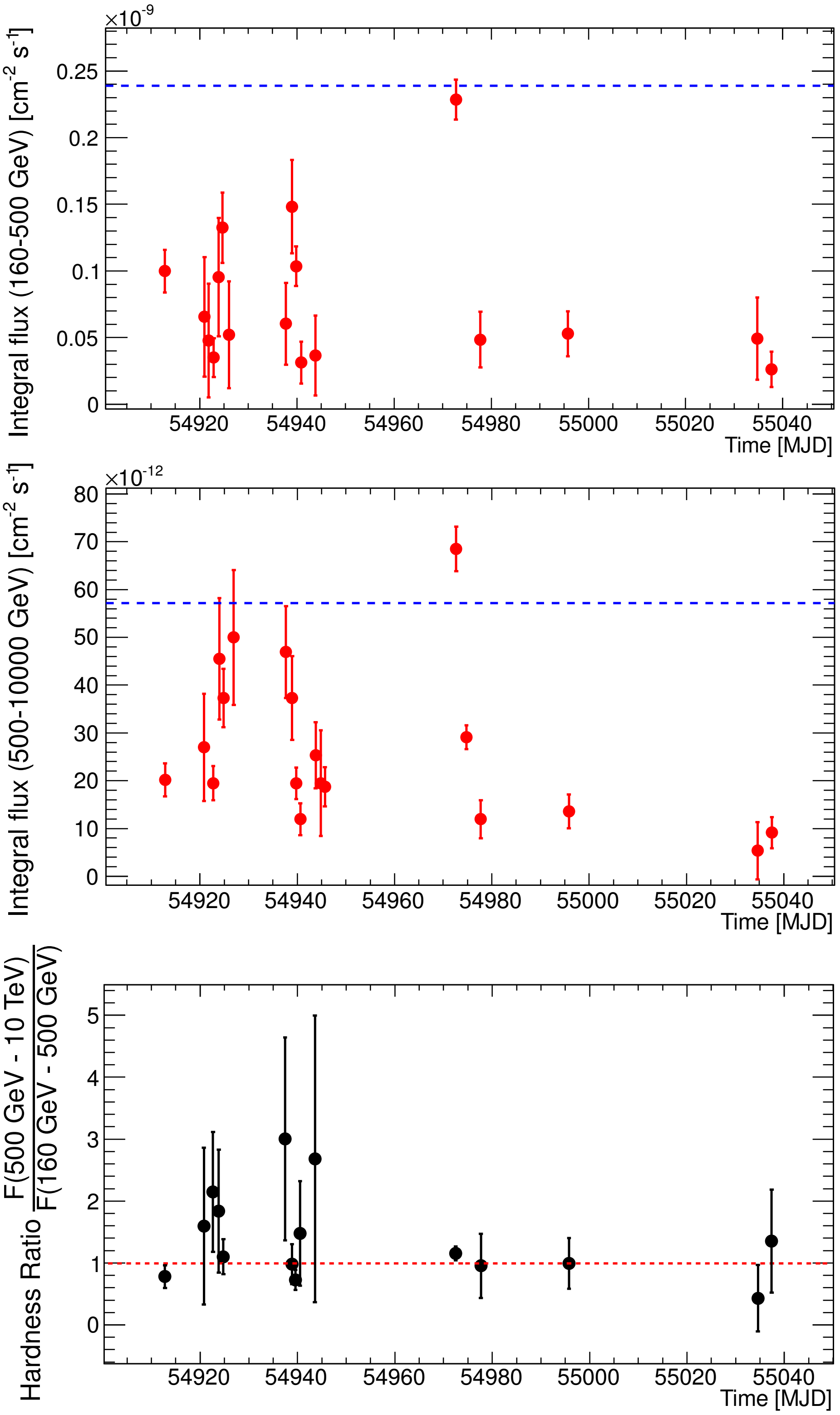

Figure 6.4: Light curves showing the integral flux at low energies (160 GeV to 500 GeV, top) and at high energies (500 GeV to 10 TeV, middle). The blue dashed line represents the Crab Nebula flux in the respective energy range. In the lower panel, the hardness ratio between the flux in these two energy bands, after normalization to the mean flux, versus time is shown. The red dashed line indicates the constant fit to the distribution.

6.2.5 Spectral analysis

Following the standard procedure for spectral reconstruction with MARS as explained in section 3.3, cuts have been optimized on the test data sample of the Crab Nebula, in order to reproduce the spectrum.
The following cuts have been found to deliver reliable results:

- size > 150 phe,
- α cut efficiency: 0.7,
- hadroness cut efficiency: 0.8,

where the actual cut per bin in α and hadronness is determined during the run of *fluxlc* according to the chosen efficiency. Again, three off positions have been used to determine the background of the measurement.
With this configuration, *fluxlc* was applied to the whole data set, to data only from May 22 (when the source exhibited an increased flux) and to all data except May 22. The resulting histograms in *estimated energy* have been unfolded using the macro *combunfold*, applying all available unfolding methods, see also [A^{+}07b]. A good agreement has been found in all three cases and the spectra obtained with the method of Bertero [Ber89] are shown in Figure 6.5. The resulting parameters of a power-law fit to the spectra are shown in Table 6.4. During this fit, the correlation of the data points, which has been introduced in the course of the unfolding, is taken into account. Based on the calculated χ^2, the probability of the fit to describe the data points has been determined for the given 6 degrees of freedom. The simple power-law describes the flaring state very well with a fit probability of 93%. Also for the low and average state the fit probability is sufficiently high (21% and 26%, respectively). Based on the obtained fit parameters, the observation on May 22 is not only characterized by an increased flux, but also a hint for a hardening in the spectrum can be seen (spectral index -2.28 ± 0.06 versus -2.40 ± 0.05), albeit not being significant for a real claim on spectral hardening. While the average spectrum is strongly influenced by this particular observation, the low state of the source is more likely represented by the spectrum of all data except the flaring day.

Table 6.4: Properties of a fit of the obtained MAGIC spectra of Mrk 501 with the power-law function $\frac{dF}{dE} = f_0 \cdot \left(\frac{E}{r}\right)^{\alpha}$, with r=1 TeV. During the fit, the correlation of the data points (introduced during the unfolding) is taken into account. The fit probability is calculated for 6 degrees of freedom.

Data set	index α	$f_0\,[10^{-11}\,\mathrm{cm}^{-2}\mathrm{s}^{-1}\mathrm{TeV}^{-1}]$	χ^2	Fit Prob.
Average state (all data)	-2.34±0.04	1.20±0.05	7.62	26%
Low state (all except May 22)	-2.40±0.05	0.93±0.04	8.36	21%
Flaring state (May 22)	-2.28±0.06	3.08±0.20	1.94	93%

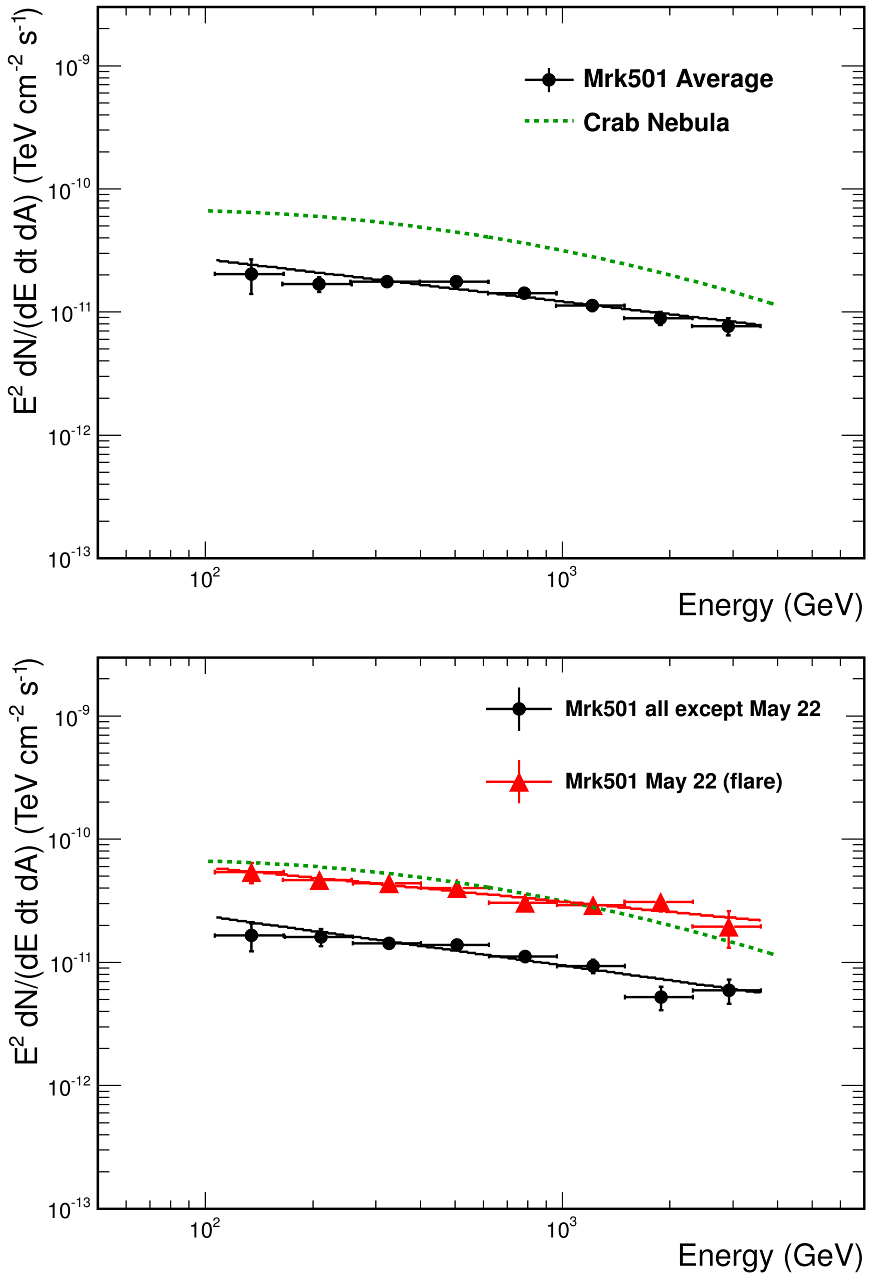

Figure 6.5: Spectral energy distributions of Mrk 501, obtained from the complete MAGIC data set (upper panel), from the flare night May 22nd (red triangle points in the lower panel) and from all nights except the flare night (black points, lower panel). The spectra have been fitted with a simple power law, while taking into account the correlation of the individual bins after unfolding. The according fits are shown in the figures as solid lines. The green dashed line indicates the spectrum of the Crab Nebula as published in [A$^+$08c].

6.3 Multi-instrument data set

The presented MWL campaign took place from March 15^{th} (Modified Julian Date (MJD) 54905) to August 1^{st} (MJD 55044) in 2009 and 30 instruments collected data in all frequency bands during this time. In the radio regime, several single dish telescopes around the globe were involved, as well as the mm-interferometer *Submillimeter Array* (SMA) and the *Very Long Baseline Array* (VLBA) interferometer. Due to its good angular resolution (≈ 0.1 pc at 43 GHz for the closest blazars [PPE10]), the VLBA measured the flux not only of the total source, but also from the core region of the jet. A range of telescopes observed in the optical frequency range, with a variety of filters. Many of the R-band measurements were conducted as part of the *GLAST-AGILE Support Program* by the *Whole Earth Blazar Telescope* (GASP-WEBT program). Data in the ultraviolet (UV) bands have been provided by the *Ultraviolet/Optical Telescope* (UVOT) onboard the *Swift* satellite. The satellite also conducted measurements in the X-ray band, with the *X-ray Telescope* (XRT) and the *Burst Alert Telescope* (BAT). Furthermore, the satellite *Rossi X-ray Timing Explorer* (*RXTE*) took X-ray data with the on board *Proportional Counter Array* (PCA) and the *All Sky Monitor* (ASM). The *Fermi* satellite has been observing the source in survey mode throughout the campaign, taking measurements with the LAT instrument. These short observations were part of a long-term monitoring of the source which involved also the two all-sky instruments BAT and ASM. In the VHE range, observations were carried out by MAGIC, VERITAS and the 10 m Whipple telescope.
For a list of all participating instruments, see Table B.1. For a detailed description of telescopes, observation strategies and analysis procedures, see [A+11b] and references therein.

6.4 Summary on average state results

In the scope of the first analysis of this MWL data set, as presented in [A+11b], a spectral energy distribution for the average state of the source throughout this campaign has been derived (see also Figure B.2). With the large number of participating instruments and the long duration of the campaign, which allowed to accumulate ample event statistics, also with the less sensitive instruments, a very good coverage of the entire SED could be reached. In the course of the work presented in [A+11b], the SED has been modeled following a simple one zone synchrotron self Compton (SSC) scenario (see subsection 5.2.2). In order to reproduce the entire SED, the energy spectrum of the underlying electron population has been characterized as a power-law distribution over an energy range γ_{min} to γ_{max} (with the energy given in terms of the particle Lorentz factor γ), with two spectral breaks at $\gamma_{br,1}$ and $\gamma_{br,2}$, respectively. The resulting parameters are given in Table 6.5. For the generated SED curve, see Figure B.3 (also included in Figures 6.17 and 6.18) and [A+11b]. In the latter reference, also more detailed descriptions on the choice of the modeling parameters and implications are given.

6.5 MWL flux variability

The distributions of flux versus time which were measured by the various instruments over the 4.5 month long campaign are shown in Figures 6.6 and 6.7. The former figure includes all instruments which allow to derive a flux point for each pointing of the instrument, while the latter comprises the light curves which were obtained with *Fermi*-LAT, *RXTE*-ASM and *Swift*-BAT and have been integrated over 30 days for each flux point due to low statistics.

In the radio regime, a nearly constant flux can be seen in the light curves from all instruments. The best sampled one is the light curve measured with the *Owens Valley Radio Observatory* (OVRO). Except for a period of ≈ 15 days (MJD 54940 to 54960), a constant emission can be noted.

The VLBA took additional measurements in the radio band, which were not part of the initial campaign and were added to the data set later on. Snapshots of the total flux and the flux from the core region were taken in December 2008 and January, February and May 2009 (see Figure 6.8). Compared to the previous months, both the total and especially the core flux show a significant increase in May 2009, although the uncertainties are relatively large.

The coverage in the infra-red band is rather sparse and the uncertainties of the measurement are large, still some variability has been seen by the different instruments. In the optical regime, an extensive sample of measurements is available, which shows a nearly constant flux from all participating telescopes. Only small variations can be seen in the Mitsume data (in all bands), for example around MJD 54935 and 55000. The very densely sampled light curve supplied within the GASP-WEBT program shows small flux variations in the order of 10% over time scales of about 15 days. Stronger variations of about 25% are apparent in measurements in all ultra-violet bands in time scales of 25 to 40 days.

In the X-ray band, the light curve obtained with *RXTE*-ASM (which required an integration time of 30 days for each flux point) shows only small variation in flux, while *Swift*-BAT saw a somewhat higher variability, but with large uncertainties. *Swift*-XRT saw strong variations in both energy bands (below and above 2 keV) on time scales of days and below. The XRT light curves exhibit flux variations of 50 to 60% on time scales of 10 to 20 days and they cover a large flux increase of more than 2 times the baseline flux in both bands around MJD 54977. The measurements taken by *RXTE*-PCA show only small variations, while a significantly increased flux was seen around MJD 54968 ad 54974.

The two *Fermi*-LAT light curves with integration times of 15 and 30 days, respectively, report on some variability, with an increased flux around MJD 54950. However, short term variations as in the X-ray band could not be probed.

Despite the naturally more sparse sampling in the VHE regime, the light curves obtained with the IACTs show that the source was quite active in this regime. Besides variations on time scales of several days, two large outbursts have been detected around MJD 54952 and 54973. While the former one was seen by VERITAS and Whipple, the latter was observed by MAGIC and Whipple.

In the following, the two periods of increased flux seen in VHE and X-ray data are investigated in more detail. Subsequently, a quantitative study of the overall variability is presented.

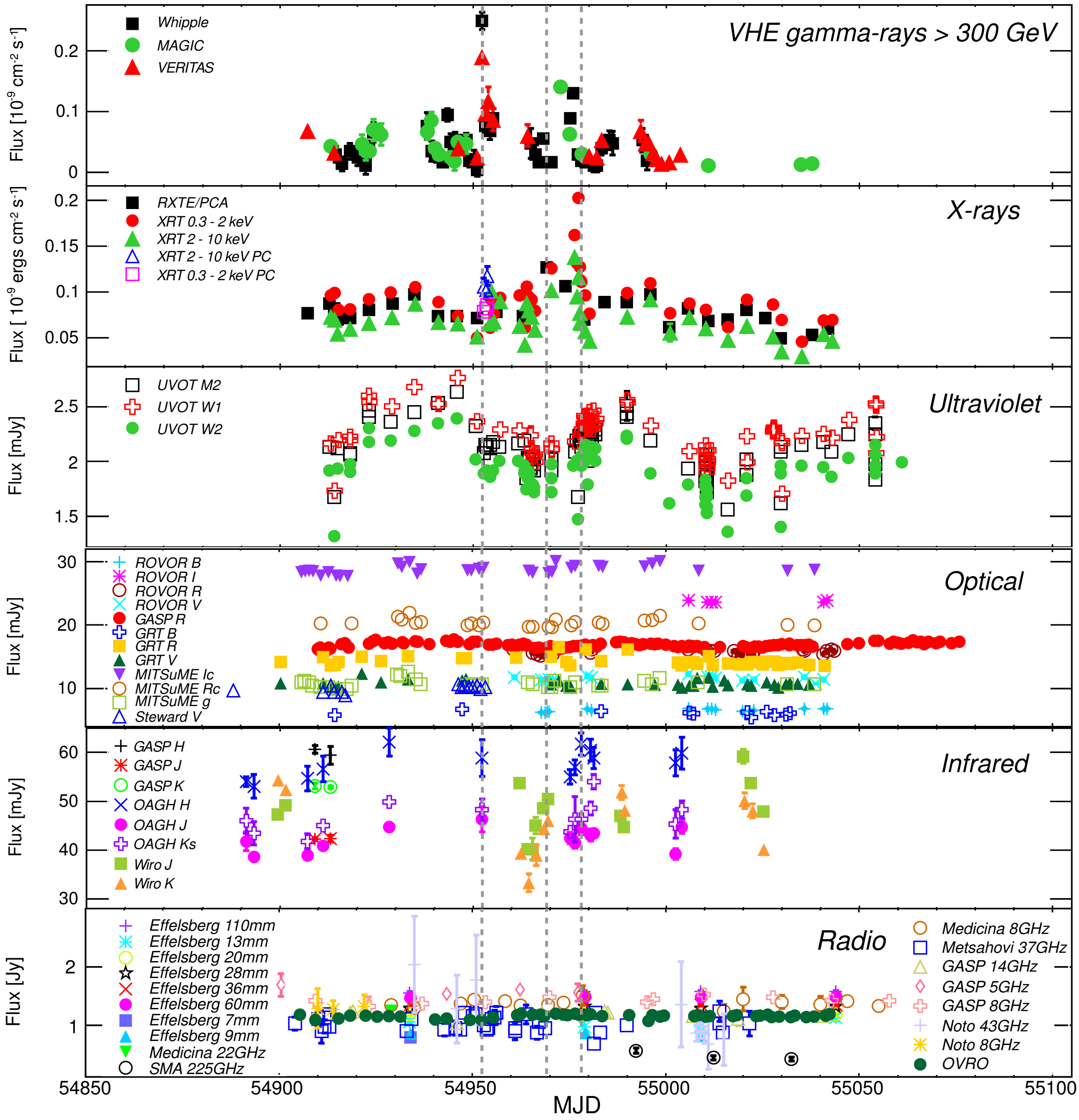

Figure 6.6: Light curves for all wavebands over the whole campaign, including all instruments which allowed to derive a flux point for each pointing. From top to bottom: VHE gamma-rays (MAGIC, VERITAS and Whipple 10m telescope), X-rays (*Swift*-XRT and *RXTE*-PCA), ultra-violet (*Swift*-UVOT), optical telescopes, infra-red and radio measurements. The dashed vertical lines indicate a sharp VHE flare at MJD 54952 and a period of increased activity in the VHE and X-ray range from MJD 54969 to MJD 54978.

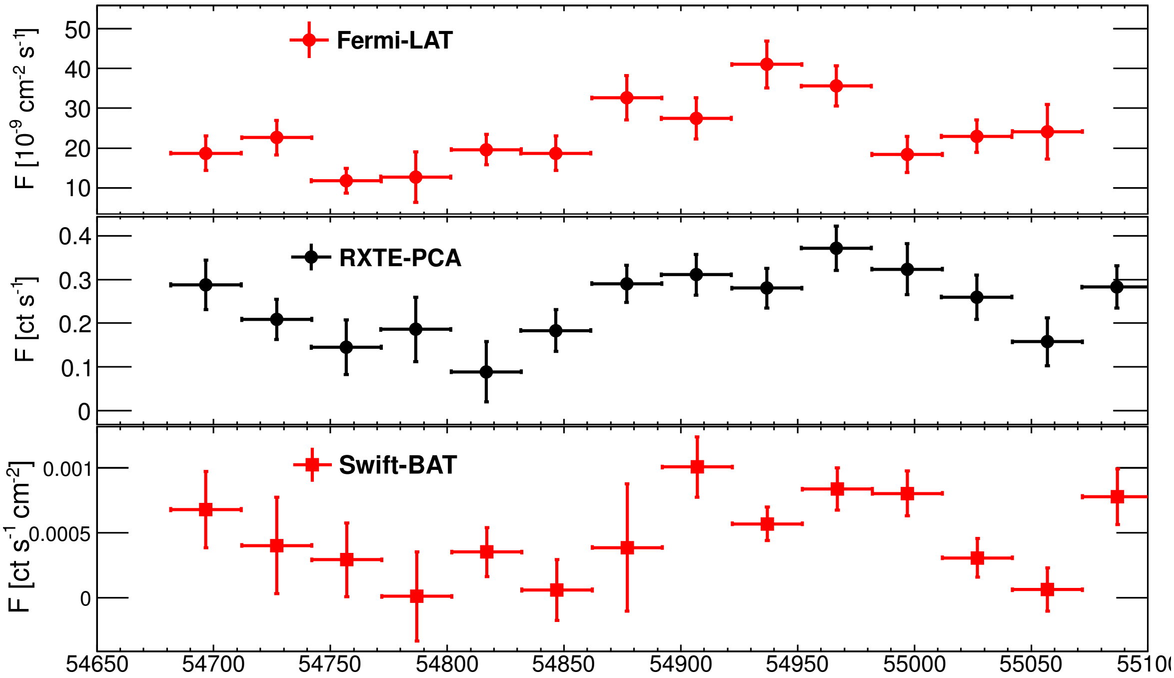

Figure 6.7: Light curves for the participating instruments, which required an integration time of 30 days. From top to bottom: *Fermi*-LAT, *RXTE*-ASM, *Swift*-BAT.

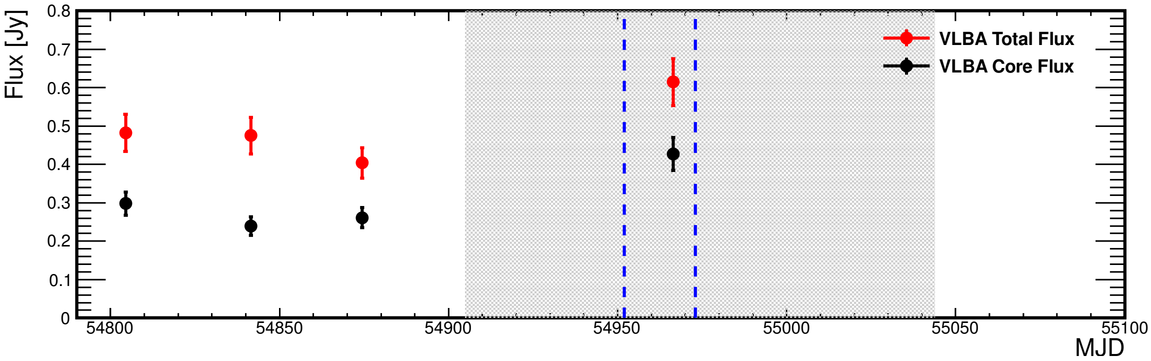

Figure 6.8: Radio light curve obtained with the VLBA at (43 GHz) around the time of the MWL campaign. Shown is the total radio flux and the flux stemming from the core region of the jet. The shaded area indicates the duration of the MWL campaign, while the dashed vertical lines define the times of the VHE flaring events.

6.5.1 Outbursts in the X-ray and VHE band

During the presented MWL campaign, Mrk 501 showed two periods of flux increase in VHE gamma-rays. Figure 6.9 shows the obtained light curves, zoomed in around the period of high activity. Beside the VHE measurements (MAGIC, VERITAS, Whipple; upper panel) also the (short term integrated) X-ray light curves are shown (*Swift*-XRT and *RXTE*-PCA, second from top). Additionally, measurements of the polarized optical emission have been carried out around the time of the first VHE outburst by the *Steward Observatory* and were added to the data set obtained in the scope of this campaign. The degree of optical polarization and the corresponding electric field vector position angle (EVPA) are shown in the lower two panels of Figure 6.9. Unfortunately, no polarization data are available around the time of the second flare. Because the *Fermi*-LAT light curve does not allow to study short time variations and due to the nearly steady emission from radio to optical (see section 6.5), the other wavebands are not considered here.

1st VHE Flare (MJD 54952)

On May 1st 2009, Whipple observed Mrk 501 in the time from MJD 54952.35 to 54952.47 at a flux level of 2 Crab Units (C.U.), which corresponds to about 10 times the baseline flux. This observation caught the rising flank of the flare and measured a flux increase by a factor 5 in 25 minutes, which indicates very fast variability. VERITAS was alerted due to this observation and observed, together with Whipple, an increased flux of 6 times the baseline flux for the rest of the night. The source stayed at a level of enhanced activity in the subsequent nights. The VHE gamma-ray measurements of this flare have been presented in [Pic11], where also more details can be found.

No simultaneous observations took place with the X-ray instruments, but *Swift*-XRT measurements, which were conducted 7 hours later, show only a slight increase in flux, while this increase appears to be stronger at high energies ($2 - 10\,\mathrm{keV}$). The measurements of the optical polarization show a state of enhanced polarization degree prior to the flare, while a drop by about 15% occurs right at the time of the flare in VHE. The EVPA shows a rotation by 15 degrees prior to the flare and stops when the flare occurs.

2nd VHE Flare (MJD 54973)

In the time span from MJD 54973 to 54976, a second flux increase has been seen in the TeV range. MAGIC observations took place on MJD 54973 (May 22nd) and saw a flux close to four times the baseline flux within 1.7 hours exposure. The next pointing took place on May 24th (MJD 54975.00 to 54975.12), when the flux was down to 1.7 times the baseline again. Whipple started observations of Mrk 501 later on that date (MJD 54975.25) and measured a flux of 2.5 times the baseline. On MJD 54976.23 (May 25th), another flux increase of almost 4 times the quiescent flux has been measured by Whipple. VERITAS did not observe the source in this time.

As seen in Figure 6.3, no intra-night variability was seen with MAGIC for the night of the flare, while no intra-night light curves were available from the Whipple observations.

In the X-ray regime, again no simultaneous measurements took place at the time of the VHE gamma-ray observations. *RXTE* took measurements every 5 days and pointed at

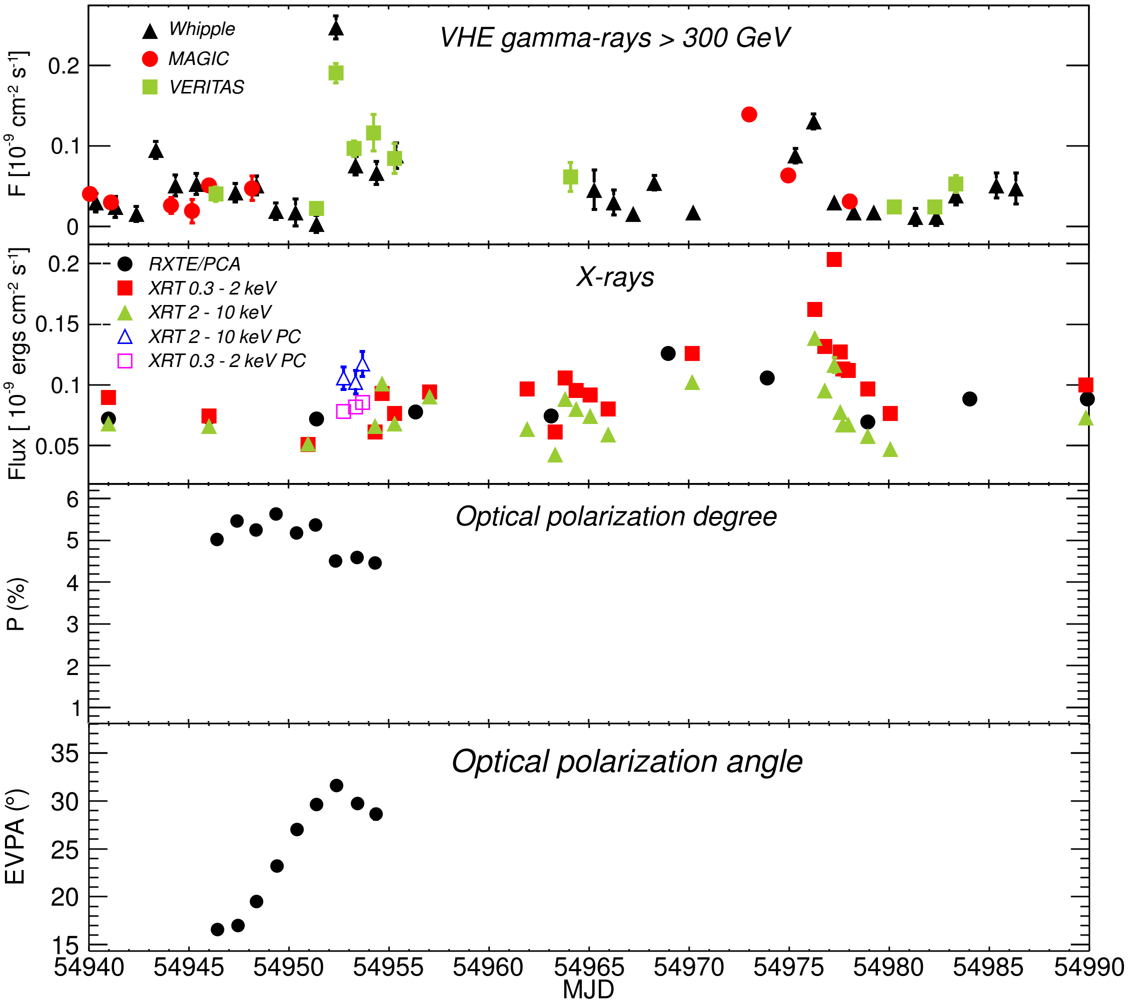

Figure 6.9: MWL light curves which have been zoomed in around the periods of the flares seen in the VHE range. Top to bottom: VHE gamma-rays, *Swift*-XRT and *RXTE*-PCA, degree of optical polarization, electric field vector position angle (EVPA) (both from Steward Observatory). The Whipple fluxes have been provided as scaled to report a flux >300 GeV, while the actual energy threshold of the experiment is 400 GeV.

the source on MJD 65969 and 54974, which is 4 days before and one day after the MAGIC observations. These days showed an increase in flux by 1.7 and 1.4 times the baseline, which was reached again on MJD 54979. *Swift*-XRT did not observe the source between MJD 54970 and 54976, but the measurement on MJD 54970 showed a trend of increasing flux (factor of 1.5 with respect to the baseline), which was continued on MJD 54976.3 (just above a factor 2) and, after a slight decline on MJD 54976.9, reached its maximum on MJD 54977.3 with a flux of roughly 2.5 times the baseline flux. The observation on MJD 54976.3 can be considered as quasi-simultaneous to Whipple, while the largest increase took place exactly one day after the outburst seen by Whipple. At that time, the gamma-ray flux was seen to be down to the baseline flux again. The X-ray baseline flux is reached, after a monotone decline, 2-3 days later.

It can be said that both the VHE gamma-ray and the X-ray measurements report on a state of enhanced activity in the sources in the period from MJD 54973 to 54976, while an erratic rise and fall of the flux levels on time scales of the order of days is seen.

6.5.2 Variability analysis

To address the variability seen in the different light curves in a quantitative way, the fractional variability has been determined for each instrument, following [V+03]. It is defined as

$$F_{var} = \sqrt{\frac{S^2 - \langle \sigma^2 \rangle}{\langle F \rangle^2}}, \tag{6.1}$$

given by the variance S^2 of the light curve, corrected for the contribution from the measurement uncertainties σ and normalized with the mean flux $\langle F \rangle$. The results are summarized in Figure 6.10, which shows the obtained values of variability versus the (mean) frequency of the instrument.

In the frequency range from radio to optical, no significant variability was seen. The fractional variability reaches from $F_{var} = 0.01$ for ROVOR to $F_{var} = 0.20$ for GRT. The X-ray instruments show some variation in the flux, characterized by $F_{var} \approx 0.3$. The variability determined with the *Fermi*-LAT is of the same order, while it has to be stated that the F_{var} values obtained for the LAT, as well as BAT and ASM are not directly comparable to the remaining values, due to the difference in the probed time scales. In the VHE gamma-ray regime, the fractional variability is shown for the complete light curves (filled markers) and for light curves after removal of the flare observations (open markers). Obviously the measurements which include the flares show the largest variability, up to $F_{var} \geq 0.6$ and even 0.9 for Whipple, but also the flare-corrected light curves show a stronger variability than the other bands ($F_{var} \geq 0.4$).

It can be concluded that Mrk 501 showed a clear increase in variability with increasing frequency during the presented MWL campaign, which ranges from mostly steady emission in radio to optical frequencies up to fast variability, partly on time scales down to minutes, at the highest energies.

6.5.3 MWL correlations

Based on the various light curves obtained during this campaign, a study for cross-correlations between the different wavebands has been performed. For this purpose, the *Discrete Correlation Function* (DCF) has been determined for each pair of instruments, following [EK88]. The DCF allows to search for correlated flux changes in a pair of light curves, probing a range of possible time lags. The tools used for this study have been prepared by N. Nowak.

A range of -100 to 100 days has been probed, although due to the limitation of the given data set to 4.5 months, correlations at time lags of more than 70 days should be treated with care. Because of the difference in exposure times and the uneven sampling, the test

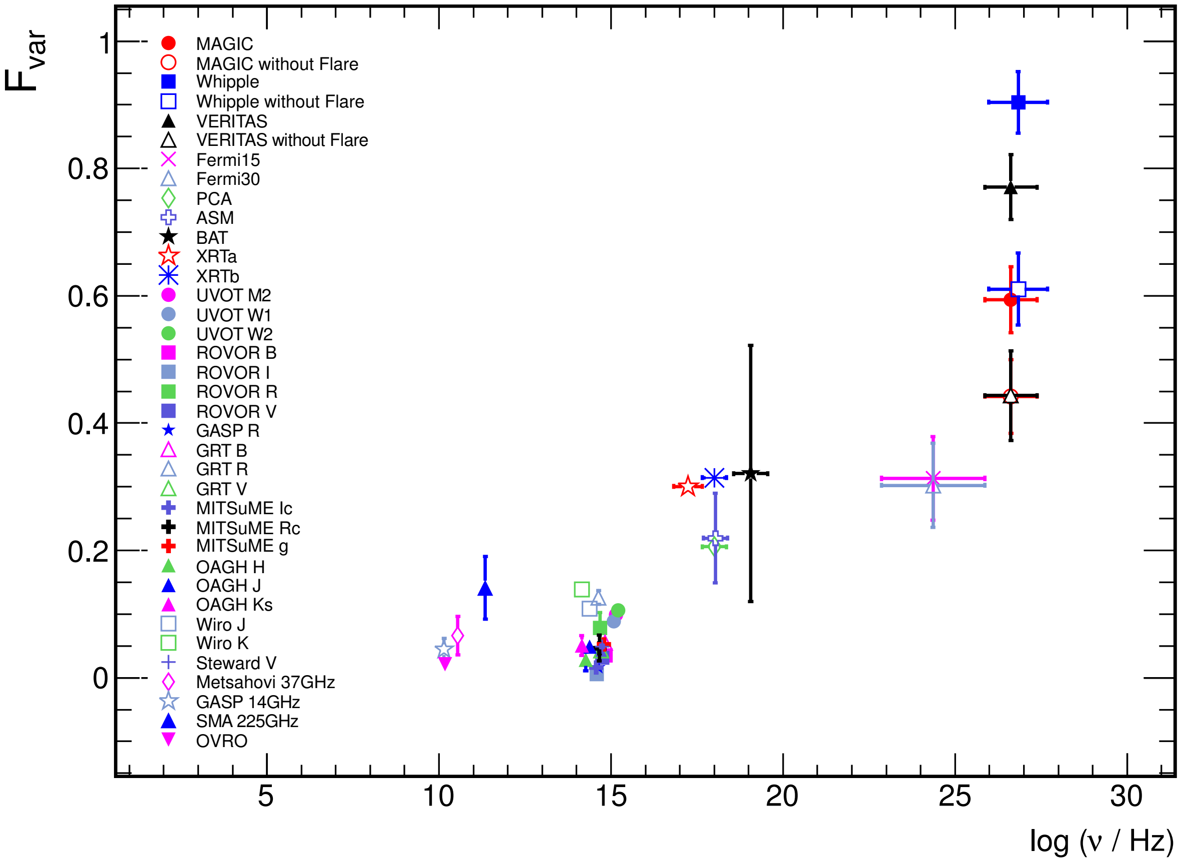

Figure 6.10: Fractional variability F_{var} for each instrument, calculated following [V^+03], based on the light curves obtained over the entire campaign. For the VHE gamma-ray instruments, a second F_{var} has been obtained for light curves from which the flare observations have been excluded.

for the significance of peaks in the DCF distribution is not trivial. For this purpose, light curves have been simulated for each instrument, regarding the sampling rate and the individual exposure time. The *power spectral density* (PSD) of the simulations has been modeled as a simple power-law with indices ranging from -2.9 to -1.0 in steps of 0.1. For each instrument, 1000 light curves per PSD have been simulated, following the prescription given in [UMP02] and using the method from [TK95]. Subsequently, the simulations have been tested to follow the same PSD as the measured light curve with the *psresp* method [UMP02]. The sample of simulations with the best matching PSD is applied for the correlation studies. The DCF itself is determined for a given combination of instruments, while the significance is tested by correlating the real light curve of one instrument to the 1000 simulated curves generated for the other. Based on the simulations, confidence bands of 95% and 99% are determined.

At first, the method has been used to investigate the *Discrete Auto Correlation Func-*

tion (DACF) for each instrument, which provides on the one hand a sanity check for the method itself and on the other hand allows to look for characteristic time scales which could point to an underlying periodicity. No remarkable result has been found here.
Combinations of instruments of all wavebands have been investigated for cross-correlations. The low level of activity in radio and optical already indicates that no significant correlation in flux changes are found neither among these bands nor with instruments of other bands. The corresponding DCF plots are shown in Appendix B. The MeV-GeV range cannot be probed for correlations on time scales of days based on the *Fermi*-LAT light curves. The same is true for BAT and ASM measurements.
The determined DCF for the remaining X-ray and VHE instruments are shown in Figure 6.11. For this study, the light curve of all three VHE gamma-ray instruments (above 300 GeV) were combined to a single light curve, containing all the observations. A second light curve has been prepared by removal of the flaring days (MAGIC: MJD 54973.1; VERITAS: MJD 54952.4; Whipple: MJD 54952.4, 54975.4 and 54976.3). In the X-ray regime, the light curves obtained by *Swift*-XRT (in both energy ranges) and *RXTE*-PCA have been used. Also here, flare-corrected light curves have been obtained for *Swift*, where the removed observations are MJD 54977.3 and 54976.3.
In Figure 6.11, the DCF are presented for the combination of one X-ray measurement (top to bottom: *RXTE*-PCA, *Swift*-XRT (0.3 - 2 keV) and *Swift*-XRT (2 - 10 keV)) with the VHE light curve. On the left hand side, DCF for the complete light curves are shown, while on the right hand side, the results of the study on the flare-corrected measurements are presented. For the complete light curves, a significant correlation has been found among the *Swift*-XRT measurements in both bands and the VHE light curve, at a time lag of -20 days. Also a marginal correlation is seen for PCA. This is not very surprising, as the first, larger outburst at gamma-ray energies occurred roughly 20 days before the flare seen by *Swift* (and the smaller flux increase measured with PCA). After removal of the flares, no significant correlation is found.

6.6 MWL spectral variability

Besides the study of variability in terms of the emitted flux at different wavelengths, also the investigation of changes in the overall energy spectrum of Mrk 501 have been a major part of this work. Additional to the broad-band SED which was averaged over the entire campaign and presented in [A+11b], energy spectra derived from single observations or integrated over shorter time scales have been provided by some of the participating instruments. For the X-ray instruments XRT and PCA, spectra were obtained for each pointing of the instrument, while for the *Fermi*-LAT, one spectrum per 30 day integration was generated, wich were likewise presented in [A+11b]. For the VHE instruments VERITAS and MAGIC, dedicated spectra have been produced from the observations which covered the increased flux states of the source. For Whipple, two dedicated spectra for the flare on MJD 54952 were produced (and presented in [Pic11]). In this section, the spectral variability in the X-ray and VHE gamma-ray band is investigated, paying particular attention to the flaring episodes. Subsequently, changes in the entire SED around the two flares will be examined.

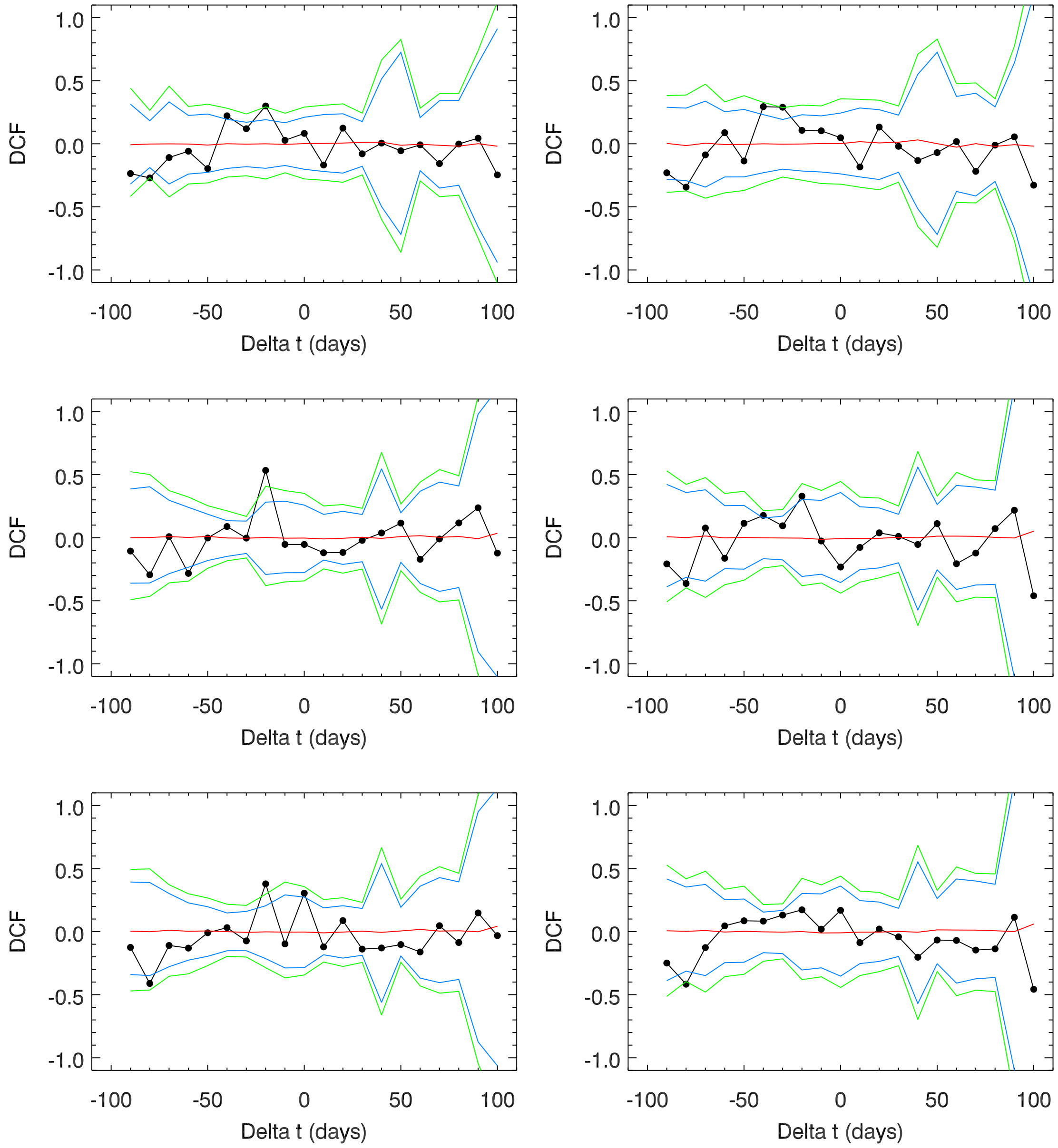

Figure 6.11: Discrete Correlation Function between the VHE and X-ray instruments versus possible time lags, following [EK88]. From top to bottom, the combined light curve of all VHE instruments has been tested for correlation with the light curves obtained with *RXTE*-PCA, *Swift*-XRT (in the band 0.3 - 2 keV) and *Swift*-XRT (2 - 10 keV). On the left hand side, the complete light curves have been used, while on the right hand side, the results for light curves after removal of the flare(s) are shown. The black dots report the calculated DCF based on the data, while the blue (green) lines define the 95% (99%) confidence intervals as derived based on MC simulations. For details see text.

6.6.1 VHE gamma-rays

The different spectra which are obtained for the VHE gamma-ray range are presented in Figure 6.12.

A spectrum which represents the low state of the source has been derived for all three participating IACTs, based on all data taken during this campaign, except for the observations which showed an outstanding increase in flux. For VERITAS, observations between MJD 54952 and 54955 have been removed from the data set to obtain this spectrum, while a high state spectrum was produced based on the excluded data. The two spectra were already presented in [A^+11b]. The same procedure has been performed for the Whipple observations, while based on the observations in the mentioned time frame, two different spectra have been derived for this instrument: one covering the rise and peak of the flare (MJD 54952.35 - 54952.41, marked as “Whipple very high”) and one derived from the remaining observations when the source was still showing a high flux (MJD 54952.41 - 54955, marked as “Whipple high”). For more details on these observations see [Pic11]. Based on the MAGIC observations, an average spectrum was presented in [A^+11b], which represents the low state of the source as the initial data set did not contain the observation from May 22^{nd}, the day of the flare seen by MAGIC. For the spectra shown in Figure 6.12, the low state and flare spectrum derived in the course of the re-analysis performed in this work has been chosen, as presented in section 6.2. All spectra have been corrected for attenuation of the gamma-ray flux by interaction with photons of the EBL, using the model by Franceschini et al. [FRV08].

A good agreement can be noted for the low state spectra measured by the different experiments. Regarding the high state spectra, a tentative “harder when brighter” behavior is seen.

6.6.2 X-rays

The X-ray satellite instruments *Swift*-XRT and *RXTE*-PCA allowed to derive a spectrum per pointing of the instrument. The spectra which were recorded closest in time to the two outbursts in VHE gamma-rays are summarized in Figure 6.14 for XRT and Figure 6.15 for PCA spectra, around the first (top panels) and second (bottom panels) VHE flare. For the first flare, not much variation is seen in the PCA spectra, while significant spectral and flux variability is present in the XRT measurements. Here, a tendency for an upward curvature towards increasing energy is seen in the spectra closest to the VHE flare. To study the evolution of the spectral shape further, a spectral analysis with a simple power-law model was performed for the *Swift* spectra by M. Perri. The evolution of the corresponding spectral index with time is presented in Figure 6.13. The distribution shows a clear peak around the time of the flux increase in the VHE band (MJD 54952-54953), which confirms a significant spectral hardening in this time.

In the case of the second VHE flare, variability is seen for both X-ray instruments, but no such spectral hardening is found. The spectra derived from the PCA data indicate a flux variation of a factor of about 2.3, but the spectral shape is unchanged. A substantial change in flux and shape on a time scale of less than one day was seen by *Swift* on MJD 54977, where the flux at energies below 2 keV changed by about 50-60% within less than 7 hours.

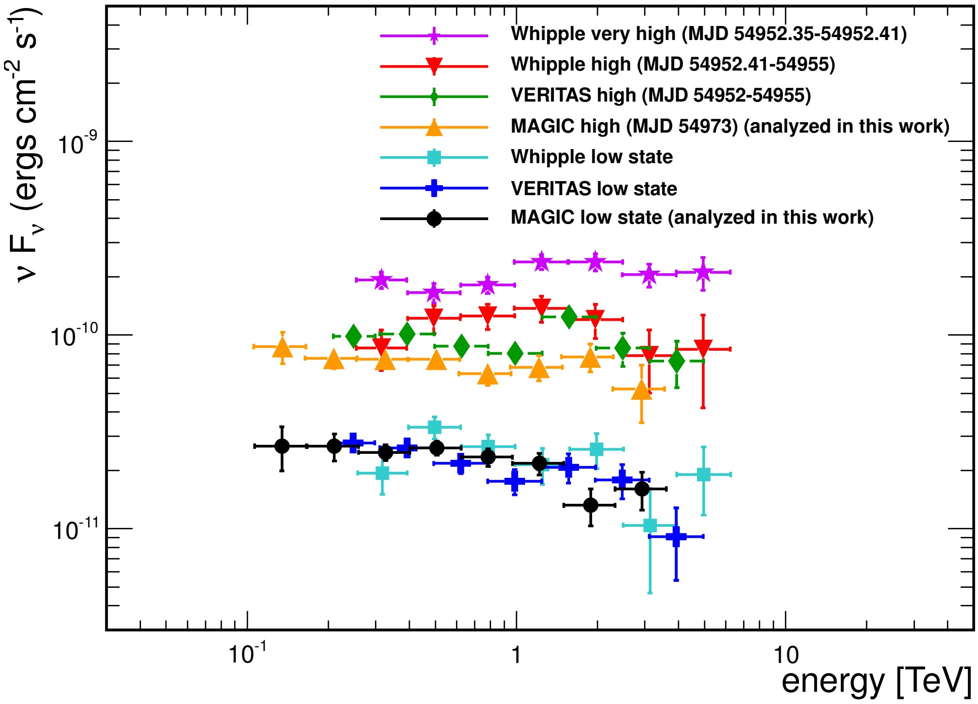

Figure 6.12: Spectral energy distributions measured by MAGIC, VERITAS and Whipple during the low state of the source and two states of increased VHE flux. The spectra have been corrected for EBL absorption using the model by Franceschini et al. [FRV08]. The VERITAS and Whipple spectra have been reported previously in [Pic11].

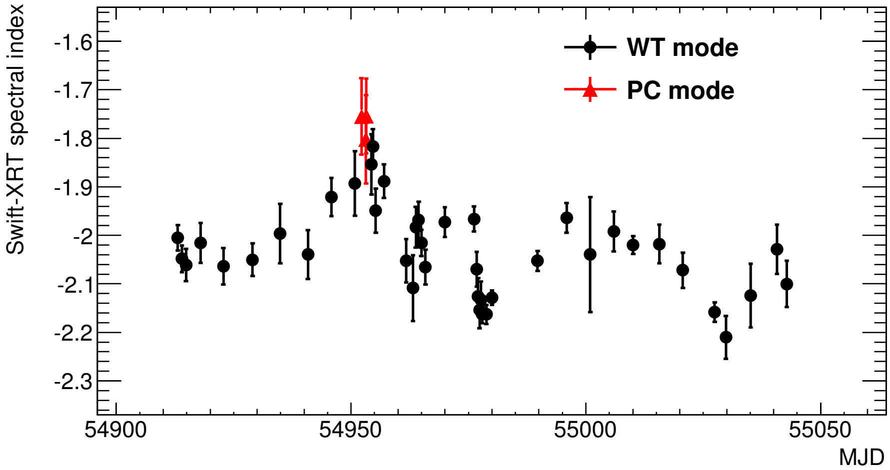

Figure 6.13: Based on a simple power-law fit which has been performed for each spectrum derived (per pointing) with *Swift*-XRT, the obtained spectral index is shown versus time. The red triangle points indicate observations which have been performed in *photon counting* (PC) mode, while most observations were carried out in *window timing* (WT) mode.

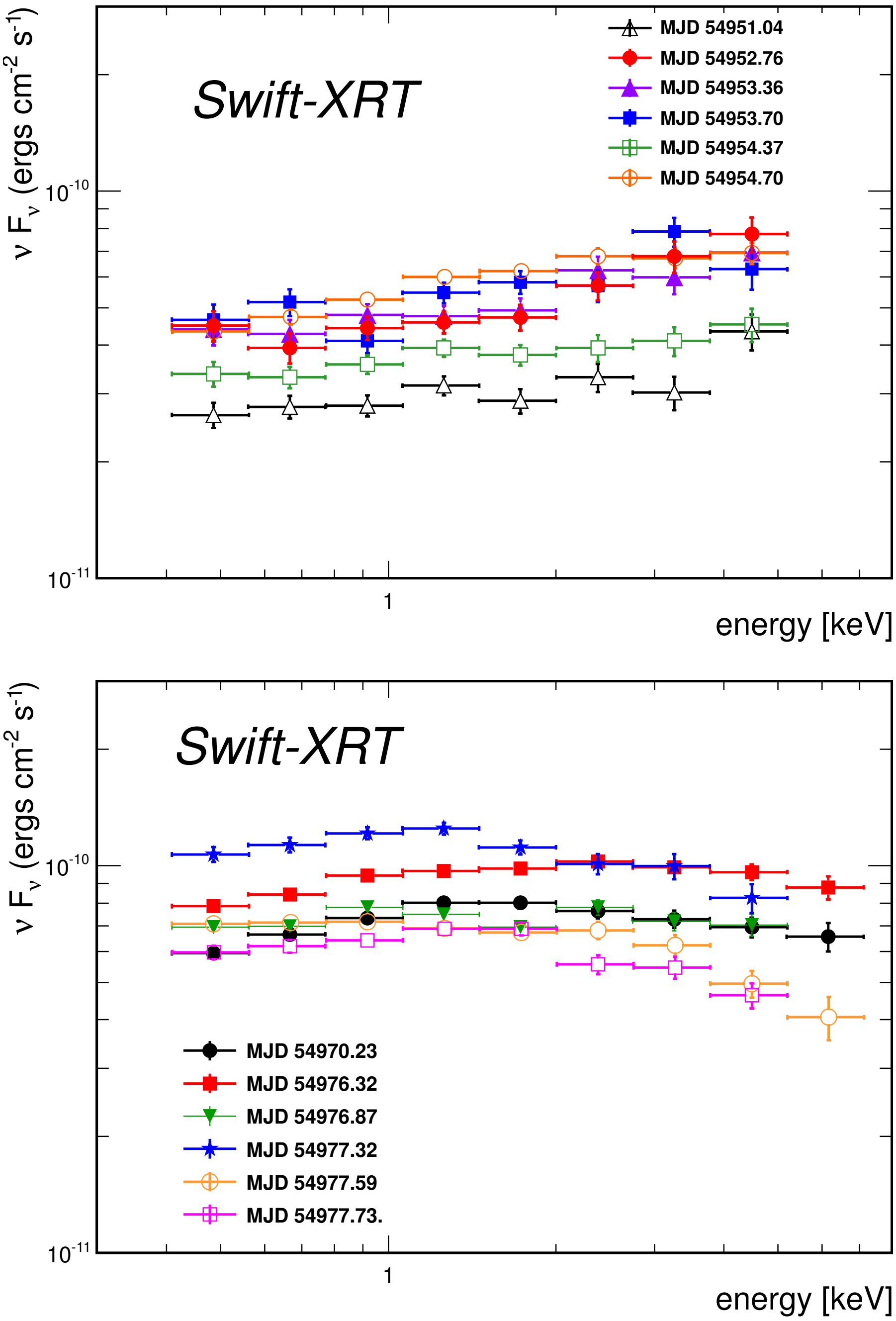

Figure 6.14: Spectral distributions in the X-ray regime, which have been derived from single pointings of *Swift*-XRT. In the upper panel, spectra which were taken around the time of the first flare are shown, while the lower panel comprises spectra around the time of the second flare.

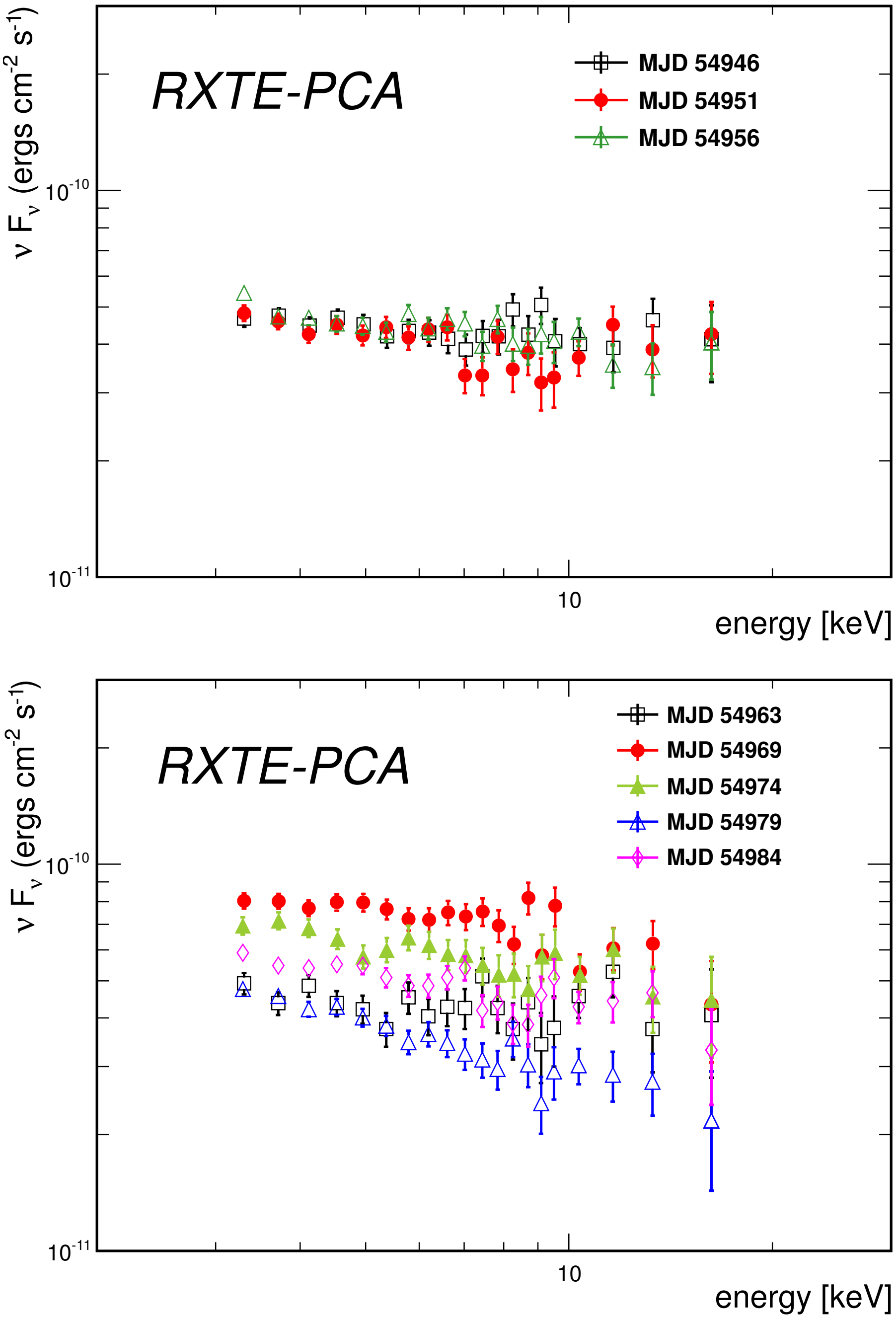

Figure 6.15: X-ray spectra measured by *RXTE*-PCA, which have been derived from single pointings. Spectra around the time of the first flare are shown in the upper panel, while the lower panel presents spectra which were measured around the time of the second flare.

6.6.3 Evolution of SEDs

Based on the SSC model which has already been applied to explain the average emission of the source, the X-ray emission from Mrk 501 is expected to constitute of synchrotron photons emitted by relativistic electrons. The bump in the spectrum which is formed by this emission is thus commonly referred to as *synchrotron bump*. The second bump, which is created by the emission in gamma-rays (MeV-TeV energies) is referred to as the *inverse Compton* (IC) *bump* in the the context of SSC scenarios.
In the following, the spectral variability seen in the X-ray and the VHE band around the flaring events is investigated in context of the entire spectral energy distribution.
The upper panel of Figure 6.16 shows an SED snapshot around the time of the first flaring event in VHE, at MJD 54953. Spectra measured by *Swift*-XRT and *RXTE*-PCA around that time are included. In the gamma-ray band, the dedicated *Fermi*-LAT spectrum derived from data from MJD 54952 to 54982 is shown. At the high energy end of the spectrum, the flaring spectra which were measured by Whipple and VERITAS are depicted. For the remaining instruments from radio to optical, one point per filter and instrument has been derived on the basis of the closest point in the light curve, if an observation has taken place within 5 days before or after.
It is apparent that, while the second bump moves up by a factor 3-6 compared to the average SED, the synchrotron peak remains rather stable in flux. However, the aforementioned change in shape of the synchrotron bump is obvious when regarding the *Swift*-XRT spectra. The shown spectrum from *RXTE*-PCA has not been measured simultaneously (not even contemporaneous). The upward curvature of the *Swift* spectrum thus indicates a shift of the synchrotron peak to higher energies, while only the rising flank has been covered by measurements.

Figure B.9 in Appendix B shows additional SED snapshots around the time of the flare, namely from MJD 54946, 54953, 54954 and 54956, which corresponds to 6 days before the flare, just after the peak of the flare, one day later when the source is still active in gamma-rays and two days later, when no VHE observations took place anymore. For any given date, the *Swift*-XRT and *RXTE*-PCA spectra which were measured closest in time are shown, with a maximum distance of 5 days. Regarding the *Fermi*-LAT spectrum, the high state spectrum (MJD 54952 to 54982) is included for dates within that range, otherwise the average spectrum gained by exclusion of this period is shown, see also [A^{+}11b]. In the VHE gamma-ray range, the respective flaring spectra are shown for the time interval of the flare and one day before or after, otherwise the low state spectra are included. Also here, close-by light curve points have been converted to spectral points for the remaining instruments.
In this sequence of figures, the observation that the synchrotron peak remains stable in height, but is subject to spectral changes becomes even clearer.

In the lower panel of Figure 6.16, the high state SED for the second observed VHE flux increase is shown. Included are again the closest *Swift*-XRT and *RXTE*-PCA spectrum, as well as the *Fermi*-LAT high state spectrum and the MAGIC flare spectrum. The second SED bump is seen to be shifted upward by a factor of ≈ 2.5, while this time also the synchrotron peak changes in flux, by approximately a factor $1.5 - 2$.

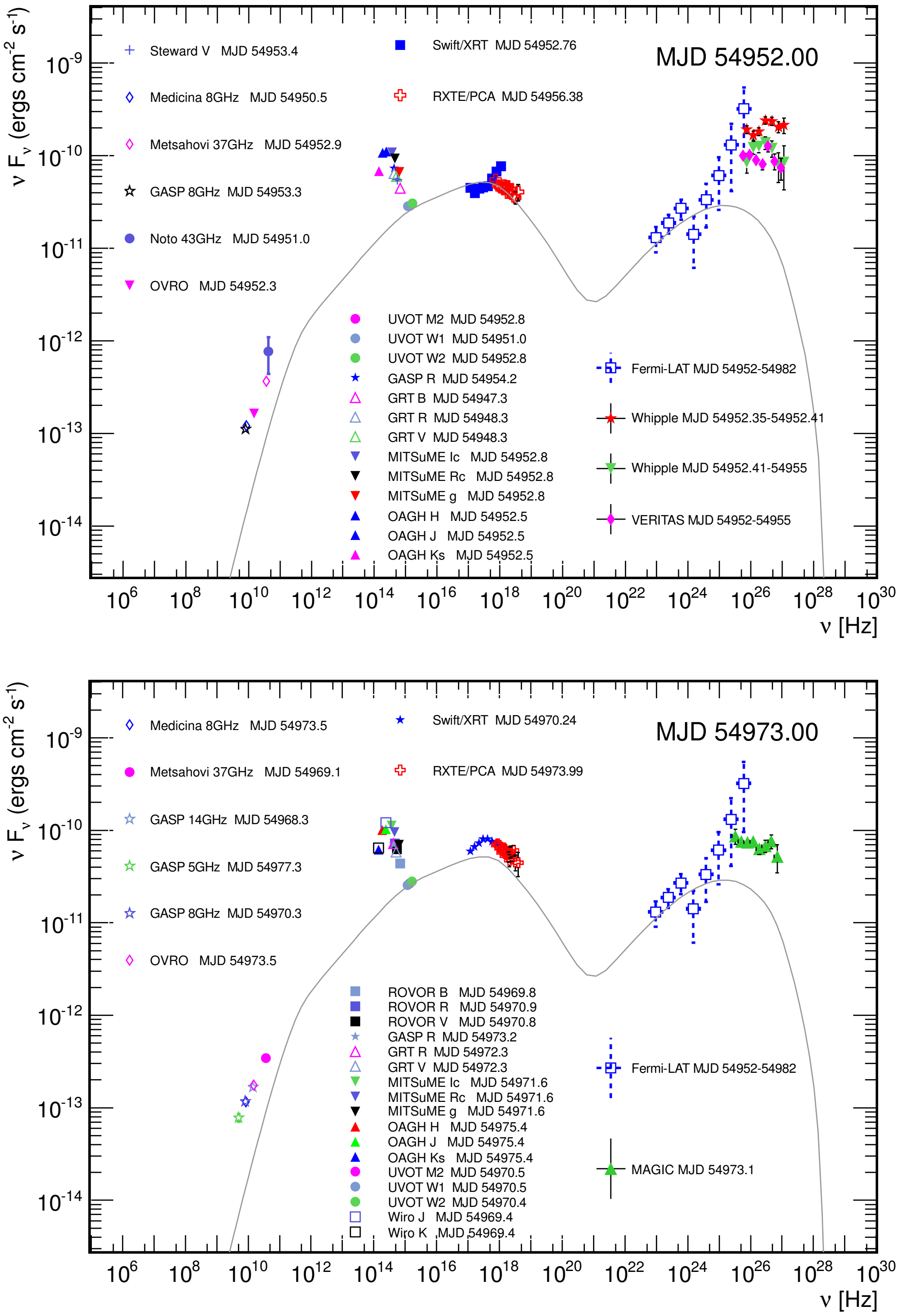

Figure 6.16: Spectral energy distribution, including individual instruments' spectra which have been obtained around the time of the first (MJD 54952, upper panel) and second (MJD 54973, lower panel) flare. Contemporaneous spectra with a temporal distance up to 5 days are included. For radio and optical instruments, a spectral point per instrument has been obtained, based on the closest measured flux point. The gray solid line represents the average state SSC model as derived in [A$^+$11b], for a better comparison of the spectra.

The slight mismatch of the *Fermi* and MAGIC spectrum can be explained by the corresponding integration times, which are very different for the various instruments. The LAT data are integrated over a time span of 30 days, among which there are larger periods of no observation in the VHE range due to moon and down times of the experiments. Within this time, the IACTs might have missed more active periods of Mrk 501, which in turn have been covered by *Fermi*.

In Appendix B, again a sequence of SEDs around the time of the flare is shown (Figure B.10), which reports on a more complex situation: Together with the overview of the X-ray spectra which was shown before (Figure 6.14, Figure 6.15), this sequence reveals a seemingly chaotic behavior of the source over time scales of days and below. While the synchrotron flux is moving up and down by 50% within one day, also the flux at VHE energies seen by MAGIC/Whipple is showing erratic flaring (see also Figure 6.9).

6.7 Modeling

Based on the modeling of the average state SED as presented in [A$^+$11b], the high state SEDs obtained in the course of this work have been modeled in the scope of the SSC emission processes, using the code implemented by H. Takami [Tak11]. Two different simple leptonic scenarios have been investigated to describe the SEDs:

First, an emission region similar to the one regarded in the low state analysis is assumed to be responsible for the entire emission during the two high states, as described in a one-zone SSC model (see upper panels in Figures 6.17 and 6.18). For this model, the size of the region and the Doppler factor have been fixed, while the magnetic field had to be reduced. For the first flare, where fast variability has been detected in the VHE range, an additional model configuration has been applied, where a smaller emission region and a larger Doppler factor have been assumed (lower panel in Figure 6.17).

Following another scenario, the high state emission has been assumed to stem from a second, spatially separated region, which emits radiation in addition to the steady low state emission, resulting in a two-zone SSC model. This scenario has been tried for the first outburst, but did not allow to describe the obtained SED. The substantial shift of the synchrotron peak to higher energies and the steep rise in the *Swift* spectrum requires a narrow electron SED centered at high energies, which does not produce any low energy synchrotron radiation. Accordingly, the electrons scatter mostly in the Klein-Nishina regime (see subsection 2.2.3), which results in a strong suppression of inverse Compton scattering and thus does not produce the high energy emission which is seen by VERITAS and Whipple. For the second flare, however, this scenario can well describe the seen change in the synchrotron and high energy bump, including also the optical and UV points (see lower panel in Figure 6.18).

The corresponding parameters used in the models (see also subsection 5.2.2) are shown in Table 6.5. As the definition of the number density used for the modeling in [A$^+$11b] is different from the one used here, Table 6.5 shows the density according to the model used in this work, for reasons of comparability, where the density n_e is defined according to

$$\frac{dN}{d\gamma} = \begin{cases} n_e \cdot \gamma^{-\alpha_1}, & (\gamma_{\mathrm{min}} < \gamma < \gamma_{\mathrm{br},1}) \\ n_e \cdot \gamma_{\mathrm{br},1}^{\alpha_2-\alpha_1} \cdot \gamma^{-\alpha_2}, & (\gamma_{\mathrm{br},1} < \gamma < \gamma_{\mathrm{br},2}) \\ n_e \cdot \gamma_{\mathrm{br},1}^{\alpha_2-\alpha_1} \cdot \gamma_{\mathrm{br},2}^{\alpha_3-\alpha_2} \cdot e^{\left(\frac{\gamma_{\mathrm{br},2}}{\gamma_{\mathrm{max}}}\right)} \cdot \gamma^{-\alpha_3} \cdot e^{\left(-\frac{\gamma}{\gamma_{\mathrm{max}}}\right)}, & (\gamma_{\mathrm{br},2} < \gamma), \end{cases} \tag{6.2}$$

with the electron Lorentz factor γ (see Equation 2.1), the spectral indices α_1, α_2 and α_3, the minimum and maximum energies (Lorentz factors) γ_{min} and γ_{max} and the break energies $\gamma_{\mathrm{br},1}$ and $\gamma_{\mathrm{br},2}$. The parametrization of the electron energy distribution allows to define up to two spectral breaks, while two breaks have only been applied in the case where a one-break spectrum was not sufficient to reproduce the data (see Table 6.5). The contribution of star light from the host galaxy depicted in Figures 6.17 and 6.18 has been included according to [S^{+}98b].

Table 6.5: Values for the model parameters as obtained during the SSC modeling. Together with values describing the average state (adapted from [A^{+}11b]), parameter values obtained during fits in the course of this work are shown, describing the flaring SEDs shown in Figures 6.17 and 6.18. For the 2 zone model, only the parameters defining the additional zone (on top of the average emission model) are given. For details on the parameters and the assumed scenarios see text.

Parameter	Av. State	Flare 1 one zone large region	Flare 1 one zone (very) small region	Flare 2 one zone large region	Flare 2 two zone small region
R [cm]	1.3×10^{17}	1.3×10^{17}	6.3×10^{15}	1.3×10^{17}	1.0×10^{16}
B [mG]	15	2.7	30	5	8.5
δ	12	12	18	12	18
n_e [cm^{-3}]	635	7.7×10^3	6×10^4	1.3×10^3	7×10^3
γ_{min}	600	1×10^3	300	1×10^3	4.0×10^4
γ_{max}	4×10^4	1.5×10^7	3×10^6	1.5×10^7	3.0×10^6
$\gamma_{br,1}$	9×10^5	-	-	1.2×10^6	8.0×10^5
$\gamma_{br,2}$	1.5×10^7	-	-	1.5×10^6	-
α_1	2.2	2.3	2.2	2.2	2.0
α_2	2.7	-	-	2.4	-
α_3	3.65	-	-	3.65	3.5

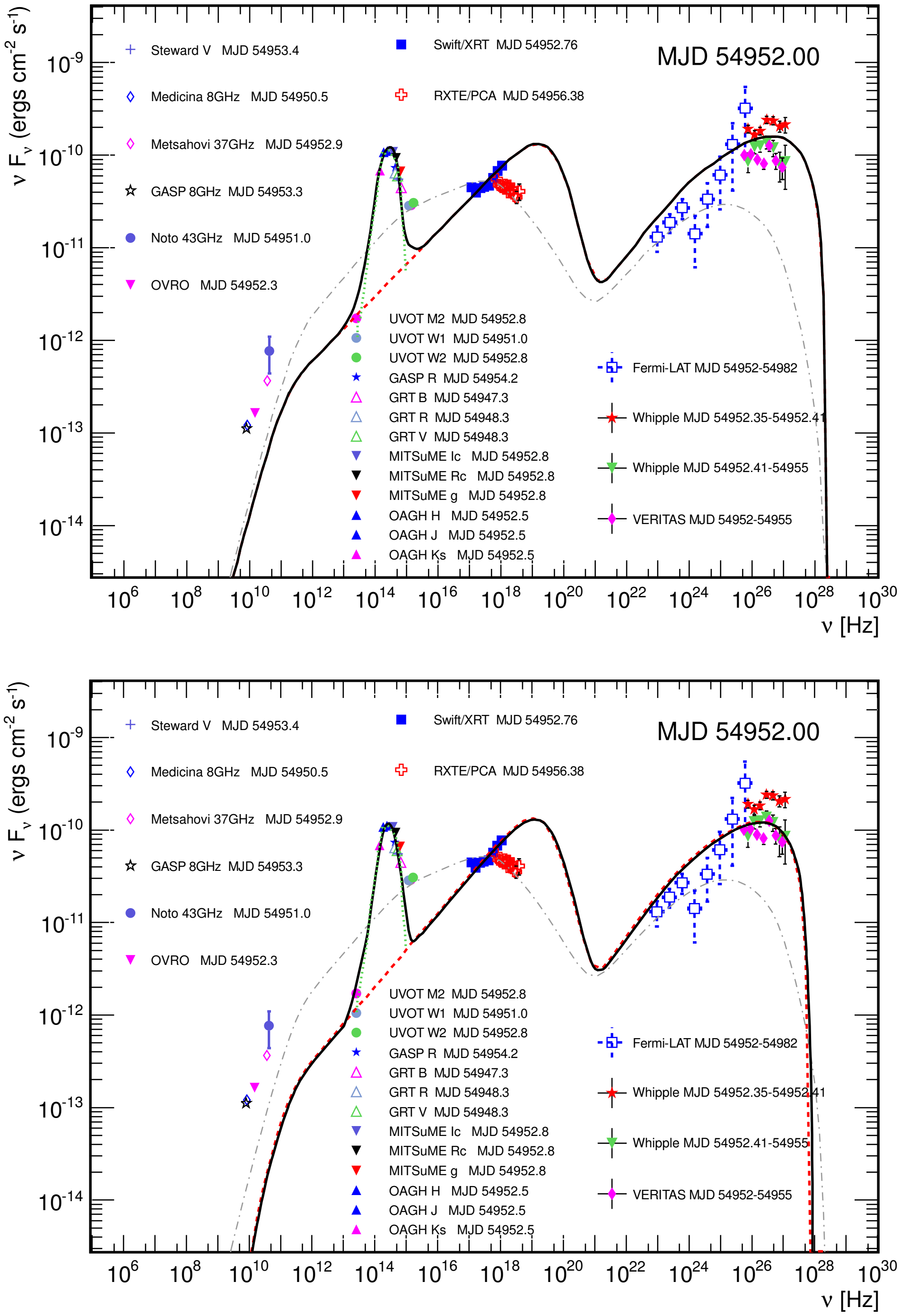

Figure 6.17: SSC models for the SED obtained around the first VHE flare (MJD 54952). Upper panel: one zone model, assuming an emission region of the same size as the one that was assumed for the average state model in [A+11b]. For the used parameter values see second column in Table 6.5. Lower panel: one zone model, assuming a smaller region and an increased Doppler factor compared to the average state model. For the parameters see third column in Table 6.5. The emission from the modeled region (red dashed line), the contribution of the host galaxy (green dotted) and the sum of the two (black solid) are shown. The average model is drawn for comparison (grey dot-dashed).

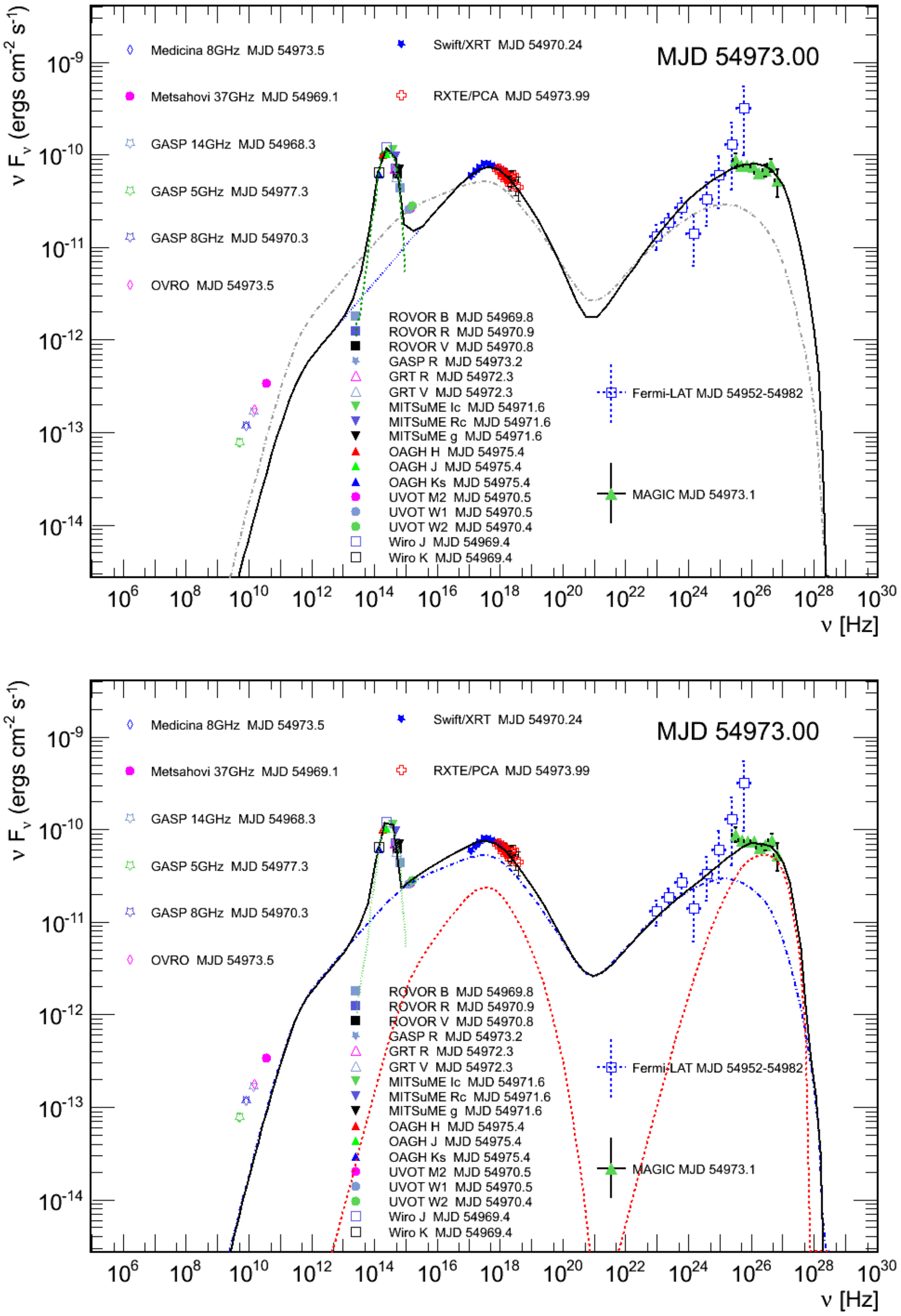

Figure 6.18: SSC models for the SED obtained around the second VHE flare (MJD 54973). Upper panel: one zone model, assuming an emission region of the same size as the one assumed for the average state model [A+11b]. The emission from the modeled region (blue dotted line), the host galaxy (green dashed) and the sum (black solid) are shown. The average model is drawn for comparison (grey dot-dashed). See fourth column in Table 6.5. Lower panel: SSC model assuming two independent emission zones, while a smaller blob responsible for the flaring emission has been added to the quiescent blob with parameters found in [A+11b]. The average state model (blue dash-dotted line), the emission from the additional region (red dashed), from the host galaxy (green dotted) and the sum of all (black solid) are shown. For the parameters which characterize the additional emission region see last column in Table 6.5.

As a result of the modeling, the second flare (MJD 54973) can be reconstructed by the two zone model, while applying a reasonable choice of parameter values. While the one zone model appears also to reconstruct the data points fairly well throughout most SED parts, it does not allow to describe the UV data points. Both possibilities are characterized by a shift of the electrons to higher energies (higher γ_{min} and γ_{max} as well as a harder spectrum) and a lower magnetic field compared to the average state, while the two zone model is clearly to be favored.

Due to the shift to higher energies and the steep increase of the synchrotron peak, the SED around the time of the first flare (MJD 54952) can neither be reproduced with the one zone nor with a simple two zone model. While again, one zone does not fully explain the flux level seen in the UV range, the two zone model cannot reproduce the sharp synchrotron peak and the existence of an IC peak at the same time. The seen behavior might be explained in the scope of more complex scenarios. One possibility could be that an additional (more energetic) electron population, which produces the shift in the synchrotron peak, appears to be cospatial with the average state emitting electrons. In this way, enough low energy photons would be present to be upscattered by the freshly accelerated electrons, while only a weak suppression due to Klein-Nishina-effects would take place. However, the scope of this thesis has been restricted to simple, straight-forward models, and as this scenario involves several additional free parameters, it was not tested in the course of this work.

6.8 Summary

During the 4.5 months covered by the MWL campaign presented in this chapter, the blazar Mrk 501 showed a general behavior of stronger flux variability towards larger frequencies. On top of this, it showed two episodes of increased activity in the emission of VHE gamma-rays. The extensive data set allowed to investigate changes in the emission at other wavelengths in correlation to these events. While the source appeared to be quiet and stable in the range from radio to optical emission, some activity has been seen in the X-ray regime, including one large outburst which can be seen as contemporaneous to one of the events visible at TeV energies. At MeV-GeV energies, only long time variations (30 days) were probed, but an increased activity over the 30 days period covering both flaring events was seen. Regarding a possible correlation of flux changes between the different bands, a significant connection could only be found between the X-ray and the VHE bands, and only for the case when the outbursts were included in the light curves.

In the MWL picture, the two VHE flares differ profoundly from one another. The first event around MJD 54952 shows a rapid flux increase in VHE gamma-rays on time scales shorter than 1 hour, which reaches flux levels of 6-10 times the baseline flux. Although strictly simultaneous observations in the X-ray band are missing, contemporaneous (within 7 hours) measurements show that the overall flux at X-ray energies does not exhibit a significant increase around that time. However, a spectral change is apparent, which indicates a shift of the synchrotron peak to higher energies. Unfortunately, this observation cannot be confirmed by measurements in the range $> 4\,\mathrm{keV}$, as there are no data available close in time to the event. Complementary measurements of the optical polarization reveal an additional coinciding change in the behavior of the source: While prior to MJD 54952, the degree of polarized light was comparably large (≈ 5.3%), it dropped down by ≈ 15% right when the flare occured. Furthermore, a rotation in the angle of the electric field vector (EVPA) is seen prior to the flaring event, which comes to a halt at the time of the gamma-ray outburst. The combination of a slight drop in degree and the comparably short rotation of only 15 degrees cannot, in themselves, be argued as an outstanding event, as changes of this extent could still be ascribed to a random behavior of turbulent plasma regions. The coincidence with the gamma-ray flare however suggests a common origin of these events.

The second flaring event shows a different behavior both in the VHE gamma-ray and the X-ray band: Based on the MAGIC observations from MJD 54973, no significant intra-night variability of the emission in VHE gamma-rays is seen, while in connection with the observations performed by the Whipple telescope, the source appears to show flux changes on time scales of days, lasting at least for 5 days. Unfortunately, no observations took place on the two days prior to the seen outburst. During this event, Mrk 501 was also active at X-ray energies. *Swift*-XRT and *RXTE*-PCA saw flux increases by factors of 1.5 up to 2.5 during a period of rising and falling flux levels, until the emission was again more stable at the level of the base line around MJD 54979. All things considered, the source seems to show a behavior of erratic flaring in both, VHE gamma-rays and X-rays, over a period of up to 10 days. In contrast to the first flaring event, unfortunately no optical polarization data are available for this period of time.

Complementary VLBA measurements reveal an increased radio activity in May compared to several snapshots prior to the campaign, which is particularly prominent at the location of the core.

The reconstruction of the SEDs of these two states in the scope of a simple SSC model revealed that an exemplary SED around the second flare could well be explained in the scope of a two zone SSC model. However, it appeared not to be possible to model the entire SED during the first flare with a simple (one or two zone) SSC model.

6.9 Discussion

An overall trend of a more pronounced variability at higher frequencies has been seen before in the X-ray regime [G$^+$06] and in the VHE regime [A$^+$07c]. While in the course of the campaign presented here, such a dependency has not been seen within a particular waveband, this trend has been observed throughout the entire electromagnetic spectrum, which establishes the source as being most variable at the highest energies. An indication for the general trend of a harder spectrum in VHE gamma-rays during high flux states (see e.g. [A$^+$07c]) was also seen. Although hints for a general correlation between the X-ray and the VHE gamma-ray band have been found in previous studies, e.g. [P$^+$98, G$^+$06], in this work a temporal correlation between flux changes in these band were only seen for light curves which are dominated by the flaring emission. However, the lack of correlation during low state emission might be influenced by the fact that many observations were not strictly simultaneous.

The occurrence of flaring events is a phenomenon that is well-known in Mrk 501. However, the detailed investigations of the individual events and their temporal proximity permits several unprecedented conclusions.

The appearance of the first flaring event seen around MJD 54952 is dominated by a strong and fast increase in the gamma-ray flux, which is not accompanied by a notable flux increase in the X-ray band. Based on these observations, this event has previously been referred to as an *orphan flare* [Pic11, NST12]. This conclusion would have made a strong impact, as an event of this type has only once (or tentatively twice) before been seen for an HBL [K+04, B+05] and would have challenged the currently favored explanation of HBL SEDs within leptonic emission scenarios. However, the pronounced hardening and upward curvature seen in the *Swift* spectra indicate a substantial shift of the synchrotron peak frequency to higher energies, possibly to beyond 100 keV. This clearly contradicts the hypothesis of an orphan flare event. A shift in the synchrotron peak during high states of the source has been noticed before, but a shift of this dimension has only been observed during the exceptional flare of Mrk 501 in 1997 [P+98]. The occurrence of such a remarkable shift of the synchrotron bump during a smaller outburst as seen here is quite surprising and suggests that the behavior seen in 1997 does not only occur for a single, outstanding event, but could characterize the source more generally.

Although the peak of the high energy bump is not fully resolved due to the long integration time required for the *Fermi*-LAT spectrum, a shift to higher energies can also be noted here. Such a move of the entire SED towards high energies has previously been interpreted as a shift in electron energy distribution towards higher energies (see e.g. [P+98, A+07c]), while the comparably small shift of the high energy bump could be explained by Klein-Nishina effects [TMG98]. In the SED modeling performed in the course of this work, neither the one zone scenario (involving only one electron population) nor the scenario of two separate zones allow to describe the entire SED, neither with a change in the electron energy distribution nor with a change of surrounding parameters for an isolated region (or a combination of both). More complex models involving two cospatial electrons populations which interact with the combined field of synchrotron photons might still be able to reconstruct the SED, but were beyond the scope of this work. However, the rapid VHE variability (on time scales down to minutes) and the remarkable change in the synchrotron emission suggest the interaction of the emitting region with a shock, or the injection of fresh, newly accelerated particles into the region. Cooling times generally depend on the energy of the particles, so that fast cooling of the high energy electrons could account for the rapid flare, while a slower cooling of the lower energy part would explain the increased VHE flux level for the order of days subsequent to this event.

A strong argument in favor of this scenario is the change in the optical polarization, which has been found to be coinciding with the TeV outburst. This is the first time such an observation has been made for a source of the HBL class. The seen drop in the degree of optical polarization and the stop of the rotation of the EVPA, coinciding with a flaring event in gamma-rays, strongly support the scenario of particle injection into the emitting region, which would introduce a turbulence and disturb the (partly ordered) movement of the particles in the surrounding magnetic field.

The second flaring event (around MJD 54973) differs from the first one in terms of flux level, the involved time scales and the changes in the SED shape. The overall SED could be reconstructed in the scope of a SSC model involving two (independent) zones, whereas a one zone approach did not permit to reproduce the measurements in optical and UV

frequencies. Regarding the SED, the overall increase in flux, which is not accompanied by a significant shift of either the synchrotron or the IC bump, do not suggest a substantial change in the electron energy distribution. The reproduction of the higher flux at X-ray and TeV energies have been achieved by increasing the electron density n_e and the Doppler factor of the region, while $F_{sync} \propto n_e$ and $F_{IC} \propto n_e^2$ (in the Thomson regime). Due to the seen variability on time scales of single nights (but not within a particular observation), the size of the emission region has been reduced by about one order of magnitude compared to the quiescent state. In contrast to the sharp outburst in the VHE range around MJD 54952, a state of enhanced activity over several days in both, X-ray and VHE frequencies, is seen here. As the cooling time for high energy electrons should be short, a mechanism of continuous particle injection would be needed to explain this high activity on these time scales, based on the shape of the electron energy distribution [P+98]. Alternatively, the emission region could be traversing an extended shock region, which results in a compression of the emitting region and an increase of the density of the present particles.
The latter explanation would be in agreement with an alternative scenario, which was initially suggested by Marscher et al. for flaring events seen in the sources BL Lacertae (LBL) in 2005 and PKS 1510-089 (FSRQ) in 2009 [M+08, M+10a]. These observations are similar to what has been presented above, as they also feature changes in polarization in coincidence with flaring events in other bands (or the start of a sequence of flares). While this behavior has been observed for the first time in an HBL during the campaign which is subject to this thesis, the scenario suggested by Marscher et al. might give some additional implications on the possible interpretation. Thus, it will in the following be discussed in the context of the presented Mrk 501 observations:

In [M+08], Marscher et al. report on a MWL campaign on BL Lacertae, which covered a double flare in the optical regime, with a separation of 40 days (see the lower panel of Figure B.11). While a significant detection of emission above 200 GeV (probably due to an increased flux state) was seen at the time of the first flare, an increased level of X-ray emission was observed around the time of the second outburst. Coinciding with the first optical flare, optical polarization measurements revealed a drop in the polarization degree at the time of the flare, while a strong rotation of the EVPA appears to terminate soon after the outburst. Complementary radio images obtained with the VLBA allow to locate the position of the core at the base of the jet and the location of a second feature within the jet. A series of these images permits to trace the feature's path, while it appeared to pass through the region of the core right before the second outburst that was seen (see the upper panel of Figure B.11). The radio band also shows significant variability.

Marscher et al. suggest that these two subsequent events are stemming from the same region (or feature in the jet). They propose a jet model, which defines the radio core not as the region of opacity $\tau = 1$ (see section 5.2), but as a region further downstream, which is characterized by a standing shock. Upstream of this region, they assume an *acceleration and collimation zone* of the jet, which is dominated by a helical magnetic field (see Figure 6.19). Based on this model, the first flare event is explained as the time when the emission features travels along and finally leaves the last spiral arm of the magnetic field, which is followed by entering a more turbulent zone. The second event corresponds to the passage of this feature through the shocked core region, which causes a chaotic behavior on longer time scales. The radio images recorded around this time support this assumption. A similar observation on the FSRQ PKS 1510-089 has been presented in [M+10a].

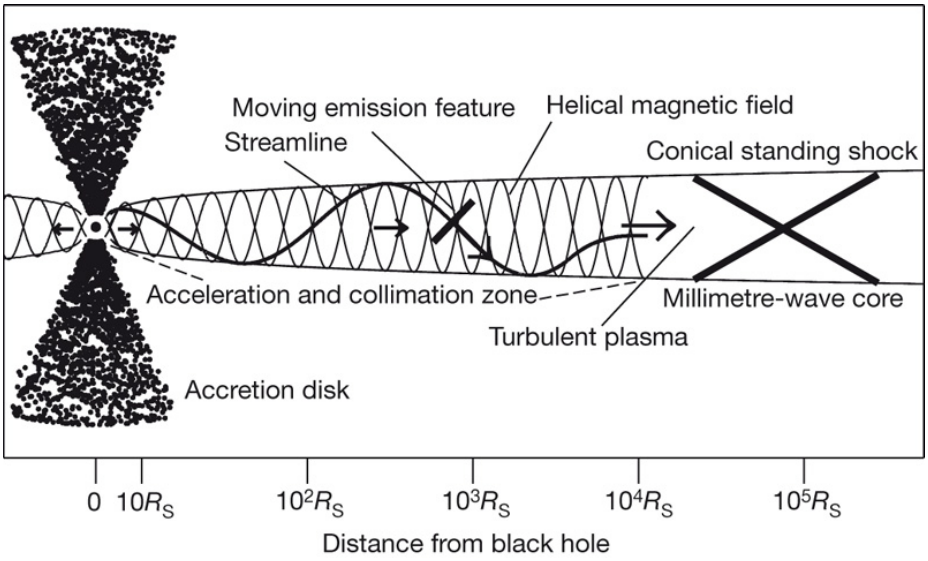

Figure 6.19: Schematic view of an inner jet model of the source BL Lacertae, which has been proposed by Marscher et al. in [M+08]. Two flaring events are interpreted as a shock moving down the jet along the streamline. The first flare is seen at the time when the shock passes the last spiral arm, before it enters the turbulent plasma region, while the second flare is explained as the passage of the shock through the core region. The distance is shown on logarithmic scale in terms of the *Schwarzschild radius* of the black hole (R_S). Figure from [M+08], see this reference also for more details.

The observations on Mrk 501, which have been subject to this work, show several similarities to the observations on BL Lacertae (and PKS 1510-089). The objects are characterized as HBL and LBL (FSRQ), respectively, because they exhibit different peak frequencies of the synchrotron bump. Therefore, the optical variability seen in BL Lac corresponds to variability in the X-ray band in Mrk 501. While a strong outburst in the TeV regime during the first event of X-ray activity is seen for Mrk 501, also BL Lac gives hints for activity in that band during the first optical flare. The changes in polarization coincide with flaring events in both sources (and for both with the first one in a series of two). The second flaring episode is featured by an increased synchrotron bump flux over a longer time span, while for BL Lac no accompanying flux increase in TeV was detected. The measured degree of polarization in Mrk 501 ($\approx 5\%$) appears to be small compared to BL Lacertae (up to 18%). However, the jet contribution makes up only 25-30% of the total emission of Mrk 501 in the optical band, as the host galaxy strongly dominates here. Therefore, the measured polarization degree corresponds to a fraction of $\approx 15-20\%$ of polarized emission from the jet, which is very similar to what is observed for BL Lacertae. The missing variability in the radio band for Mrk 501 is consistent with what has been seen previously for HBLs, see [L+11]. Unfortunately, no direct tracing of a feature's movement in the jet could be performed, as no VLBA images were taken during that time, unlike in the case of BL Lac.

Although the two observations do not report on entirely equal behavior over all bands, the similarities suggest that the presented scenario could also be an applicable explanation for the observations of Mrk 501 in 2009. In this context, the first flare might stem from the fact that a blob of highly energetic particles leaves the collimation region and enters a more turbulent region. However, the steep rise of the synchrotron peak can not be easily accommodated here. The second flare is more straight forward to explain in this scenario, as it would correspond to the passage through a compressed, shocked region, possibly the core seen in radio images. The enhanced activity in this region during May 2009 seen in high resolution radio measurements (VLBA) supports this hypothesis.

In this scenario, it is not quite clear if the emission feature, which causes the flaring events, might also be the origin of the quiescent emission, or if this is produced by another feature or in another region of the jet. In the context of the (simple) SSC modeling presented in this work, the latter scenario (including two zones) seems to be better suited in order to reproduce the SED during the flaring states.

Beyond the detailed explanation of the observed behavior of Mrk 501 during this campaign, the observational details clearly reveal common phenomena which have not been seen for an HBL before, but were studied already for LBL type sources and FSRQs. This is quite surprising for sources which exhibit relativistic jets with very different characteristics, namely slow apparent speed and low overall power (together with seen limb brightening, which suggests a *spine-layer* structured jet) in Mrk 501, as opposed to sources which exhibit more jet power and fast jet velocities. This gives a strong indication for the intrinsic similarity of these different classes, as proposed by Fossati et al. [F+98a] (see also subsection 5.2.1). Recent observations of rapid variability in the LBL BL Lacertae confirm this further [A+12c], as flux changes on such time scales are more commonly found in objects of the HBL class.

In this light, the performed observational campaign and respective analyses can be seen as fresh support to the claim of intrinsic physical similarities of the different blazar subclasses.

6.10 Conclusion

In the course of the work presented in this chapter, the light curves of Mrk 501 have been investigated in terms of the overall variability and correlations between the different wavebands. Two flaring episodes have been identified, which showed very different behavior in the broad-band spectral energy distribution. Based on the prior description of the quiescent emission in the context of SSC emission models, the reconstruction of the two SEDs has been tried using one zone and two zone SSC models. For both cases, the simplest SSC model, including only one emission zone, was not sufficient to reproduce the entire SED. While the second event could be accommodated well in a two zone model, the first flare could not be entirely described by either one or two zones. More complex scenarios of two interacting zones or a jet of a different structure (*spine-layer*) might be able to explain the SED during the first flare, but were not tested in the scope of this thesis.

Tentative explanations have been given for the spectral behavior seen in these two different flaring episodes: Based on the modeling, the first event could not be entirely explained, but seems to be characterized by an injection of particles into a formerly quiescent region, while the second flare is more consistent with a compressed emission region. A comparison to earlier data from the LBL object BL Lacertae (and the FSRQ 1510-089) gives strong hints towards the idea that the emission is produced upstream of the radio core within the jet, where the magnetic field is strongly collimated, and directly at the core. Accordingly, this scenario could explain the two flaring events in connection with each other.

The non-strict simultaneity of the spectral distributions measured in the VHE and the X-ray regime however, does not permit an ultimate conclusive interpretation.

Beyond the explanation of the seen event itself, the observations presented in this chapter were able to confirm similarities between the different subclasses HBL, LBL and FSRQ. This clearly supports the hypothesis that the sources are intrinsically more similar than is suggested by the seen differences in energetic output, SED structure and jet morphology, and that the differences could be governed by only a few global parameters.

Chapter 7

AGN: Sources of neutrinos and charged cosmic rays?

7.1 Motivation and Introduction

One of the most pressing, but still unresolved questions in astroparticle physics today is the origin of the highest energy cosmic rays. Following the considerations given in subsection 2.3.7, the class of AGN is a very promising candidate for the production and emission of charged cosmic particles. The difficulty in the search for the origin of CRs has already been discussed in subsection 2.1.1, consisting in the fact that a direct search is not possible, as the CR flux is isotropized by deflection on magnetic fields. The only exception to this could be the highest energy CRs, as their Larmor radius could be large enough not to be too disturbed by the prevailing magnetic fields.

In order to identify their sources anyhow, other messenger particles can be addressed, as their production might be linked to the origin of the CRs. Following hadronic scenarios of high energy emission from blazar jets, not only gamma-rays but also neutrinos should emerge from interactions of highly energetic hadronic particles with the jet environment. Both particles are neutrally charged messengers which are not deflected during their propagation from the source to the Earth and can thus be used for dedicated studies of their sources. While the possible production mechanisms of gamma-rays in AGN are manifold and can often be fully accommodated in purely leptonic models, as was discussed in subsection 5.2.3 and the previous chapter, the detection of neutrinos would be a strong confirmation for the participation of hadrons in the acceleration and emission processes at work there. For this reason, the possible detection of high energy neutrinos from an AGN is referred to as a “smoking gun” evidence for the case of hadronic jet models.

The drawback in the use of neutrinos is their small interaction probability. After the AMANDA neutrino detector did not reveal a signal of cosmic neutrinos of point sources beyond the flux of neutrinos which are produced in atmospheric interactions [A+09a], the successor experiment IceCube is now searching for such a signal. IceCube has been completed in 2010 and employs a cubic kilometer of antarctic ice as its detection volume. For an overview of the experiment see [HK10]. So far no significant detection of high energy neutrinos from an AGN could be claimed.

In the course of this chapter, an exemplary estimation of the possible neutrino flux from the blazar Mrk 501 is conducted, assuming, in contrast to the considerations in the previous chapter, that the entire gamma-ray emission seen from the source is produced in

hadronic interactions. In this scenario, the flux in gamma-rays and in neutrinos should be linked via the production process. The method presented in the following is independent from dedicated acceleration and emission models and is based only on bolometric considerations. It has been discussed before in [HZ97] and has been recently applied also to GRBs [B+10]. The fact that a generation of new instruments both in the gamma-ray and the neutrino field are at hand now suggested a revisit of the method in order to get a better estimation of the detectability of neutrinos from AGN.
The results which are presented in this chapter have been obtained in cooperation with A. Ó Murchadha and F. Halzen and have partly been shown at the international workshop *Beamed and unbeamed gamma-rays from galaxies*. They have been published in the corresponding proceedings [D+12].

7.2 The Process

The main emission processes which are thought to produce the highest energy photons seen from blazars have been outlined in chapter 5. Leptonic models assume an interaction of synchrotron photons or external photons with a population of highly relativistic electrons, which leads to the production of high energy photons via the *inverse Compton effect*. In hadronic models, which shall be assumed here, high energy photons can be produced via several different processes, which were briefly discussed in subsection 5.2.2. In the following, photo-hadronic interactions will be discussed: when protons interact with the surrounding field of photons (or among the population of protons themselves), resonances can be produced, which decay further into charged and neutral mesons with a fixed ratio. For simplicity, the $\Delta-$approximation is applied and only π mesons are considered, which yields

$$p\,\gamma \rightarrow \Delta^+(1232) \rightarrow \begin{cases} p\,\pi^0, & \text{fraction } \frac{2}{3} \\ n\,\pi^+, & \text{fraction } \frac{1}{3}, \end{cases} \tag{7.1}$$

cf. [Bec08] and subsection 2.2.5. The resulting neutral pions decay further, and therein produce highly energetic gamma-rays which, in this scenario, make up the second bump in a blazar SED:

$$\pi^0 \quad \rightarrow \quad \gamma\,\gamma. \tag{7.2}$$

The charged pions decay into leptons via the process

$$\pi^+ \quad \rightarrow \quad \mu^+\,\nu_\mu \rightarrow e^+\,\nu_e\,\overline{\nu}_\mu\,\nu_\mu, \tag{7.3}$$

resulting in the emission of neutrinos which might serve as the direct experimental confirmation of this process. The fact that the ratios in which the charged and neutral pions are produced are fixed, directly relates the measured flux in gamma-rays to a flux in neutrinos which should be produced within the process, cf. [D+12].

7.3 The Method

For the estimation which is presented here, the interaction of protons with a present photon field is considered. This field could consist of synchrotron photons which are emitted by the accelerated particles (including leptons which should also be present in the region) or of thermal photons which are emitted for example by the accretion disk. No specific scenario is chosen here, but the photon field is assumed to be constant.

Proton-proton-interactions are neglected for the study presented here, while it is stated in [BB09] that photo-hadronic processes should dominate in the investigated scenario.

An assumption is made for the spectral energy distribution of the accelerated protons, and thus for the pions, based on the particle distributions typically produced in Fermi acceleration processes. Subsequently, the spectral distribution of the resulting photons and of the first neutrino can be determined following two-body decay kinematics [Ste71, Der86, Gai91]. The spectral distribution of the second neutrino, which emerges as a decay product of the muon, corresponds to a three-body decay of a particle resulting from two-body-decay and is determined following [Gai91] (see also [B+10] for explicit calculations). With an arbitrary normalization of the input spectrum, the gamma-ray and the neutrino spectra are normalized to each other, but lack an absolute normalization. This can be derived from measurements of the second spectral bump in the SED of an AGN, which holds the entire energy that is deposited in gamma-rays. As shown in the previous chapter, this bump can be well probed with the current generation of instruments. However, two effects have to be considered, which might alter the initially produced gamma-ray distribution. One is the attenuation of the gamma-ray flux by interactions with low energy photons of the EBL. For the application presented below, the measured gamma-ray spectra have been corrected for EBL absorption using the model by Franceschini from 2008 [FRV08]. The second effect is the cascading of gamma-rays within the source (see subsection 2.2.6). In order to detect gamma-rays which are produced in the above mentioned processes, they first have to escape the emission region. This region is typically filled with (synchrotron) photons, which actually is a requirement for a detectable gamma-ray flux in the course of a photo-hadronic model. The present photons can interact with the gamma photons, resulting in a cascading of the gamma-rays towards lower energies, cf. subsection 2.2.6. For the application presented here, it is assumed that most of the photons still contribute to the energy deposited in the second spectral bump. Particle cascades in emission regions in AGN jets are usually assumed to be "non-saturated", as particles have a high escape probability due to the limited size of the region, and thus terminate after few circles (see also subsection 2.2.6). Following these considerations, the pion-induced gamma-ray spectrum $dN_{\pi^0\rightarrow\gamma\gamma}/dE$, and thus the neutrino spectrum, can be normalized with the help of measured gamma-ray spectra dN_{meas}/dE, in terms of the deposited energy according to

$$\int\limits_{E_{min}}^{E_{max}} E\frac{dN_{\pi^0\rightarrow\gamma\gamma}}{dE}dE = \int\limits_{E_{min}}^{E_{max}} E\frac{dN_{\mathrm{meas}}}{dE}dE, \tag{7.4}$$

cf. [D+12].

7.4 Application to data

7.4.1 Data selection

The above presented method is applied to the blazar Mrk 501. To derive the energy deposited in gamma-rays, the measurements of the high energy spectral bump which have been presented in chapter 6 have been used. This includes the low state and high state spectra measured by the *Fermi*-LAT (see Figure 6.16 for the high state spectrum and the upper left panel of Figure B.9 for the low state spectrum; see also [A^+11b]), the low state spectrum derived from MAGIC data in the course of this work and the high state spectrum derived from the VERITAS data, as this represents the highest flux state seen from this source in the course of the presented campaign (for both spectra see Figure 6.12). As already mentioned, the VHE spectra have been corrected for EBL absorption according to [FRV08].

7.4.2 Parametrization of the high energy bump

Based on the measurements in the *Fermi* and IACT regime, the shape of the second peak in the SED of Mrk 501 can be derived for both cases. Without imposing any prior knowledge or assumptions derived from particular emission models, this peak can be parameterized by a polynomial function of 2^{nd} order, which is fitted to the data points in the representation $\log(\Phi)$ vs. $\log(E)$:

$$\log(\Phi) = p_0 \cdot (\log(E))^2 + p_1 \cdot \log(E) + p_2. \tag{7.5}$$

The parameters which are found for the two flux states of the source are given in Table 7.1. The spectra and the respective fit functions are shown on the left hand side of Figure 7.1.

Table 7.1: Fit parameters for the parametrization of the measured gamma-ray spectral bumps of Mrk 501 in two different flux states.

Source State	p_0	p_1	p_2
Low	-0.07 ± 0.02	-0.17 ± 0.06	-10.86 ± 0.03
High	-0.08 ± 0.02	$+0.01 \pm 0.06$	-10.20 ± 0.02

7.4.3 Flux normalization via integration

The integration limits for the energy normalization using this parametrization are chosen as $E_{min} = 10^{-5}$ TeV and $E_{max} = 10^8$ TeV. While the lower limit is given by the left flank of the second SED bump, the upper limit is suggested by the expected cut-off in the spectrum of protons coming from cosmic accelerators at an energy of 10^9 TeV. These limits indicate an extrapolation of the measured spectra for the integration, but as the main contribution comes from the well determined part of the spectrum, this appears to be feasible.

7.4.4 Resulting neutrino fluxes

The derived neutrino spectra span an energy range from the pion production threshold at tens to hundreds of MeV up to 10^8 TeV, where the suppression of highly energetic protons creates a cutoff (cf. subsection 2.1.1). The spectra are shown on the right hand side of Figure 7.1. For the low state, three different assumptions of the initial pion spectrum have been used for the estimation (top panel). A comparison of the low and high state flux of Mrk 501 for an initial spectral index of $\alpha_\pi = -2.0$ is shown in the lower panel. Additionally, upper limits are drawn, which were obtained from the IceCube neutrino detector when 40 of the final 86 strings where in operation (IC-40). They have been derived for an $E^{-2.0}$ spectrum in a live time of 375.5 days and correspond to the Feldman-Cousins 90% confidence intervals [A+11a]. The flux of neutrinos stemming from hadronic interactions in the atmosphere, which is the major background to the measurement with IceCube, has been calculated according to [Ho07].

7.4.5 How many events could IceCube see?

IceCube accesses an energy range from 0.1 TeV to 10^7 TeV. This covers a large fraction of the expected neutrino signal derived above. The number of events which should be seen in IceCube can be determined using the effective area of the detector. In the presented study, the standard effective area predicted for a configuration of 80 strings has been applied. The expected number of events per year, derived for an initial proton/pion spectral index $\alpha_\pi = -2.0$, are shown in Table 7.2. Also the expected number of background events in that time are given there, based on the atmospheric neutrino flux given in [Ho07]. For both flux states, the significance for a detection based on these numbers is determined according to

$$\sigma = \frac{\text{signal events}}{\sqrt{\text{bg events}}}. \tag{7.6}$$

It has to be noted that the number of events for the high state of the source has been derived under the assumption of a constant flux at this level over an entire year. While this is not a realistic scenario, this presentation has been chosen for comparability.

Table 7.2: Predicted event numbers for the examined blazars to be seen within one year with the IceCube detector, based on the calculated neutrino flux and an effective area which has been predicted for 80 strings.

Source	events [year^{-1}]	$\frac{\text{signal events}}{\sqrt{\text{bg events}}}$
Mrk 501 low state	1.70	0.372
Mrk 501 high state	6.232	1.365
Atmosph. background	20.84	-

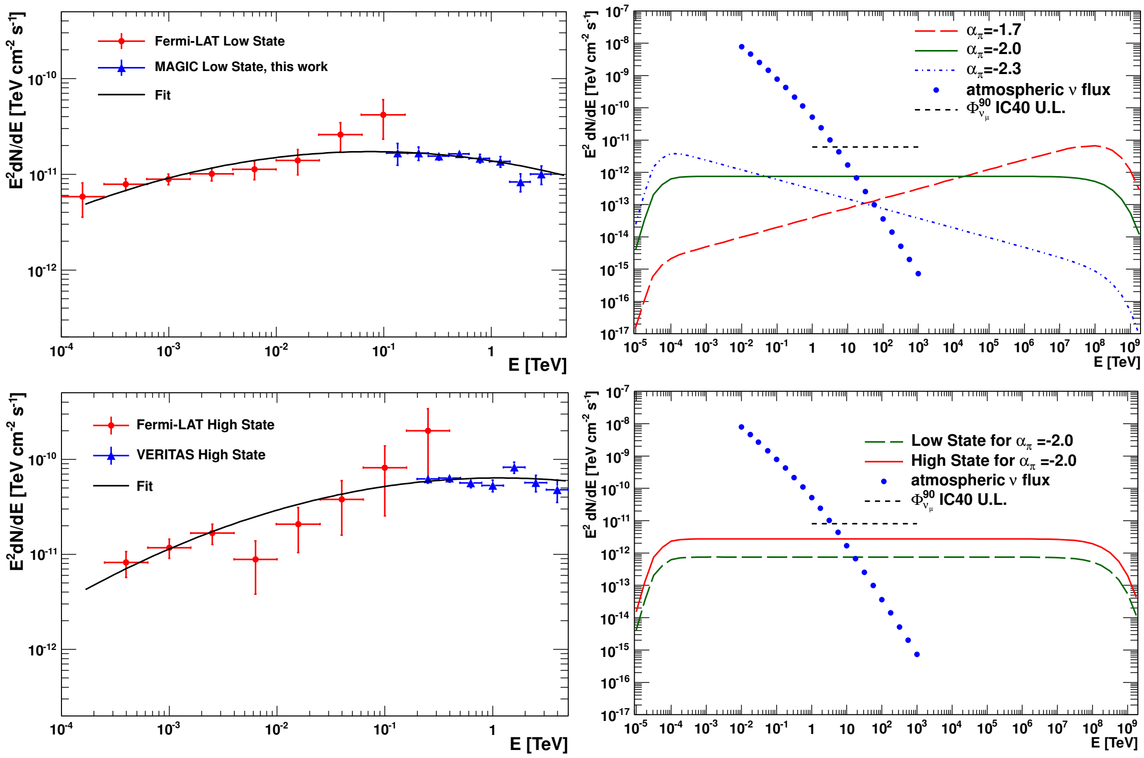

Figure 7.1: Left hand side: Measured gamma-ray spectral points from *Fermi* and IACTs and the according fits to the high energy peak: Mrk 501 in low state (top panel) and high state (bottom panel). Right hand side: Predicted neutrino spectra for Mrk 501. Top panel: Estimations for three different initial π-spectra for Mrk 501 in low state. Bottom panel: Estimations for an $\alpha_\pi = -2.0$ spectrum of Mrk 501 in low and hight state. IC-40 limits are drawn according to [A$^+$11a]. The atmospheric neutrino flux is determined according to [Ho07]. These figures have partly been presented in [D$^+$12].

7.5 Discussion and Conclusion

Based on the predicted number of neutrino events for the low state which has been derived in the course of this study, it is apparent that a single source of this type is not close to detectability in a standard IceCube point source analysis. The flux limit which is presented in Figure 7.1 corresponds to less than half of the volume of the finished detector (IC-40 configuration) and will be lowered for data taken with the completed detector. Furthermore, the significance of a possible detection will increase roughly with the square root of the exposure time. Therefore, the predicted fluxes could be within reach for the full detector after several years of data taking. However, the key task in order to improve the sensitivity is the suppression of events stemming from the atmospheric background. An analysis of IceCube data collected within a certain time window around a detected gamma-ray high state could be more promising, as this would substantially improve the signal to background ratio by removing most of the background events. Corresponding studies on temporal correlation of the optical, gamma-ray and possible neutrino signal from AGN have been presented in [ESR12].

Beside further possibilities to improve the ratio of signal to background, like an additional optimization of the considered energy range, the stacking method which combines the significance from several sources within one analysis could yield an excess which is strong enough to detect a neutrino signal from the overall sample [A+06b, B+07]. The corresponding data catalog should comprise several promising gamma-ray sources, possibly during high states. Beyond the source class of HBLs which is represented here by Mrk 501, also more powerful blazars (LBLs and FSRQs) should be included in such a source sample.

The study presented here has been applied to derive a rough estimate for the feasibility of detecting a neutrino flux from the HBL Mrk 501. It delivered meaningful results, which do not predict a detection for the immediate future, but motivate the continuation and improvement of the current search strategies. Beyond the application given here, the method could be used in a broader study, to make an estimation of the signal which can be achieved with a *stacking analysis* of a sample of blazars.

Chapter 8

Final Conclusion and Outlook

After an introduction was given to astroparticle physics in general and gamma-ray astronomy in particular, the successful implementation of the novel unfolding program TRUEE into the standard analysis chain of the MAGIC experiment has been presented, along with the very first application of the program to very high energy gamma-ray data. This first *proof of principle* analysis, resulting in an energy spectrum of the Crab Nebula, has proven the compatibility of the program with respect to former unfolding tools and has highlighted the advantages of the new spectral reconstruction method, which is now open to be used by the collaboration and has already drawn interest from other experiments.

The phenomenon of active galactic nuclei has been extensively studied throughout this thesis, following two different approaches. After an introduction to AGN and the subclass of blazars, a multi-instrument study of the VHE gamma-ray source Markarian 501 has been presented, which stands out due to its unprecedented coverage in time and energy. The obtained data provide detailed insights into the broad-band variability of the source, not only in terms of flux changes but focussing on the overall energy distribution. Two flaring episodes have been seen and studied in detail, considering also optical polarization measurements. In this way, a VHE outburst and a coinciding change in the polarization behavior have been detected for the first time in an HBL object. Accompanied with substantial changes in the broad-band spectral distribution, this event appears to be challenging simple leptonic emission scenarios. In the context of previous work on the average emission of the source during this campaign, leptonic models were tried in the course of this thesis in order to explain the spectral energy distributions measured during the two flares. While the first flare event could not be reproduced in this scope, the second event could be well reconstructed, albeit only in a scenario which involves two emission zones. The complexity of the data and the difficulties in modeling call for the testing of a broader range of emission models, like e.g. the spine-layer model or hadronic jet models, which could not be thoroughly studied in the scope of this work.

A comparison to observations on objects of other blazar classes (LBL and FSRQ) revealed similarities which suggest that the flaring events (together with the change in polarization) are linked to the movement of a feature in the helical field of the jet, probably close to the central engine.

Beside the detailed modeling of the flaring events itself, the presented observations uncovered striking similarities to events seen in LBL objects and FSRQs. Despite their differences in the structure of the energy distribution, the overall jet power and measured plasma speeds, the results presented in this thesis give strong hints towards fundamental intrinsic similarities of the different blazar classes.

In a complementary study, the approach of hadronic emission of very high energy gamma-rays was followed in the context of *multi-messenger astronomy*. Based on simple bolometric considerations and the gamma-ray energy distribution obtained previously, a possible neutrino flux from blazars has been estimated, on the example of Markarian 501. While the predictions do, within the limitations of the method, not announce a neutrino signal of a single quiescent source for the near future, a detection of a neutrino flux from a stacked sample of sources, possibly including only time windows of high gamma-ray high activity, could be within reach after some years of event accumulation with the state-of-the-art neutrino experiment IceCube.

The results which have been obtained in the course of this thesis clearly motivate future campaigns on the blazar Mrk 501, as they revealed that the behavior of the source cannot be explained in (very) simple models and needs to be studied in more detail. Furthermore, it suggests that a better understanding of Mrk 501 will strongly contribute to our knowledge on blazars in general, as the observed behavior seems to describe common phenomena which take place in different sources and source classes.
Another conclusion is the importance of combining broad-band observational campaigns with optical polarization measurements and radio imaging of the active regions, which will give a more complete understanding of the structure and evolution of the jets. In the future, such observation will be complemented by the *GEMS* satellite, which will add polarization measurements in the X-ray band. This will be particularly interesting for studies of HBL sources like Mrk 501, which emit most of their synchrotron power in the X-ray regime.
Thorough studies, together with the continued search for very high energy neutrino emission from blazars, promise to uncover the nature of their highly energetic emission in gamma-rays and to eventually solve the riddle of the sources of the highest energy cosmic rays in the near future.

Appendix A

Cuts for new spectral reconstruction method

The standard hadronness and θ^2 cuts which are default values in *made-up.rc* and have been used during the spectral reconstructions presented in chapter 4 are given here.
The cut in the hadronness parameter is following the function

$$f(x) \begin{cases} -0.95 + 7.20 \cdot x - 9.78 \cdot x^2 + 5.77 \cdot x^3 - 1.25 \cdot x^4 & 0.77 \leq x \leq 1.85 \\ 142.57 - 241.22 \cdot x + 153.08 \cdot x^2 - 43.03x^3 + 4.52x^4 & 1.85 \leq x \leq 2.63 \\ 94.06 - 147.67 \cdot x + 91.84 \cdot x^2 - 28.07 \cdot x^3 + 4.21 \cdot x^4 - 0.25 \cdot x^5 & 2.63 \leq x, \end{cases} \tag{A.1}$$

where x stands for $\log_{10}(E_{est})$.

The θ^2 cut is defined as

$$\theta^2 < 0.06 + (\tanh(7 \cdot (-\log_{10}(E_{est}) + 1.7))) \cdot 0.04. \tag{A.2}$$

Appendix B

MWL analysis of Mrk 501

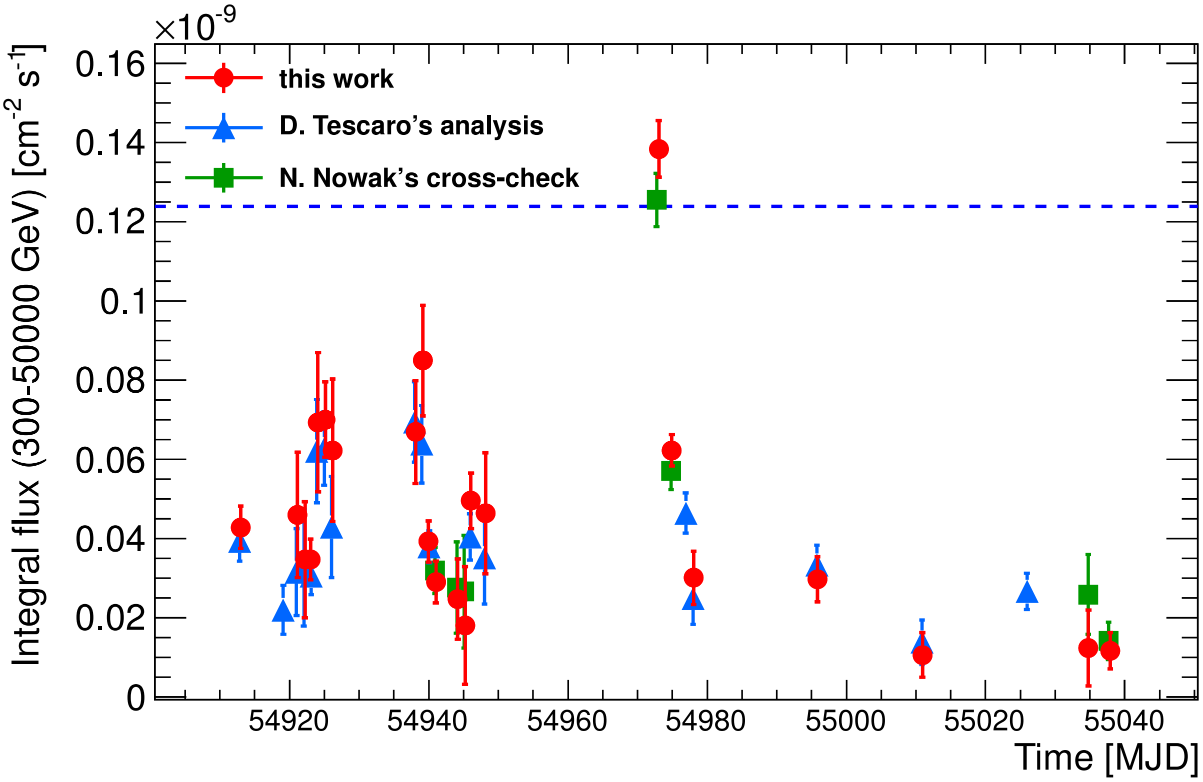

Figure B.1: Mrk 501 light curve from 2009 MAGIC data. Red circles denote the light curve derived from the MAGIC analysis performed in the course of this work, as shown in Figure 6.2. Additionally, the light curve derived in the first analysis of these data by D. Tescaro [Tes10] is depicted as blue triangles. Due to independent quality selections of the data set, some dates are included in one light curve but not in the other and vice versa. Points in the light curve obtained in this work, which were not included in the analysis by D. Tescaro, have been cross-checked by N. Nowak (green squares). A good agreement can be seen for all data points. The blue dashed line indicates the flux of the Crab Nebula in the given energy range.

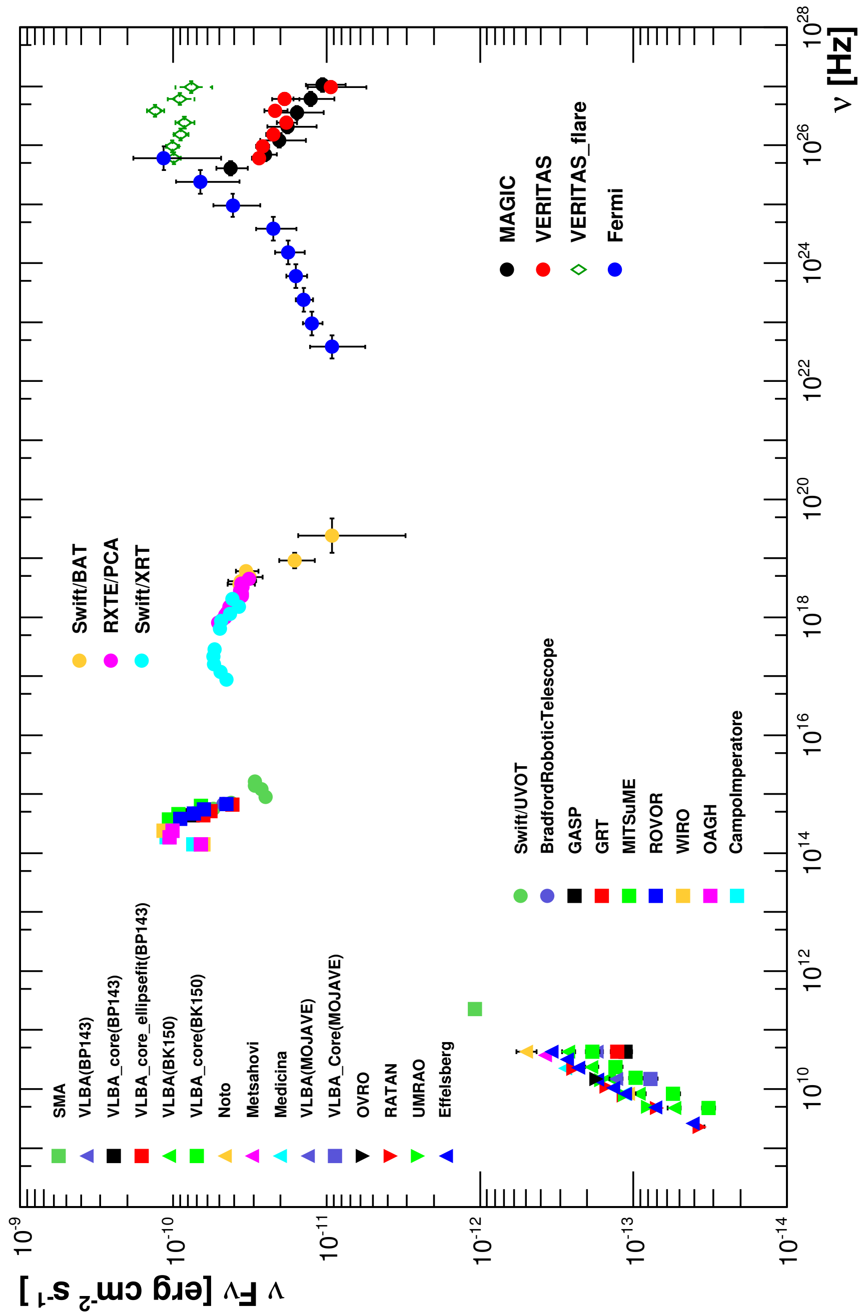

Figure B.2: Broad-band spectral energy distribution of Mrk 501, derived as the average of all data collected during the MWL campaign in 2009. Only the VERITAS data have been separated in a flaring episode and the remaining data. See [A$^+$11b] and section 6.4 for more details. Figure: [A$^+$11b].

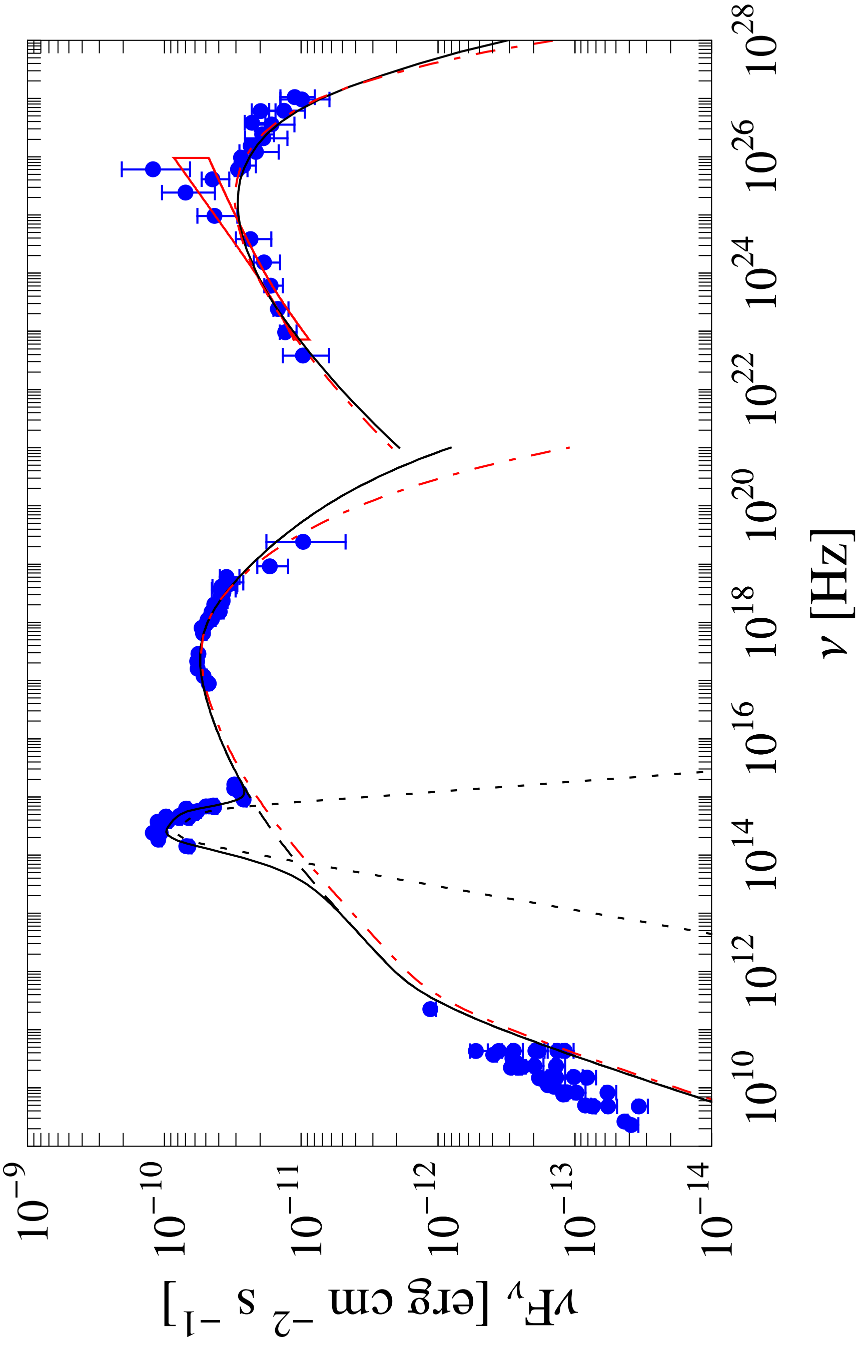

Figure B.3: SSC modeling of the Mrk 501 average state broad-bad SED collected during the MWL campaign in 2009 as presented in [A+11b]. The black solid line depicts the modeling of the average state which is considered in section 6.7, where also details about the corresponding parameters can be found. The red dash-dotted line depicts an alternative model which is not considered here. The contribution of the host galaxy (black dashed line) is included according to [S+98b]. Figure from [A+11b], where also more details can be found.

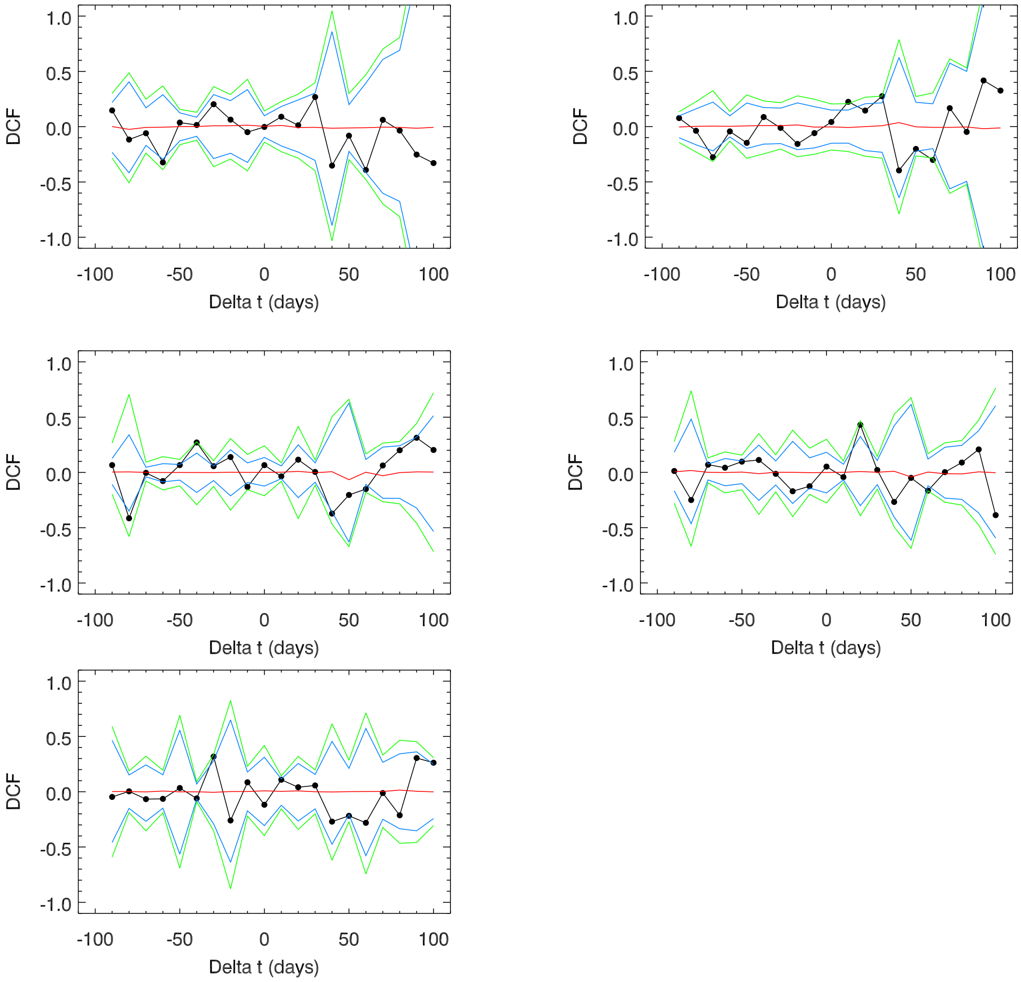

Figure B.4: Discrete Correlation Function (DCF) between the VHE gamma-ray and optical/UV/IR light curves for a range of possible time lags. Shown are DCFs for a combined VHE light curve vs. light curves measured by various instruments in different bands: UVOT W1(top left), GASP R (top right), Mitsume Ic (middle left), Mitsume g (middle right), OAGH Ks (bottom left). Confidence intervals (95% and 99%), which have been obtained based on simulations, are depicted by the blue and green lines, respectively. See subsection 6.5.3 for details.

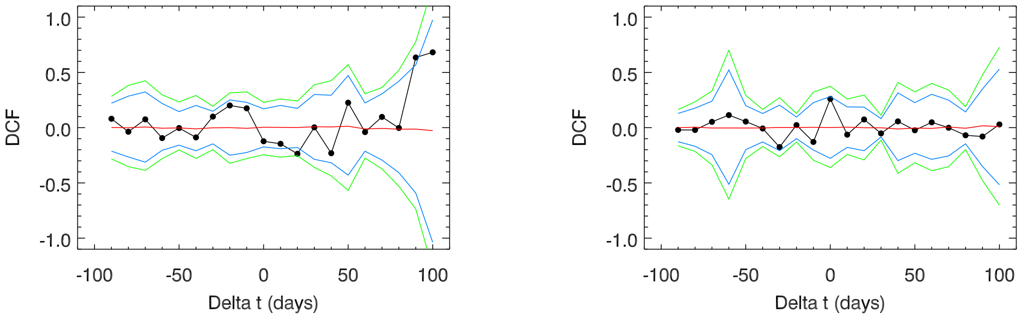

Figure B.5: Discrete Correlation Function of the VHE and radio light curves. Left: VHE vs. OVRO. Right: VHE vs. Metsahovi 37 GHz. For more details see the caption of Figure B.4 and subsection 6.5.3.

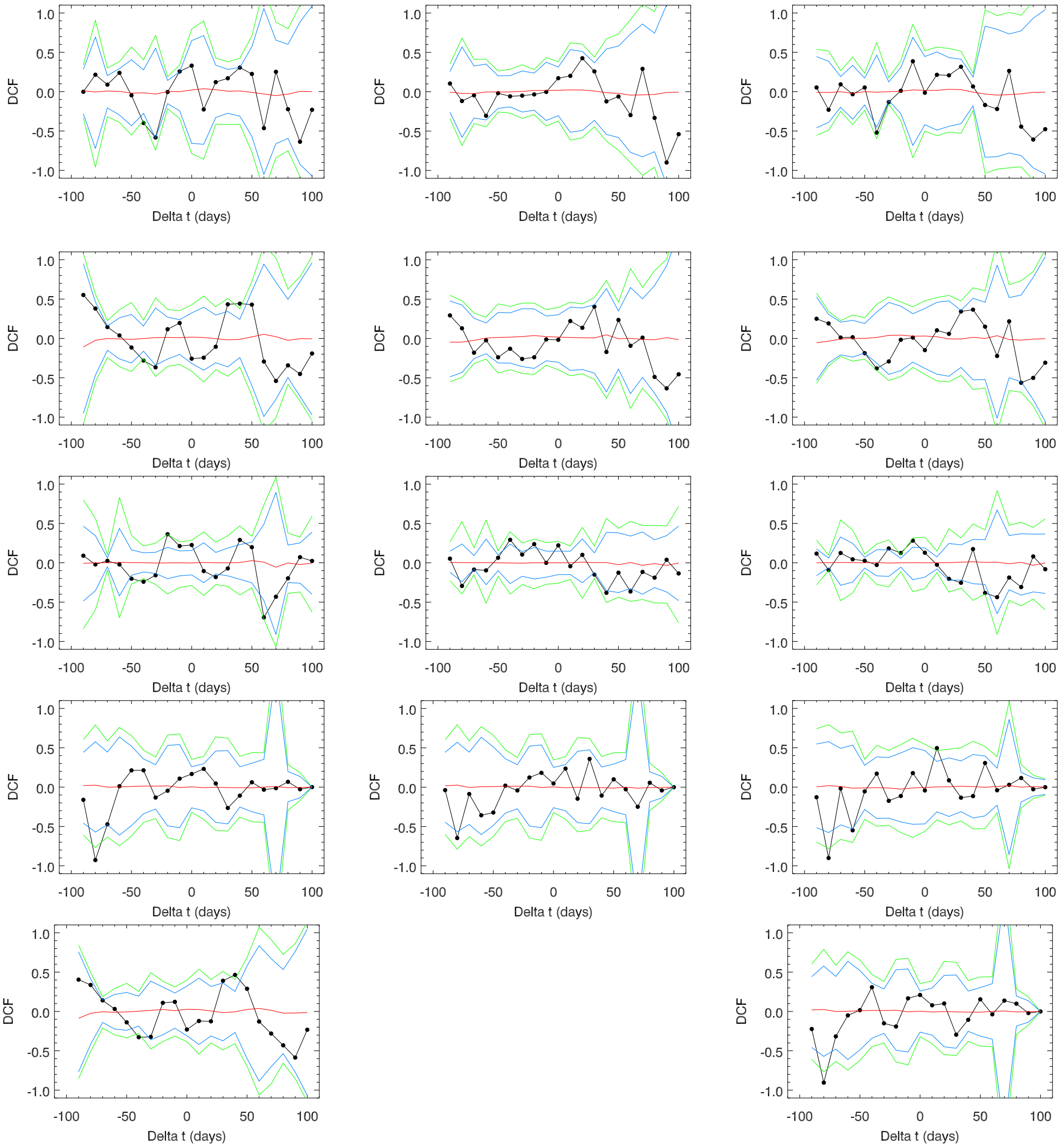

Figure B.6: Discrete Correlation Function between different combinations of X-ray and UV/optical/IR measurements. Optical instruments: UVOT W1 (top row), GASP R (second from top), Mitsume Ic (third from top), OAGH Ks (rorth row from top). X-ray instruments: Swift-XRT 0.3−2 keV (left column), Swift-XRT 2 - 10 keV (center column), *RXTE*-PCA (right). In the bottom row, the DCF between Swift-XRT 0.3−2 keV measurements after removal of the flare observation vs. GASP R (left) and OAGH Ks (right) are shown. For more details see the caption of Figure B.4 and subsection 6.5.3.

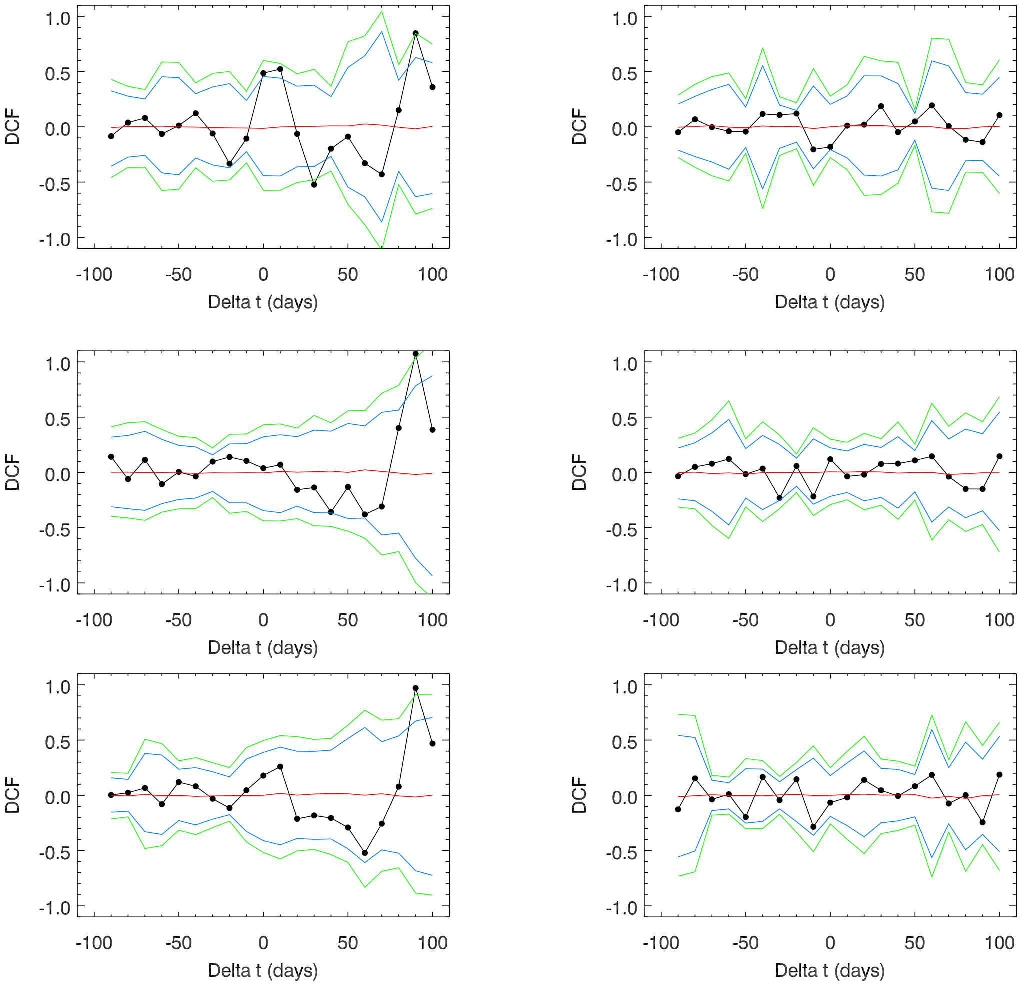

Figure B.7: Discrete Correlation Function between the X-ray and radio measurements. X-ray instruments (top to bottom): Swift-XRT 0.3−2 keV, Swift-XRT 2−10 keV, *RXTE*-PCA. Radio telescopes: OVRO (left), Metsahovi 37 GHz (right). For more details see the caption of Figure B.4 and subsection 6.5.3.

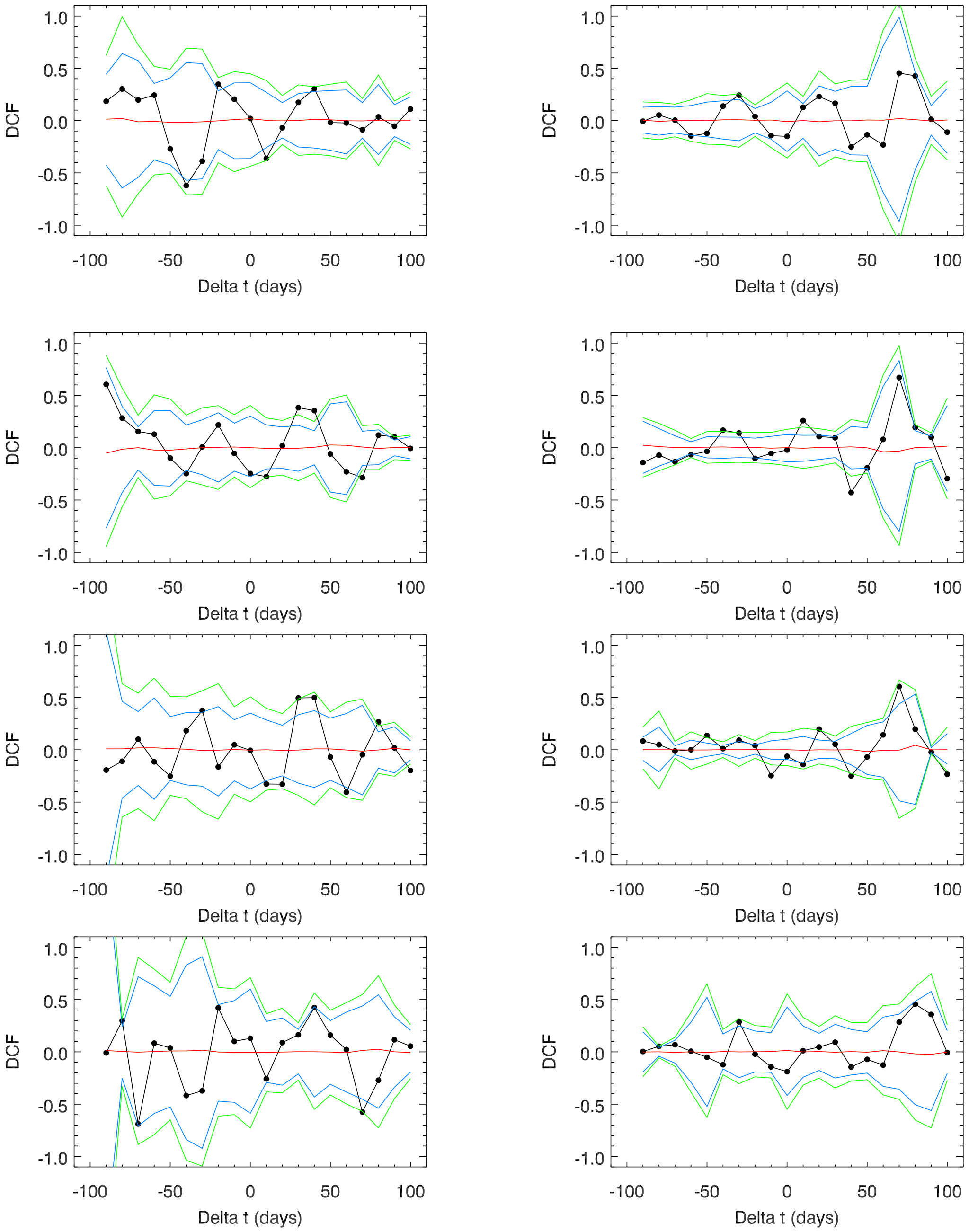

Figure B.8: Discrete Correlation Function between the UV/optical/NIR and radio measurements. Optical instruments from top to bottom: UVOT W1, GASP R, Mitsume Ic, OAGH Ks. Radio telescopes: OVRO (left), Metsahovi 37 GHz (right). For more details see the caption of Figure B.4 and subsection 6.5.3.

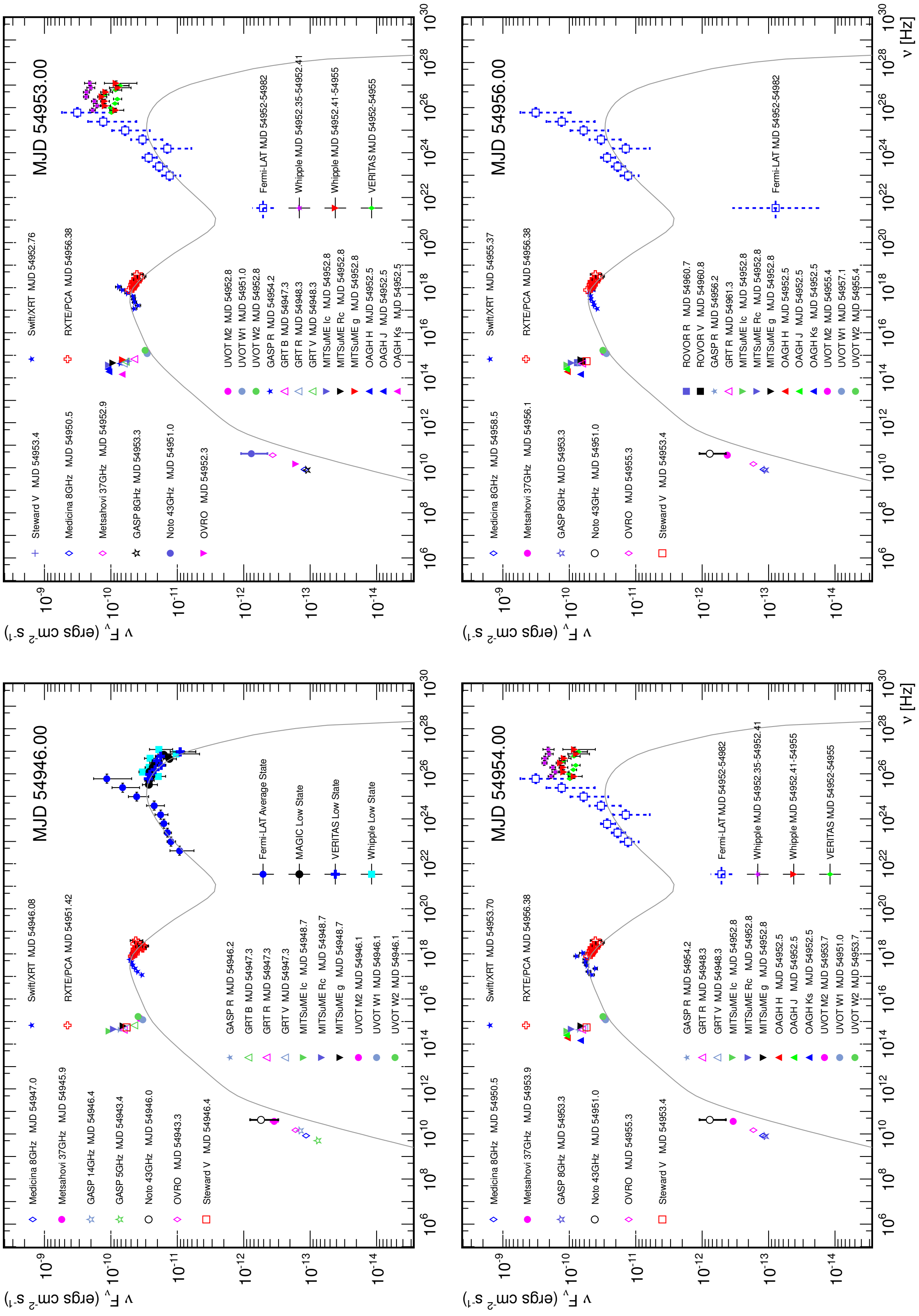

Figure B.9: Spectral energy distributions around the time of the first VHE flare (MJD 54952). The exact dates around which the data points have been collected are given in the figures. For more details on the data points see subsection 6.6.3.

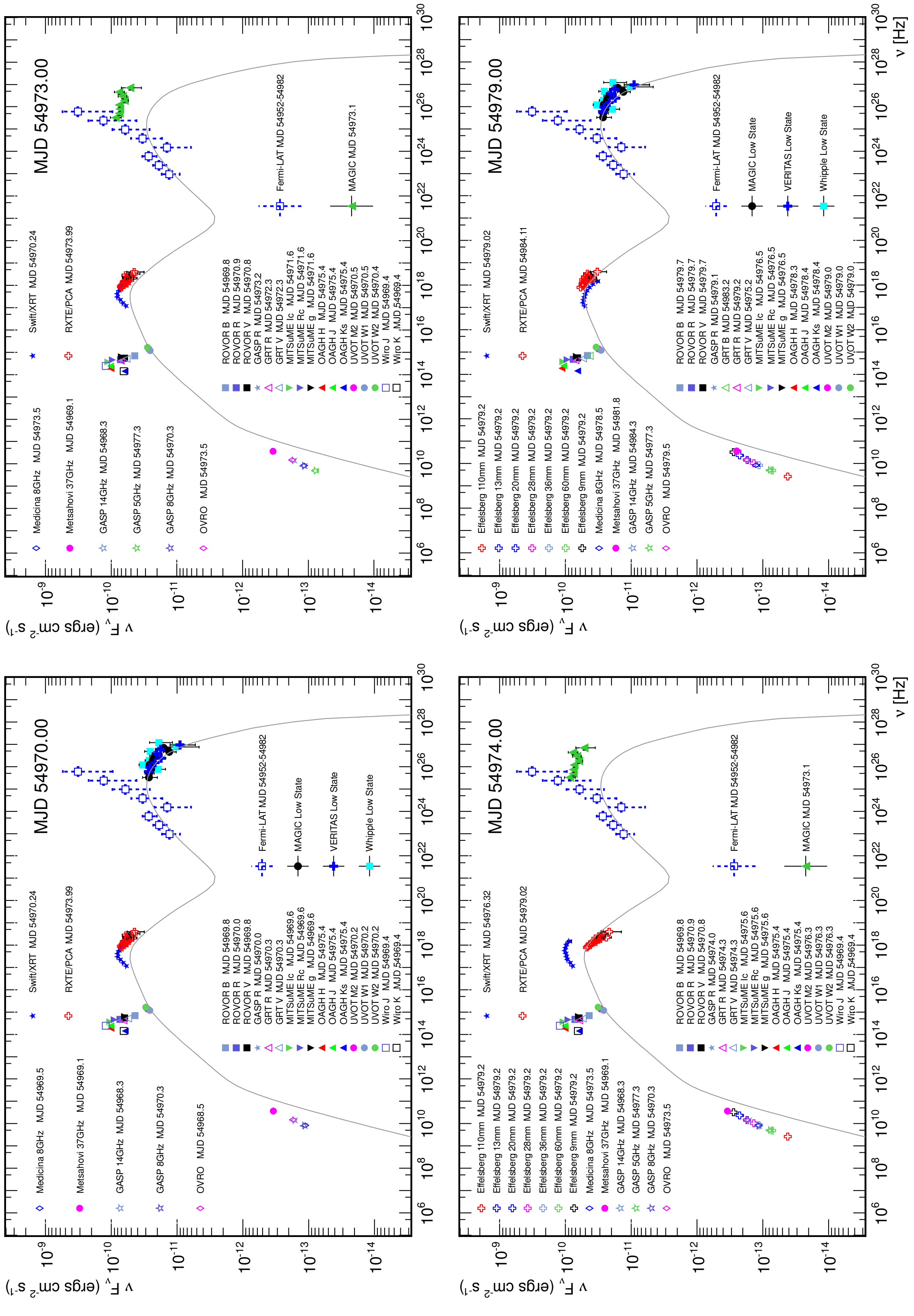

Figure B.10: Spectral energy distributions around the time of the second VHE flare (MJD 54973). The respective dates are given in the figures. For more details on the data points and the selection see subsection 6.6.3.

Table B.1: List of instruments which have been participating in the presented multi-frequency campaign and the corresponding energy ranges. Adapted from [A+11b].

Instrument/observatory	Energy range covered
MAGIC	0.12-5.8 TeV
VERITAS	0.20-5.0 TeV
Whipple	0.4-1.5 TeV
Fermi-LAT	0.1-400 GeV
Swift-BAT	14-195 keV
RXTE-PCA	3-28 keV
Swift-XRT	0.3-9.6 keV
Swift-UVOT	V, B, U, UVW1, UVM2, UVW2
Abastumani (through GASP-WEBT program)	R band
Lulin (through GASP-WEBT program)	R band
Roque de los Muchachos (KVA) (through GASP-WEBT program)	R band
St. Petersburg (through GASP-WEBT program)	R band
Talmassons (through GASP-WEBT program)	R band
Valle d'Aosta (through GASP-WEBT program)	R band
GRT	V, R, B bands
MitSume	g, Rc, Ic bands
ROVOR	B, R, V, I bands
Campo Imperatore (through GASP-WEBT program)	H, J, K bands
OAGH	H, J, K bands
WIRO	J, K bands
SMA	225 GHz
VLBA	4.8, 8.3, 15.4, 23.8, 43.2 GHz
Noto	8.4, 43 GHz
Metsähovi (through GASP-WEBT program)	37 GHz
VLBA (through MOJAVE program)	15 GHz
OVRO	15 GHz
Medicina	8.4, 22.3 GHz
UMRAO (through GASP-WEBT program)	4.8, 8.0, 14.5 GHz
RATAN-600	2.3, 4.8, 7.7, 11.1, 22.2 GHz
Effelsberg (through F-GAMMA program)	2.6, 4.6, 7.8, 10.3, 13.6, 21.7, 31 GHz

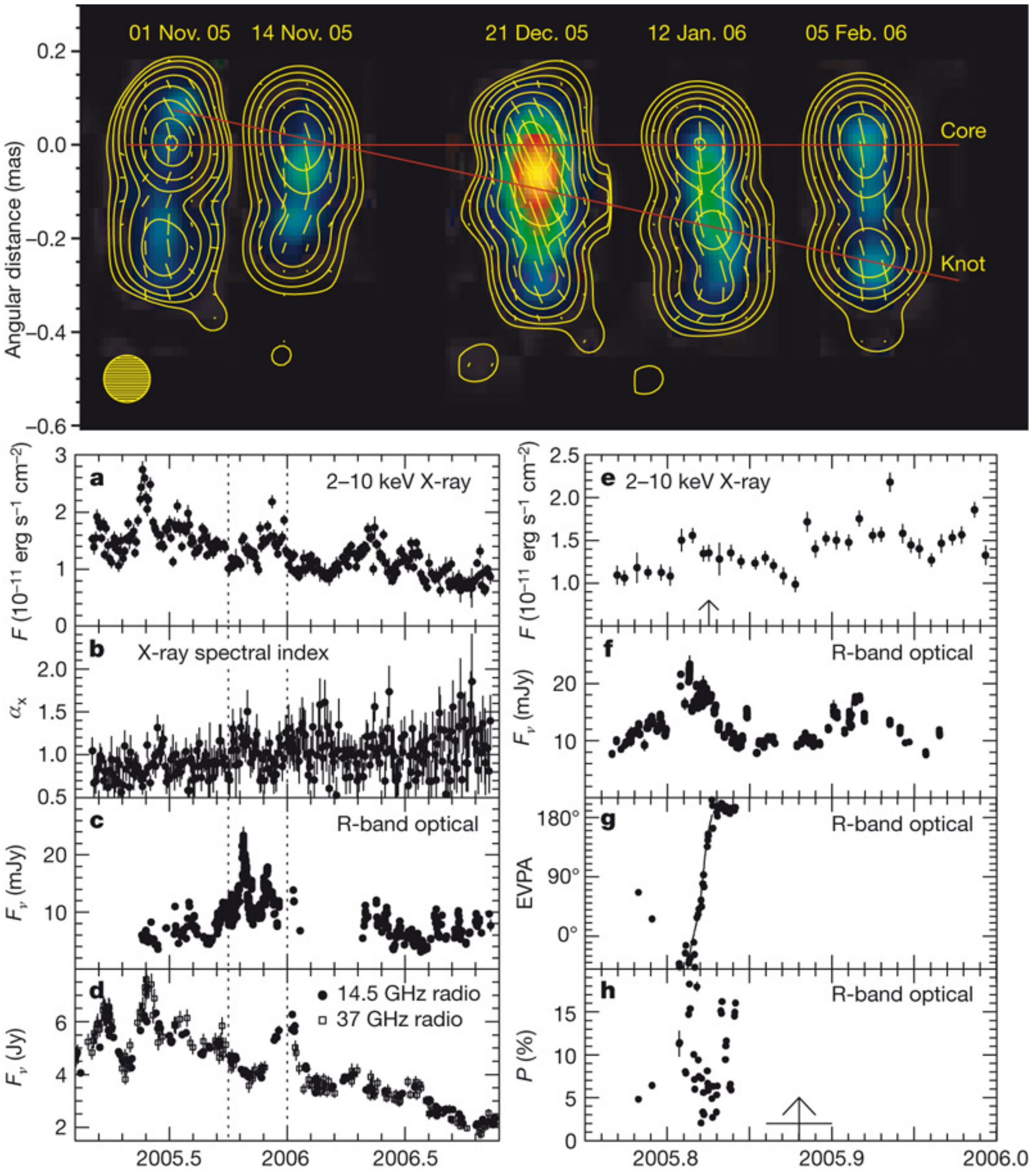

Figure B.11: Light curves and VLBA radio images obtained during an observational campaign on BL Lacertae in 2005/2006. Upper panel: sequence of VLBA images at 43 GHz. The axis on the left indicates the angular distance to the core. The total flux intensity is given by contours. The colors depict the intensity of polarized emission and the EVPA is indicated by the yellow lines. The movement of a feature with respect to the core is traced with the red lines. Lower left panel: light curves in X-rays (first from top), optical (third) and radio (fourth) are given for the time of the campaign. Additionally, the evolution of the power-law spectral index of the X-ray spectra is shown (second). Lower right panel: close-up views of the X-ray (first from top) and optical (second) light curves around the flare events are given. The two lower panels show the evolution of the polarization EVPA and the fraction of polarized optical emission. The arrow drawn in the X-ray light curve depicts a highly significant detection of gamma-rays (>200 GeV) and the arrow in the panel of polarization degree denotes the time when the feature is seen to pass the core in the VLBA images. Figures from [M$^+$08], where also more details can be found.

List of Figures

List of Tables

Bibliography

The references are listed in alphabetical order of the abbreviations and thus not necessarily in alphabetical order of the name of the first author. The last number in each reference refers back to the pages of citation within this thesis.

[A$^+$99a] Aharonian, F. A. et al. The temporal characteristics of the TeV gamma-radiation from MKN 501 in 1997. I. Data from the stereoscopic imaging atmospheric Cherenkov telescope system of HEGRA. *Astronomy and Astrophysics*, 342: 69–86, February 1999. 58

[A$^+$99b] Aharonian, F. A. et al. The time averaged TeV energy spectrum of MKN 501 of the extraordinary 1997 outburst as measured with the stereoscopic Cherenkov telescope system of HEGRA. *Astronomy and Astrophysics*, 349: 11–28, September 1999. 58

[A$^+$00] Andres, E. et al. The AMANDA neutrino telescope: principle of operation and first results. *Astroparticle Physics*, 13 (1): 1–20, March 2000. 6

[A$^+$04] Aharonian, F. et al. Very high energy gamma rays from the direction of Sagittarius A*. *Astronomy and Astrophysics*, 425 (1): L13–L17, October 2004. 10

[A$^+$06a] Achterberg, A. et al. First year performance of the IceCube neutrino telescope. *Astroparticle Physics*, 26 (3): 155–173, October 2006. 6

[A$^+$06b] Achterberg, A. et al. On the selection of AGN neutrino source candidates for a source stacking analysis with neutrino telescopes. *Astroparticle Physics*, 26 (4): 282–300, November 2006. 101

[A$^+$07a] Albert, J. et al. Discovery of Very High Energy Gamma-Ray Emission from the Low-Frequency-peaked BL Lacertae Object BL Lacertae. *The Astrophysical Journal*, 666 (1): L17–L20, September 2007. 54

[A$^+$07b] Albert, J. et al. Unfolding of differential energy spectra in the MAGIC experiment. *Nuclear Instruments and Methods in Physics Research A*, 583: 494–506, December 2007. 34, 66

[A$^+$07c] Albert, J. et al. Variable Very High Energy γ-Ray Emission from Markarian 501. *The Astrophysical Journal*, 669 (2): 862–883, November 2007. 53, 58, 89, 90

[A$^+$08a] Abraham, J. et al. Observation of the Suppression of the Flux of Cosmic Rays above 4×10^{19} eV. *Physical Review Letters*, 101 (6): 61101, August 2008. 5

[A$^+$08b] Albert, J. et al. Probing quantum gravity using photons from a flare of the active galactic nucleus Markarian 501 observed by the MAGIC telescope. *Physics Letters B*, 668 (4): 253–257, October 2008. 57

[A$^+$08c] Albert, J. et al. VHE γ-Ray Observation of the Crab Nebula and its Pulsar with the MAGIC Telescope. *Astrophysical Journal*, 674: 1037–1055, 2008. 15, 18, 19, 67, I

[A$^+$09a] Abbasi, R. et al. Search for point sources of high energy neutrinos with final data from AMANDA-II. *Physical Review D*, 79 (6): 62001, March 2009. 95

[A$^+$09b] Acciari, V. A. et al. Radio Imaging of the Very-High-Energy Gamma-Ray Emission Region in the Central Engine of a Radio Galaxy. *Science*, 325 (5): 444–, July 2009. 57

[A$^+$09c] Atwood, W. B. et al. The Large Area Telescope on the Fermi Gamma-Ray Space Telescope Mission. *The Astrophysical Journal*, 697 (2): 1071–1102, June 2009. 5, 59

[A$^+$10] Abdo, A. A. et al. A change in the optical polarization associated with a γ-ray flare in the blazar 3C 279. *Nature*, 463 (7283): 919–923, February 2010. 57

[A$^+$11a] Abbasi, R. et al. Time-integrated Searches for Point-like Sources of Neutrinos with the 40-string IceCube Detector. *The Astrophysical Journal*, 732 (1): 18, May 2011. 99, 100

[A$^+$11b] Abdo, A. A. et al. Insights into the High-energy Gamma-ray Emission of Markarian 501 from Extensive Multifrequency Observations in the Fermi Era. *The Astrophysical Journal*, 727 (2): 129, February 2011. 58, 60, 68, 76, 78, 82, 83, 84, 85, 86, 87, 98, 108, 109, 118, II

[A$^+$11c] Actis, M. et al. Design concepts for the Cherenkov Telescope Array CTA: an advanced facility for ground-based high-energy gamma-ray astronomy. *Experimental Astronomy*, pages 1–124, 2011. 15

[A$^+$11d] Ageron, M. et al. ANTARES: The first undersea neutrino telescope. *Nuclear Instruments and Methods in Physics Research A*, 656 (1): 11–38, November 2011. 6

[A$^+$12a] Aleksic, J. et al. Performance of the MAGIC stereo system obtained with Crab Nebula data. *Astroparticle Physics*, 35 (7): 435–448, February 2012. 6, 14, 15, 16, 19, 21, 40, 44, 47, I

[A$^+$12b] Aleksic, J. et al. PG 1553+113: Five Years of Observations with MAGIC. *The Astrophysical Journal*, 748 (1): 46, March 2012. 56

[A$^+$12c] Arlen, T. et al. Rapid TeV Gamma-Ray Flaring of BL Lacertae. *Accepted for publication in The Astrophysical Journal*, November 2012. arXiv:1211.3073. 53, 93

[A+13] Aleksic, J. et al. Unprecedented temporal evolution of the broad-band emission of the BL Lac Mrk 501. *in preparation*, 2013. 60

[AD03] Atoyan, A. M. and Dermer, C. D. Neutral Beams from Blazar Jets. *The Astrophysical Journal*, 586 (1): 79–96, March 2003. 56

[Aha00] Aharonian, F. A. TeV gamma rays from BL Lac objects due to synchrotron radiation of extremely high energy protons. *New Astronomy*, 5: 377–395, November 2000. 56

[ALS77] Axford, W. I., Leer, E. and Skadron, G. The acceleration of cosmic rays by shock waves. In *Proceedings of the 15th International Cosmic Ray Conference, Plovdiv, Bulgaria*, volume 11, pages 132–137. 1977. 7

[B+97a] Belolaptikov, I. A. et al. The Baikal underwater neutrino telescope: Design, performance, and first results. *Astroparticle Physics*, 7: 263–282, August 1997. 6

[B+97b] Bradbury, S. M. et al. Detection of gamma-rays above 1.5TeV from MKN 501. *Astronomy and Astrophysics*, 320: L5–L8, April 1997. 57

[B+05] Błażejowski, M. et al. A Multiwavelength View of the TeV Blazar Markarian 421: Correlated Variability, Flaring, and Spectral Evolution. *The Astrophysical Journal*, 630 (1): 130–141, September 2005. 56, 90

[B+07] Becker, J. K. et al. Astrophysical implications of high energy neutrino limits. *Astroparticle Physics*, 28 (1): 98–118, September 2007. 101

[B+09a] Biermann, P. L. et al. Active Galactic Nuclei: Sources for ultra high energy cosmic rays? In *Nuclear Physics B Proceedings Supplements*, volume 190, pages 61–78. May 2009. 12

[B+09b] Bretz, T. et al. The drive system of the major atmospheric gamma-ray imaging Cherenkov telescope. *Astroparticle Physics*, 31 (2): 92–101, March 2009. 16

[B+10] Becker, J. K. et al. Neutrino Emission from High-energy Component Gamma-ray Bursts. *The Astrophysical Journal*, 721 (2): 1891–1899, October 2010. 96, 97

[B+11] Biermann, P. L. et al. Photon and neutrino emission from active galactic nuclei. In *Nuclear Physics B Proceedings Supplements*, pages 284–286. August 2011. 56

[BB09] Becker, J. K. and Biermann, P. L. Neutrinos from active black holes, sources of ultra high energy cosmic rays. *Astroparticle Physics*, 31 (2): 138–148, March 2009. 97

[BD66] Bahcall, J. N. and Davis, R. J. On the Problem of Detecting Solar Neutrinos. *Stellar Evolution*, page 241, 1966. 6

[Bec08] Becker, J. K. High-energy neutrinos in the context of multimessenger astrophysics. *Physics Reports*, 458 (4): 173–246, March 2008. 96

[Bel78a] Bell, A. R. The acceleration of cosmic rays in shock fronts. I. *Monthly Notices of the Royal Astronomical Society*, 182: 147–156, January 1978. 7

[Bel78b] Bell, A. R. The acceleration of cosmic rays in shock fronts. II. *Monthly Notices of the Royal Astronomical Society*, 182: 443–455, February 1978. 7

[Ber89] Bertero, M. Linear inverse and ill posed problems. *Advances in Electronics and Electron Physics*, 75: 1–120, 1989. 28, 47, 66

[BG06] Bergström, L. and Goobar, A. *Cosmology and Particle Astrophysics.* Springer, July 2006. 3, 4, 5, 11, 14

[BH34] Bethe, H. and Heitler, W. On the Stopping of Fast Particles and on the Creation of Positive Electrons. In *Proceedings of the Royal Society of London. Series A*, pages 83–112. August 1934. 9

[BHK12] Boettcher, M., Harris, D. E. and Krawczynski, H. *Relativistic Jets from Active Galactic Nuclei.* Wiley-VCH, January 2012. 6, 7, 8, 9, 53

[BL98] Blobel, V. and Lohrmann, E. Statistische und numerische Methoden der Datenanalyse. Teubner, 1998. 24, 26, 27, 28, 29

[Bla01] Blanch, O. How to use the camera simulation program. Technical report, 2001. MAGIC-TDAS 01-04. 17

[Blo84] Blobel, V. Unfolding methods in high energy physics experiments. *DESY 84-118*, 1984. 24, 26, 27, 28, 29

[Blo96] Blobel, V. The RUN manual: regularized unfolding for high-energy physics experiments. *OPAL Technical Note TN361*, May 1996. 28

[BO78] Blandford, R. D. and Ostriker, J. P. Particle acceleration by astrophysical shocks. *Astrophysical Journal*, 221: L29–L32, April 1978. 7

[Boo01] de Boor, C. A Practical Guide to Splines. Springer, 2001. 30

[Böt02] Böttcher, M. Physics input from multiwavelength observations of AGN. *Bulletin of the Astronomical Society of India*, 30: 115–124, March 2002. 56

[BR78] Blandford, R. D. and Rees, M. J. Some comments on radiation mechanisms in Lacertids. *In: Pittsburgh Conference on BL Lac Objects*, pages 328–341, 1978. 53

[Bre01] Breiman, L. Random Forests. *Machine Learning*, 45 (1): 5–32, 2001. 19, 34

[BRM09] Böttcher, M., Reimer, A. and Marscher, A. P. Implications of the very High Energy Gamma-Ray Detection of the Quasar 3C279. *The Astrophysical Journal*, 703 (1): 1168–1175, September 2009. 56

[BS12] Biermann, P. L. and de Souza, V. Centaurus A: The Extragalactic Source of Cosmic Rays with Energies above the Knee. *The Astrophysical Journal*, 746 (1): 72, February 2012. 5

[BT+09] Borla Tridon, D. et al. Performance of the Camera of the MAGIC II Telescope. *eprint*, June 2009. arXiv:0906.5448. 16

[C+97] Catanese, M. et al. Multiwavelength Observations of a Flare from Markarian 501. *The Astrophysical Journal*, 487 (2): L143–L146, October 1997. 58, 59

[C+98] Cleveland, B. T. et al. Measurement of the Solar Electron Neutrino Flux with the Homestake Chlorine Detector. *Astrophysical Journal*, 496: 505, March 1998. 6

[CLR67] Chakravarti, I. M., Laha, R. G. and Roy, J. Handbook of Methods of Applied Statistics. John Wiley & Sons, 1967. 33

[Cur08] Curtef, V. *A New Unfolding Method for the MAGIC Telescope*. Ph.D. thesis, Technische Universität Dortmund, 2008. 42

[D+01] Donato, D. et al. Hard X-ray properties of blazars. *Astronomy and Astrophysics*, 375: 739–751, September 2001. 54

[D+12] Doert, M. et al. Correlated neutrino and gamma-ray emission from Active Galactic Nuclei - an estimation. *Journal of Physics: Conference Series*, 355 (1): 012039, March 2012. 96, 97, 100, II

[DA+99] Djannati-Ataï, A. et al. Very High Energy Gamma-ray spectral properties of MKN 501 from CAT Čerenkov telescope observations in 1997. *Astronomy and Astrophysics*, 350: 17–24, October 1999. 58

[Der86] Dermer, C. D. Binary collision rates of relativistic thermal plasmas. II - Spectra. *Astrophysical Journal*, 307: 47–59, August 1986. 97

[Der11] Dermer, C. D. Are Gamma-Ray Bursts the Sources of the Ultra-High Energy Cosmic Rays? In *Gamma Ray Bursts 2010. AIP Conference Proceedings*, pages 355–360. August 2011. 12

[DH12] Doert, M. and Heck, D. The TRAJECT Option of the Air-Shower Simulation Program CORSIKA. *KIT Scientific Working Papers*, 1, March 2012. 17

[Doe09] Doert, M. Automated Production of Standardized and Tailor-made Monte Carlo Simulations for the MAGIC Telescopes. *Diploma Thesis*, July 2009. 17

[DR10] Dermer, C. D. and Razzaque, S. Acceleration of Ultra-high-energy Cosmic Rays in the Colliding Shells of Blazars and Gamma-ray Bursts: Constraints from the Fermi Gamma-ray Space Telescope. *The Astrophysical Journal*, 724 (2): 1366–1372, December 2010. 5

[Dre10] Dreyer, J. *Neutrinos from Starburst-Galaxies*. Ph.D. thesis, Technische Universität Dortmund, June 2010. 4, I

[Dru12] Drury, L. ScienceDirect.com - Astroparticle Physics - Origin of cosmic rays. *Astroparticle Physics*, 2012. 10

[DS93] Dermer, C. D. and Schlickeiser, R. Model for the High-Energy Emission from Blazars. *Astrophysical Journal*, 416: 458, October 1993. 56

[DS+05] Domingo Santamaria, E. et al. The DISP analysis method for point-like or extended gamma source searches/studies with the MAGIC Telescope. In *Proceedings of the 29th International Cosmic Ray Conference, Pune, India*, volume 5, page 363. 2005. 19, 20

[Ein10] Einecke, S. *Parameter optimization for unfolding of MAGIC energy spectrums*. Master's thesis, Technische Universität Dortmund, August 2010. 42

[EK88] Edelson, R. A. and Krolik, J. H. The discrete correlation function - A new method for analyzing unevenly sampled variability data. *Astrophysical Journal*, 333: 646–659, October 1988. 74, 77, II

[ESR12] Eichmann, B., Schlickeiser, R. and Rhode, W. Differences of Leptonic and Hadronic Radiation Production in Flaring Blazars. *The Astrophysical Journal*, 749 (2): 155, April 2012. 101

[F+98a] Fossati, G. et al. A unifying view of the spectral energy distributions of blazars. *Monthly Notices of the Royal Astronomical Society*, 299 (2): 433–448, September 1998. 53, 54, 57, 93, I

[F+98b] Fukuda, Y. et al. Measurement of a small atmospheric ν_μ/ν_e ratio. *Physics Letters B*, 433 (1): 9–18, August 1998. 6

[Feg97] Fegan, D. J. Topical Review: γ/hadron separation at TeV energies. *Journal of Physics G: Nuclear and Particle Physics*, 23 (9): 1013–1060, September 1997. 19

[Fer54] Fermi, E. Galactic Magnetic Fields and the Origin of Cosmic Radiation. *Astrophysical Journal*, 119: 1, January 1954. 7

[Fin13] Finke, J. D. Compton Dominance and the Blazar Sequence. *The Astrophysical Journal*, 763 (2): 134, February 2013. 57

[Fo94] Fomin, V. P. and others. New methods of atmospheric Cherenkov imaging for gamma-ray astronomy. I. The false source method. *Astroparticle Physics*, 2: 137–150, May 1994. 16

[FR12] Falkenburg, B. and Rhode, W. *From Ultra Rays to Astroparticles*. A Historical Introduction to Astroparticle Physics. Springer, December 2012. 3, 5, 6, 7, 10, 11, 14

[Fre03] Fredholm, E. I. Sur une classe d'équations fonctionnelles. *Acta Mathematica*, 27: 365–390, 1903. 24

[FRV08] Franceschini, A., Rodighiero, G. and Vaccari, M. Extragalactic optical-infrared background radiation, its time evolution and the cosmic photon-photon opacity. *Astronomy and Astrophysics*, 487 (3): 837–852, September 2008. 5, 78, 79, 97, 98

[G+98] Ghisellini, G. et al. A theoretical unifying scheme for gamma-ray bright blazars. *Monthly Notices of the Royal Astronomical Society*, 301 (2): 451–468, December 1998. 55

[G+06] Gliozzi, M. et al. Long-Term X-Ray and TeV Variability of Mrk 501. *The Astrophysical Journal*, 646 (1): 61–75, July 2006. 89

[G+08] Goebel, F. et al. Upgrade of the MAGIC Telescope with a Multiplexed Fiber-Optic 2GSamples/s FADC Data Acquisition System system. In *Proceedings of the 30th International Cosmic Ray Conference, Merida, Yucatan, Mexico*, volume 3, pages 1481–1484. 2008. 16

[G+12] Giommi, P. et al. Simultaneous Planck, Swift, and Fermi observations of X-ray and γ-ray selected blazars. *Astronomy and Astrophysics*, 541: 160, May 2012. 56

[Gai91] Gaisser, T. K. *Cosmic Rays and Particle Physics*. Cambridge University Press, January 1991. 97

[GJ53] Galbraith, W. and Jelley, J. V. Light Pulses from the Night Sky associated with Cosmic Rays. *Nature*, 171 (4): 349–350, February 1953. 14

[GP69] Gribov, V. and Pontecorvo, B. Neutrino astronomy and lepton charge. *Physics Letters B*, 28 (7): 493–496, January 1969. 6

[Gre66] Greisen, K. End to the Cosmic-Ray Spectrum? *Physical Review Letters*, 16 (1): 748–750, April 1966. 5

[GTC05] Ghisellini, G., Tavecchio, F. and Chiaberge, M. Structured jets in TeV BL Lac objects and radiogalaxies. Implications for the observed properties. *Astronomy and Astrophysics*, 432 (2): 401–410, March 2005. 58

[H+03] Hofmann, W. et al. Status of the H.E.S.S. Project. In *Proceedings of the 28th International Cosmic Ray Conference, Trukuba, Japan*, page 2811. July 2003. 14

[H+06] Holder, J. et al. The first VERITAS telescope. *Astroparticle Physics*, 25 (6): 391–401, July 2006. 14

[H+12] Horns, D. et al. Hardening of TeV gamma spectrum of active galactic nuclei in galaxy clusters by conversions of photons into axionlike particles. *Physical Review D*, 86 (7): 75024, October 2012. 57

[Hei54] Heitler, W. *Quantum theory of radiation*. International Series of Monographs on Physics. Clarendon Press, 1954. 8

[Hes12] Hess, V. Observation of Penetrating Radiation of seven Balloon Flights. *Physikalische Zeitschrift*, 13: 1084, 1912. 3

[Hil84] Hillas, A. M. The Origin of Ultra-High-Energy Cosmic Rays. *IN: Annual review of astronomy and astrophysics. Palo Alto*, 22: 425–444, 1984. 11, 12, I

[Hil85] Hillas, A. M. Cerenkov light images of EAS produced by primary gamma. In *Proceedings of the 19th International Cosmic Ray Conference, La Jolla, USA*, pages 445–448. 1985. 18, 19

[HK10] Halzen, F. and Klein, S. R. IceCube: An Instrument for Neutrino Astronomy. *Nuovo Cimento*, 81: 081101, 2010. 95

[HKC$^+$98] Heck, D. et al. CORSIKA: a Monte Carlo code to simulate extensive air showers. *Wissenschaftliche Berichte FZKA*, 6019, February 1998. 17

[Ho07] Honda, M. and others. Calculation of atmospheric neutrino flux using the interaction model calibrated with atmospheric muon data. *Nuovo Cimento*, D75: 043006, 2007. 99, 100

[HS06] Henri, G. and Saugé, L. The Bulk Lorentz Factor Crisis of TeV Blazars: Evidence for an Inhomogeneous Pileup Energy Distribution? *The Astrophysical Journal*, 640 (1): 185–195, March 2006. 58

[HZ97] Halzen, F. and Zas, E. Neutrino Fluxes from Active Galaxies: A Model-independent Estimate. *Astrophysical Journal*, 488: 669, October 1997. 96

[J$^+$05] Jorstad, S. G. et al. Polarimetric Observations of 15 Active Galactic Nuclei at High Frequencies: Jet Kinematics from Bimonthly Monitoring with the Very Long Baseline Array. *The Astronomical Journal*, 130 (4): 1418–1465, October 2005. 52

[JR76] Jauch, J. and Rohrlich, F. *The theory of photons and electrons: the relativistic quantum field theory of charged particles with spin one-half.* Texts and monographs in physics. Springer, 1976. 8

[K$^+$89] Kanbach, G. et al. The project EGRET (energetic gamma-ray experiment telescope) on NASA's Gamma-Ray Observatory GRO. *Space Science Reviews*, 49 (1): 69–84, January 1989. 5

[K$^+$00a] Kirk, J. G. et al. Particle Acceleration at Ultrarelativistic Shocks: An Eigenfunction Method. *The Astrophysical Journal*, 542 (1): 235–242, October 2000. 7

[K$^+$00b] Krawczynski, H. et al. X-ray/TeV-gamma-ray observations of several strong flares of Mkn 501 during 1997 and implications. *Astronomy and Astrophysics*, 353: 97–107, January 2000. 58

[K$^+$04] Krawczynski, H. et al. Multiwavelength Observations of Strong Flares from the TeV Blazar 1ES 1959+650. *The Astrophysical Journal*, 601 (1): 151–164, January 2004. 56, 90

[KD10] Kneiske, T. M. and Dole, H. A lower-limit flux for the extragalactic background light. *Astronomy and Astrophysics*, 515: 19, June 2010. 5

[Kro99] Krolik, J. H. *Active galactic nuclei : from the central black hole to the galactic environment*. Princeton, 1999. 52

[Kry77] Krymskii, G. F. A regular mechanism for accelerating charged particles at the shock front. *Akademiia Nauk SSSR*, 234: 1306–1308, June 1977. 7

[KS12] Katz, U. F. and Spiering, C. High-energy neutrino astrophysics: Status and perspectives. *Progress in Particle and Nuclear Physics*, 67 (3): 651–704, July 2012. 55, I

[KT12] Kusunose, M. and Takahara, F. A Leptonic Model of Steady High-energy Gamma-Ray Emission from Sgr A*. *The Astrophysical Journal*, 748 (1): 34, March 2012. 10

[L$^+$01] Lessard, R. W. et al. A new analysis method for reconstructing the arrival direction of TeV gamma rays using a single imaging atmospheric Cherenkov telescope. *Astroparticle Physics*, 15 (1): 1–18, March 2001. 19, 20

[L$^+$11] Lister, M. L. et al. Gamma-Ray and Parsec-scale Jet Properties of a Complete Sample of Blazars From the MOJAVE Program. *The Astrophysical Journal*, 742 (1): 27, November 2011. 93

[Lin63] Linsley, J. Evidence for a Primary Cosmic-Ray Particle with Energy 1020 eV. *Physical Review Letters*, 10 (4): 146–148, February 1963. 5

[LM83] Li, T. P. and Ma, Y. Q. Analysis methods for results in gamma-ray astronomy. *Astrophysical Journal*, 272: 317–324, September 1983. 21

[LT12] Lacki, B. C. and Thompson, T. A. Cosmic rays and high energy emission from starburst galaxies. *The Spectral Energy Distribution of Galaxies*, 284: 393–396, August 2012. 11

[M$^+$03] Mücke, A. et al. BL Lac objects in the synchrotron proton blazar model. *Astroparticle Physics*, 18 (6): 593–613, March 2003. 56

[M$^+$08] Marscher, A. P. et al. The inner jet of an active galactic nucleus as revealed by a radio-to-γ-ray outburst. *Nature*, 452 (7190): 966–969, April 2008. 53, 57, 91, 92, 119, II

[M$^+$10a] Marscher, A. P. et al. Probing the inner jet of the quasar PKS 1510–089 with multi-waveband monitoring during strong gamma-ray activity. *The Astrophysical Journal*, 710 (2): L126–L131, February 2010. 57, 91, 92

[M$^+$10b] Moralejo, R. A. et al. MARS: The MAGIC Analysis and Reconstruction Software. *Astrophysics Source Code Library*, page 11004, November 2010. 17, 34

[M$^+$12a] Mankuzhiyil, N. et al. Emitting Electrons and Source Activity in Markarian 501. *The Astrophysical Journal*, 753 (2): 154, July 2012. 58

[M$^+$12b] Meyer, E. T. et al. Breaking the Blazar Sequence: A New View of Radio Loud AGN Unification. In *Fermi & Jansky Proceedings*. May 2012. arXiv:1205.0794. 57

[M$^+$13] Milke, N. et al. Solving inverse problems with the unfolding program TRUEE: Examples in astroparticle physics. *Nuclear Instruments and Methods in Physics Research A*, 697: 133–147, January 2013. 22, 24, 29, 30, 31, 32, 33, 35, 43, 46, 47, 48, 49, I

[Man93] Mannheim, K. The proton blazar. *Astronomy and Astrophysics*, 269: 67–76, March 1993. 56

[Man11] Mankuzhiyil, N. BL Lac Objects: Laboratory to study the environment and properties of emitting particles in relativistic jets. In *Proceedings of the 32nd International Cosmic Ray Conference, Beijing, China*, volume 11, page 157. 2011. 56

[Mar82] Marchuk, G. I. *Methods of numerical mathematics*. Springer, 1982. 28

[Maz07] Mazin, D. *A Study of Very High Energy Gamma-ray Emission from AGNs and Constraints on the Extragalactic Background Light*. Ph.D. thesis, Technische Universität München, 2007. 19, 20, I

[MB92] Mannheim, K. and Biermann, P. L. Gamma-ray flaring of 3C 279 - A proton-initiated cascade in the jet? *Astronomy and Astrophysics*, 253: L21–L24, January 1992. 56

[MC28] Millikan, R. A. and Cameron, G. H. The Origin of the Cosmic Ray. *Scientific American*, 139: 136–137, August 1928. 4

[MGC92] Maraschi, L., Ghisellini, G. and Celotti, A. A jet model for the gamma-ray emitting blazar 3C 279. *Astrophysical Journal*, 397: L5–L9, September 1992. 56

[Mor02] Moralejo, A. The reflector simulation program v.0.6. Technical report, 2002. MAGIC-TDAS 02-11. 17

[MRB83] Moore, R. L., Readhead, A. C. S. and Baath, L. Superluminal acceleration in 3C345. *Nature*, 306: 44–46, November 1983. 52

[N$^+$01] Neshpor, Y. I. et al. BL Lac: A New Ultrahigh-Energy Gamma-Ray Source. *Astronomy Reports*, 45 (4): 249–254, April 2001. 54

[NST12] Neronov, A., Semikoz, D. and Taylor, A. M. Very hard gamma-ray emission from a flare of Mrk 501. *Astronomy and Astrophysics*, 541: 31, May 2012. 56, 90

[Ohm12] Ohm, S. Gamma-rays from starburst galaxies. In *5th International Meeting on High Energy Gamma-Ray Astronomy. AIP Conference Proceedings*, pages 64–71. December 2012. 11

[P^+92] Punch, M. et al. Detection of TeV photons from the active galaxy Markarian 421. *Nature*, 358: 477, August 1992. 57

[P^+98] Pian, E. et al. BeppoSAX Observations of Unprecedented Synchrotron Activity in the BL Lacertae Object Markarian 501. *Astrophysical Journal Letters*, 492: L17, January 1998. 58, 89, 90, 91

[P^+08] Paoletti, R. et al. The global trigger system of the magic telescope array. In *2008 IEEE Nuclear Science Symposium and Medical Imaging conference (2008 NSS/MIC)*, pages 2781–2783. IEEE, 2008. 16

[P^+09] Piner, B. G. et al. Significant Limb-Brightening in the Inner Parsec of Markarian 501. *The Astrophysical Journal Letters*, 690 (1): L31–L34, January 2009. 58

[PG95] Padovani, P. and Giommi, P. The connection between x-ray- and radio-selected BL Lacertae objects. *Astrophysical Journal*, 444: 567–581, May 1995. 54, 57

[Pic11] Pichel, A. Detailed Multifrequency Study of a Rapid VHE Flare of Mrk501 in May 2009. In *Proceedings of the 32nd International Cosmic Ray Conference, Beijing, China*, volume 8, page 171. 2011. 56, 72, 76, 78, 79, 90

[PPE08] Piner, B. G., Pant, N. and Edwards, P. G. The Parsec-Scale Jets of the TeV Blazars H1426+428, 1ES 1959+650, and PKS 2155-304: 2001-2004. *The Astrophysical Journal*, 678 (1): 64–77, May 2008. 58

[PPE10] Piner, B. G., Pant, N. and Edwards, P. G. The Jets of TeV Blazars at Higher Resolution: 43 GHz and Polarimetric VLBA Observations from 2005 to 2009. *The Astrophysical Journal*, 723 (2): 1150–1167, November 2010. 54, 68

[PW65] Penzias, A. A. and Wilson, R. W. A Measurement of Excess Antenna Temperature at 4080 Mc/s. *Astrophysical Journal*, 142: 419–421, July 1965. 5

[Q^+96] Quinn, J. et al. Detection of Gamma Rays with $E > 300$ GeV from Markarian 501. *The Astrophysical Journal*, 456 (2), January 1996. 57

[Ree84] Rees, M. J. Black Hole Models for Active Galactic Nuclei. *Annual review of astronomy and astrophysics*, 1984. 52

[RL08] Rybicki, G. B. and Lightman, A. P. *Radiative Processes in Astrophysics*. Wiley-VCH, September 2008. 6

[S^+98a] Samuelson, F. W. et al. The TeV Spectrum of Markarian 501. *The Astrophysical Journal*, 501 (1): L17–L20, July 1998. 58

[S^+98b] Silva, L. et al. Modeling the Effects of Dust on Galactic Spectral Energy Distributions from the Ultraviolet to the Millimeter Band. *The Astrophysical Journal*, 509 (1): 103–117, December 1998. 85, 109

[S+02] Schweizer, T. et al. The optical calibration of the MAGIC telescope camera. *IEEE Transactions on Nuclear Science*, 49: 2497–2503, October 2002. 16

[SBR94] Sikora, M., Begelman, M. C. and Rees, M. J. Comptonization of diffuse ambient radiation by a relativistic jet: The source of gamma rays from blazars? *Astrophysical Journal*, 421: 153–162, January 1994. 56

[Sch63] Schmidt, M. 3C 273 : A Star-Like Object with Large Red-Shift. *Nature*, 197 (4): 1040, March 1963. 52

[Sch94] Schmelling, M. The Method of reduced cross entropy: A General approach to unfold probability distributions. *Nuclear Instruments and Methods in Physics Research A*, 340: 400–412, 1994. 28

[Sch13] Schmidt, F. CORSIKA Shower Images. `http://www.ast.leeds.ac.uk/~fs/showerimages.html`, January 2013. 14, I

[SDJS92] Stecker, F. W., De Jager, O. C. and Salamon, M. H. TeV gamma rays from 3C 279 - A possible probe of origin and intergalactic infrared radiation fields. *Astrophysical Journal*, 390: L49–L52, May 1992. 5

[Ste71] Stecker, F. W. Cosmic gamma rays. *Baltimore: Mono Book Corporation*, 249, 1971. 97

[Ste04] Stecker, F. W. Tests of quantum gravity and large extra dimensions models using high energy γ-ray observations. *New Astronomy Reviews*, 48 (5): 437–444, April 2004. 57

[Str09] Strahler, E. A. *Searches for neutrinos from gamma ray bursts with the AMANDA-II and IceCube detectors*. Ph.D. thesis, University of Wisconsin-Madison, November 2009. 12, I

[T+01] Tavecchio, F. et al. Theoretical Implications from the Spectral Evolution of Markarian 501 Observed with BeppoSAX. *The Astrophysical Journal*, 554 (2): 725–733, June 2001. 58

[Tak11] Takami, H. γ-rays as a diagnostic of the origin of core radiation in low-luminosity active galactic nuclei. *Monthly Notices of the Royal Astronomical Society*, 413: 1845–1851, May 2011. 84

[Tes10] Tescaro, D. *TeV Gamma-ray observation of nearby Active Galactic Nuclei with the MAGIC telescope: exploring the high energy region of the multiwavelength picture*. Ph.D. thesis, Universitat Autònoma de Barcelona, 2010. 60, 63, 107

[TH11] Takami, H. and Horiuchi, S. The production of ultra high energy cosmic rays during the early epochs of radio-loud AGN. *Astroparticle Physics*, 34 (1): 749–754, May 2011. 5

[Tik63] Tikhonov, A. N. On the solution of ill-posed problems and the method of regularization. *Doklady Akademii Nauk SSSR*, 151: 501–504, 1963. 28

[TK95] Timmer, J. and König, M. On generating power law noise. *Astronomy and Astrophysics*, 300: 707, 1995. 75

[TMG98] Tavecchio, F., Maraschi, L. and Ghisellini, G. Constraints on the Physical Parameters of TeV Blazars. *The Astrophysical Journal*, 509 (2): 608–619, December 1998. 56, 90

[UMP02] Uttley, P., McHardy, I. M. and Papadakis, I. E. Measuring the broad-band power spectra of active galactic nuclei with RXTE. *Monthly Notices of the Royal Astronomical Society*, 332 (1): 231–250, May 2002. 75

[UMU97] Ulrich, M.-H., Maraschi, L. and Urry, C. M. Variability of Active Galactic Nuclei. *Annual Review of Astronomy and Astrophysics*, 35: 445–502, 1997. 53

[UP95] Urry, C. M. and Padovani, P. Unified Schemes for Radio-Loud Active Galactic Nuclei. *Publications of the Astronomical Society of the Pacific*, 107: 803, September 1995. 51, 52, 53, I

[V$^+$03] Vaughan, S. et al. On characterizing the variability properties of X-ray light curves from active galaxies. *Monthly Notices of the Royal Astronomical Society*, 345 (4): 1271–1284, November 2003. 74, 75

[Vig98] Vignaud, D. The GALLEX solar neutrino experiment. In *Nuclear Physics B Proceedings Supplements*, pages 20–29. DAPNIA/SPP, CEA/Saclay, 91191 Gif-sur-Yvette, France, January 1998. 6

[Wag04] Wagner, W. *Design and Realisation of a New AMANDA Data Acquisition System with Transient Waveform Recorders*. Ph.D. thesis, Universität Dortmund, October 2004. 4, I

[Wag09] Wagner, R. The MAGIC Telecopes. `http://wwwmagic.mpp.mpg.de`, April 2009. 15, I

[Wee03] Weekes, T. C. *Very High Energy Gamma Ray Astronomy*. Taylor & Francis, 2003. 14

[WH13] Wakely, S. and Horan, D. TeVCat. `http://tevcat.uchicago.edu`, February 2013. 56

[Wo89] Weekes, T. and others. Observation of TeV gamma rays from the Crab nebula using the atmospheric Cerenkov imaging technique. *Astrophysical Journal*, 342: 379–395, 1989. 14, 57

[WT77] Weekes, T. C. and Turver, K. E. Gamma-ray astronomy from 10-100 GeV: A new approach. *In ESA Recent Advan. in Gamma-Ray Astronomy p 279-286 (SEE N78-11899 02-88)*, 124: 279–286, July 1977. 14

[ZK66] Zatsepin, G. T. and Kuzmin, V. A. Upper Limit of the Spectrum of Cosmic Rays. *Journal of Experimental and Theoretical Physics Letters*, 4: 78, August 1966. 5

Author’s Publications

Publications which are associated with this thesis and which are signed by the author of this thesis as (one of) the main author(s):

[1] Aleksic, J. et al. Unprecedented temporal evolution of the broad-band emission of the BL Lac Mrk 501. *in preparation.*

[2] Milke, N., Doert, M. et al. Solving inverse problems with the unfolding program TRUEE: Examples in astroparticle physics. *Nuclear Instruments and Methods in Physics Research A*, 697: 133–147, January 2013.

[3] Doert, M. et al. Correlated neutrino and gamma-ray emission from Active Galactic Nuclei - an estimation. *Journal of Physics: Conference Series*, 355 (1): 012039, March 2012.

[4] Doert, M. and Heck, D. The TRAJECT Option of the Air-Shower Simulation Program CORSIKA. *KIT Scientific Working Papers*, 1, March 2012.

[5] Wagner, R. et al. Monitoring of bright, nearby Active Galactic Nuclei with the MAGIC telescopes. In *Proceedings of the 32nd International Cosmic Ray Conference, Beijing, China*, volume 8, page 143. 2011.

List of Abbreviations

ADC	Analog to Digital Converter
AGN	Active Galactic Nucleus
AMANDA	Antarctic Muon And Neutrino Detector Array
ASM	All-Sky Monitor
BAT	Burst Alert Telescope
BH	Black Hole
CMB	Cosmic Microwave Background
CORSIKA	COsmic Ray SImulations for KAscade
CR	Cosmic Ray
CTA	Cherenkov Telescope Array
DACF	Discrete Auto-Correlation Function
DAQ	Data AQuisition
DC	Direct Current
DCF	Discrete Correlation Function
DM	Dark Matter
DRS	Domino Ring Sampling chip
EBL	Extragalactic Background Light
EC	External Compton
EeV	Exaelectronvolt ($= 10^{18}$ eV)
EGRET	Energetic Gamma Ray Experiment Telescope
eV	Electronvolt
EVPA	Electric Vector Position Angle
FADC	Flash Analog to Digital Converter
FSRQ	Flat Spectrum Radio Quasar
GASP	GLAST-AGILE Support Program
GeV	Gigaelectronvolt ($= 10^{9}$ eV)
GRB	Gamma-Ray Burst
GST	Gamma-ray Space Telescope
GZK	Greisen-Zatsepin-Kuzmin
HBL	High-frequency peaked BL Lac object
HEGRA	High Energy Gamma Ray Astronomy
H.E.S.S.	High Energy Stereoscopic System
HST	Hubble Space Telescope
IACT	Imaging Atmospheric Cherenkov Telescope
IC	Inverse Compton
IC-40	IceCube 40 String configuration
LAT	Large Area Telescope

LBL	Low-frequency peaked BL Lac object
MAGIC	Major Atmospheric Gamma Imaging Cherenkov telescopes
MC	Monte Carlo
MeV	Megaelectronvolt ($= 10^6$ eV)
MJD	Modified Julian Date
MWL	Multi-Wavelength
NSB	Night-sky background
OVRO	Owens Valley Radio Observatory
PCA	Proportional Counter Array
phe	photo electron
PMT	Photomultiplier Tube
PSD	Power Spectral Density
PSF	Point Spread Funktion
PWN	Pulsar Wind Nebula
RF	Random Forest
RMS	Root Mean Square
RUN	Regularized Unfolding
RXTE	Rossi X-ray Timing Explorer
SED	Spectral Energy Distribution
Sgr	Saggitarius
SuperKamiokande	Super Kamioka nucleon decay experiment
SM	Standard Model of particle physics
SMBH	SuperMassive Black Hole
SNR	Supernova Remnant
SSC	Synchrotron Self Compton
TeV	Teraelectronvolt ($= 10^{12}$ eV)
TRUEE	Time-Dependent Regularized Unfolding for Economics and Engineering problems
UHE	Ultra High Energy
UVOT	Ultraviolet/Optical Telescope
VCSEL	Vertical Cavity Laser Diodes
VERITAS	Very Energetic Radiation Imaging Telescope
VHE	Very High Energy
VLBA	Very Long Baseline Array
VLBI	Very Long Baseline Interferrometry
WEBT	Whole Earth Blazar Telescope
XRT	X-Ray Telescope
ZeV	Zetaelectronvolt ($= 10^{21}$ eV)

I would like to thank...

... first of all my supervisor Prof. Dr. Dr. Wolfgang Rhode for his continuous support in the course of this doctoral thesis. I am very grateful for the opportunities he provided to participate in numerous conferences, meetings and schools and for his specialist advice and steady encouragement.

... Prof. Dr. Claus Gössling for his willingness and his efforts involved in being the second assessor of this thesis.

... David Paneque for giving me the opportunity to work with such an extensive data set as the one from Mrk 501, for never tiring to discuss a newly found feature in the data and for always being ready to provide help and advice.

... Daniel Mazin and Stefan Klepser for hosting me during my visits to the Barcelona group, and for the support and sometimes looong discussions which were exchanged in matters of MAGIC analysis and unfolding.

... Francis Halzen, who kindly supported me during my stay in Madison and helped me to find the way into the multi-messenger picture. I also have to thank Aongus Ó Murchadha and Julia Tjus for a fruitful collaboration, for providing advice and being open for discussions.

... Markus Böttcher, Felix Spanier and Stephan Richter for spontaneous meetings on short notice, instructive discussions and a lot of patience.

... Julian Krause for oftentimes immediate answers to technical questions and for being a good “fellow sufferer” in the phase of applying, writing and finishing up; Nina Nowak for very productive co-working and for teaching me a lot of things about variability studies on light curves; and Elina Lindfors for always being ready to answer my questions on blazar physics, for fruitful discussions - and for making me play football as “the only other girl” among the MAGIC guys.

... the entire MAGIC collaboration, who I had the opportunity to be a part of during the work on this doctoral thesis. In that time, I was lucky to meet so many knowledgeable, inspiring and lovable people, who created the perfect environment to learn and develop, scientifically and personally. I would like to thank all of you for your support and appreciation, for teaching me new things and for just being the “MAGIC family”.

... the ASTROPARTICLE PHYSICS WORKING GROUP at TU Dortmund, in the current and also in the former cast, while special thanks are dedicated to MICHAEL BACKES for supplying a lot of background, critical questions and encouragement, to MALWINA UELLENBECK, for sharing a birthday, a sense of humor and many good thoughts over the years, and to NATALIE MILKE, for being a great collaborator and being patient enough to always discuss the unfolding algorithms yet another time.

... the Dortmund Monte Carlo team: MALWINA UELLENBECK, NIKOLA STRAH, ADAM HADAMEK and KATHARINA FRANTZEN, for their help in feeding the MAGIC collaboration with the Monte Carlo simulations they were constantly craving for.

... the many people who were kind enough to offer their help in proofreading, namely SABRINA EINECKE, ANN-KRISTIN OVERKEMPING, KATHARINA FRANTZEN, FABIAN CLEVERMANN, MICHAEL BACKES, BURKHARD STEINKE, ADAM JOHN NETTO and STEPHAN LUCKA.

... the GERMAN RESEARCH FOUNDATION (DFG) for funding this research in the scope of the Collaborative Research Center SFB 823.

Außerdem möchte ich mich bei meinem ehemaligen Physiklehrer HEINZ-GÜNTER POHL bedanken. Rückblickend war er mit Sicherheit derjenige, der mich durch seine eigene Faszination für Physik und Astronomie schon zu Schulzeiten auf den Weg gebracht hat, dem ich nun selbst seit Jahren mit Begeisterung folge. Vielen Dank dafür!

Als letzten Punkt auf dieser Liste, aber keineswegs zuletzt möchte ich meiner Familie und meinen guten Freunden danken, die mir immer Rückhalt gegeben und mich geerdet haben, mich ziemlich oft entbehrt, zu Flughäfen gebracht und abgeholt haben, die stressige Phasen mit mir durchgestanden und mir immer wieder Mut und Kraft gegeben haben.

Besonders danke ich MEINEN ELTERN für Unterstützung, die immer da war, wenn ich sie brauchte, und STEPHAN LUCKA, der mich durch seine oftmals weisen Ratschläge und unermüdliche "Betreuung" sicher das ein oder andere mal vor dem Verrücktwerden gerettet hat.

Ich danke euch allen von Herzen!